The Dissertation Committee for Patryk Pawel Radyjowski
certifies that this is the approved version of the following dissertation:

Additively Manufactured Si-SiC Combustion Devices: The Role of Heat Recirculation in Counter-flowing Reactors

Committee:

Janet Ellzey, Supervisor

David Bourell

Desiderio Kovar

Erica Belmont

Additively Manufactured Si-SiC Combustion Devices: The Role of Heat Recirculation in Counter-flowing Reactors

by

Patryk Pawel Radyjowski

Dissertation

Presented to the Faculty of the Graduate School of

The University of Texas at Austin

in Partial Fulfillment

of the Requirements

for the Degree of

Doctor of Philosophy

The University of Texas at Austin

May 2021

Moim rodzicom.

To my parents.

Acknowledgments

The Ph.D. degree program was a life-changing journey that I would not have accomplished without many people's support. I could never fully express the extent of my gratitude to all who were part of this experience.

First and foremost, I would like to thank my dissertation supervisor, Dr. Janet Ellzey, for her guidance, support, and patience through the years. I was extremely fortunate to find such an exceptional mentor who taught me how to be a researcher. I highly appreciate the freedom to explore entrusted in me combined with the skillful oversight that kept me on track. My thanks also go to my dissertation committee members: Dr. David Bourell, Dr. Desiderio Kovar, and Dr. Erica Belmont. Dr. Bourell introduced me to the world of additive manufacturing and cermet processing. His support and patience were invaluable, especially in the early years as I went through the Material Science crash course. Dr. Kovar's door was always open whenever I had issues with ceramic and broad material-related problems. Moreover, he played a crucial role in transitioning from research to writing and successfully finishing the Ph.D. degree. Without that, I would still be in the laboratory following yet another exciting development.

I owe a special thanks to Dr. Erica Belmont, whom I had first met when she was a Ph.D. student of Dr. Ellzey herself. Dr. Belmont introduced me to the research on counter-flow combustion reactors and the world of academia. Her encouragement was a significant factor in my choice to pursue the degree at The University of Texas at Austin later on. I would like to express my gratitude to Dr. Ingmar Schoegl, another previous student of Dr. Ellzey. His support was critical at multiple stages of my degree.

I would also like to thank Dr. Joseph Beaman for his support, involving me in his research group's work, and granting access to necessary AM equipment. My

acknowledgments would not be complete without a special thanks to Mark Phillips. Thank you for all the time spent helping me fix the equipment while providing an endless supply of anecdotes and technical know-how. My gratitude also goes to the ME Department for Teaching Assistant possibilities thorough the years. Special thanks go to Dr. Matthew Hall, who accepted me as a TA for his thermodynamics class for multiple years. Helping undergraduate students understand the basics of thermodynamics brought a whole new, unique meaning to my degree program.

My gratitude also goes to Dr. Guillermo Rein and Dr. Markus Mueller. They introduced me to the world of research during my undergraduate studies at The University of Edinburgh. Dr. Rein was my academic advisor/mentor during those formative years. Meanwhile, Dr. Mueller entrusted me with the first research project during my Master's degree. Without their influence, my Ph.D. journey would have never started.

My deep appreciation goes to my best friends Crystal Chaloupka, Manuela Grabosh, and Deborah Navarro. I am greatly indebted to them for all their support and for making sure I remember about the life outside work. You are part of my best memories over the years and helped me develop as a person. Thank you.

Finally, my most heartfelt thanks go to my parents Ewa and Witold Radyjowski, as well as my brother Maciej Radyjowski. Thank you for your endless love, help, and support. All I am today is because of you, and I would have never made it that far without you.

Mamo, Tato, dziekuje.

Patryk Pawel Radyjowski

The University of Texas at Austin

May 2021

Abstract

Additively Manufactured Si-SiC Combustion Devices: The Role of Heat Recirculation in Counter-flowing Reactors

Patryk Pawel Radyjowski, Ph.D.
The University of Texas at Austin, 2021

Supervisor: Janet Ellzey

The importance of energy efficiency demands novel approaches to combustion of fossil fuels. Significant research has focused on increasing efficiency, reducing emissions, and improving fuel flexibility. One approach of recycling energy from the flame to the reactants, called excess enthalpy combustion, offers all of these potential advantages. A variety of heat recirculating reactor designs exist, but they are all characterized by small pores or channels to maximize the exposure of hot walls to the flowing reactants. This requires a material that can withstand the combustion environment without constraining possible geometries. Standard materials such as ceramics and superalloys are limited in either one or the other of these criteria. A potential solution is an additively manufactured ceramic-metal composite, siliconized silicon carbide (Si-SiC) cermet. It can be fabricated in the desired shape and withstands temperatures up to 1400°C. This work examines the fabrication of Si-SiC parts by a multi-step process including laser sintering, transient binder processing, and metal infiltration. Modifications in the process improved intermediate handling and part quality. Future material science development of manufacturing method could lead to a 1900°C capable material. The newly developed material was investigated under a lean methane-air combustion environment. Flame compatibility and good thermal oxidation above 1200°C

were confirmed in the isolated exposure tests. Using the AM process above, three counter-flow combustors were manufactured with different channel geometries such that the surface area to volume ratio was varied. The relationship between the resulting change in heat transfer and the stable operating range was investigated. Higher heat recirculation increased internal temperatures and improved flame stability. The role of heat recirculation was crucial under high speed, high firing rate conditions. Experimental findings were supported by analytical modeling and previous research in the field. CO and NO_x emissions registered at exits were low, substantially below equilibrium. The material degradation of Si-SiC was tracked over an entire 80-hour period. The operation near 1400°C resulted in partial melting and protrusions of infiltrating metal. Otherwise, passive oxidation was observed to happen in-line with the literature. The new material system for high-temperature applications shows significant potential for the development of new combustor designs.

Table of Contents

List of Tables

List of Figures

Chapter 1: Introduction

Various forms of combustion remain the primary means of energy conversion for a range of thermodynamic processes. A better understanding of combustion and new ways of improving efficiency and flexibility has the potential to significantly impact the world's overall energy consumption. The simplest combustion phenomenon is a laminar premixed flame which forms the basis for many more complicated combustion processes. A laminar flame exhibits three main characteristics which help outline the fundamentals of combustion: the laminar flame speed which describes the rate at which reactants are consumed , flammability limits which specify the minimum and maximum fuel/air ratios necessary for self-sustained combustion, and flame quenching which describes the balance between heat release and heat loss. The theoretical basis of the laminar flame speed were identified by Mallard and Le Chatelier [1] who showed that the flame is sustained by heat transfer from the flame to the incoming reactants. This model linked the burning rate with the thermal properties of the gas. Therefore it is possible to influence the laminar flame speed or burning rate by introducing additional heat transfer paths. Enhanced heat transfer results in higher reactant temperature which also leads to potentially broader flammability limits [2] opening possibilities for new technologies such as thermal oxidizers and fuel reformers. Furthermore, external heat transfer has a significant role in the flame quenching mechanism, where heat losses overpower heat release leading to the extinguishment of the flame [3].

One method of enhancing the heat transfer from the flame to the reactants is through the insertion of solid surface into the flame zone. The introduction of solid surfaces provides new conductive and radiative heat transfer paths from hot products to cooler reactants. The incorporation of solids to recycle heat upstream of the

combustion front led to purposely designed recirculating heat reactors [4, 5]. In this dissertation, the effects of heat transfer on flame stabilization are examined through experiments on various reactors which were fabricated using additive manufacturing. Both the combustion and manufacturing aspects of this study are discussed.

The remainder of this chapter is an in-depth introduction to heat recirculating reactors (HRR) with special attention to parallel channel counter-flow designs. The objectives of this study are put forward in section 1.4. Chapter 2 presents a general overview of high-temperature materials, section 2.1, coupled with a detailed discussion of the new material system utilized in this study, section 2.3. The combustion experiments executed to evaluate the influence of heat transfer on HRR performance are described in chapter 3. The methods section 3.1 is followed by experimental results sections 3.3 through 3.5 and the results discussion in section 3.6. An analytical model of counter-flow HRR by Schoegl [6], discussed in section 3.2.1, has been employed for improved analysis of experimental data. Finally, the degradation of the new material in the combustion environment is assessed in section 3.7. Conclusions and further recommendations are presented in chapter 4.

1.1 Excess Enthalpy Combustion

The classic setup for analyzing stable premixed flame in an adiabatic tube, as discussed by Mallard and Le Chatelier, is shown on the Figure 1.1a. The reactants are flowing from the left while thermal diffusion preheats the mixture until a sufficient temperature is reached for self-sustaining chemical reactions. Once the thermal energy overcomes the activation barrier, reactions occur at a short timescale, quickly heating the flow. There is no subsequent energy loss, and products leave at adiabatic flame temperature. Since the reaction front propagation speed is equal to the inlet flow velocity, the flame is stationary. By introducing a solid medium, Figure 1.1b, a

more effective heat propagation path is established such that thermal energy can flow from hot products upstream to incoming reactants. This idea of heat recycling led to the development of HRR described by Weinberg [4]. Following this initial concept,

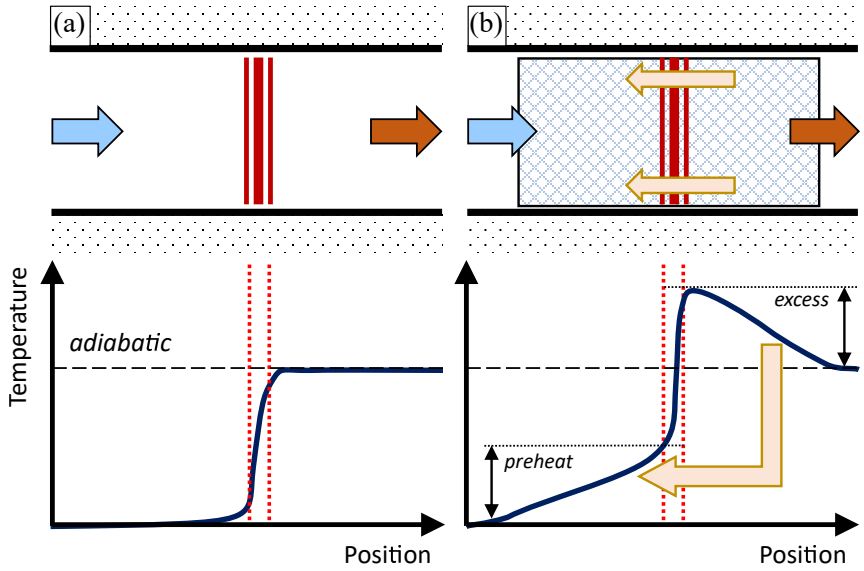

Figure 1.1: Premixed combustion in an adiabatic tube with the temperature profiles: a) classic stable flame b) solid heat recirculation example

Jones et al. [7] presented a range of configurations that resulted in heat reciruclation in a combustion device. The example used in the above is a unidirectional arrangement. It depends solely on the additional conductivity of a solid wall to achieve heat recirculation over a long distance. Reviews of these HRR types have been published for a variety of applications [8–10]. This work concentrates on the counter-flow configuration, introduced in detail in the Section 1.2. The exit temperature of HRR remains at adiabatic temperature due to the overall system energy balance as there are no additional energy inputs. Nonetheless, the local temperature at the flame front is higher than the level predicted by equilibrium analysis [2]. Therefore HRRs are often called *superadiabatic* or *excess enthalpy* combustion devices. The higher temperature significantly increases the burning rate, hence the faster flame velocity. This

effect is achieved without chemical catalysts commonly used in other burner types. The non-catalytic operation avoids the catalyst overheating and poisoning issues [11], which allows for greater fuel flexibility as well as more economical operation. Despite improved reaction rates the excessive heat losses can overwhelm reactions heat release leading to flame extinction at low flow velocities. In contrast, the high velocity flows usually carry sufficient energy to overcome losses, but the reactor's residence time is reduced. A finite length reactor has an upper-velocity limit at which the kinetics timescale is too long compared to residence time [12]. The exact velocity limits are device-specific, although the range usually correlates with deeply laminar to transitional flows. The flow geometry has an impact in terms of gas-solid convective heat exchange. Narrow passages improve the convection, which enables the heat recirculation operation. However, the wall quenching restricts the minimum passage size when the convective energy loss at flame position exceeds the energy generation [13]. Although the hot wall quenching diameter is substantially smaller than traditional values, it can pose an issue for micro-scale combustion.

Heat recirculating reactors have a wide equivalence ratio range expanding past regular flammability limits. Conventional flames are constrained on the fuel/air mixture ratios based on the limit when heat losses exceed the heat generation, subsequently cooling the flame and stopping thermally activated reactions. Heat recirculating reactors keep superadiabatic temperatures in the proximity of the reaction front. Therefore reaction rates remain sufficiently to continue burning even at ultra-lean or ultra-rich conditions. The ability to expand the flammability limits enables new applications and enhances the flexibility of HRR combustors. The equilibrium prediction of methane/air combustion products at atmospheric pressure obtained from Cantera [14] is shown on Figure 1.2. Although the equilibrium analysis does not perfectly represent a kinetics-driven process, the obtained data provides an insight into general

trends. The application range of superadiabatic reactors is visualized in Figure 1.3. The operation within the stability range produces the maximum heat output and the usual combustion products: water H_2O and carbon dioxide CO_2. The stability of operation is improved near the flammability limits, as discussed above. The reactor's geometric flexibility in the micro and mesoscale range provides an attractive portable solution as a thermal energy source that remains highly efficient despite its small size. The ultra-lean combustion is beneficial due to implied complete combustion, increasing fuel efficiency as well as low emissions of carbon monoxide CO and nitric oxide NO_x species [15]. Furthermore, the ultra-lean device can be used as a thermal oxidizer, where minimal amounts of fuel and other pollutants are broken down into less harmful combustion products. In the ultra-rich regime, a fuel reformer converts the mixture to hydrogen H_2 and CO, both fuels for different processes. The ability to store H_2 within dense hydrocarbon fuel and reform as-needed is an interesting alternative for pressurized hydrogen storage. [16].

The lean and ultra-lean combustors have been examined as the heat source for a range of mechanical [17] and electrical [18] energy conversion. Operation at superadiabatic temperatures and the presence of highly emissive solid walls makes the HRR a suitable source for thermal radiation [19, 20]. The radiative output can be used in direct heating applications such as industrial drying or evaporation. The experimental study on swirl-type geometry by Kim et al. [21] found that the radiant heat transfer driven by high surface temperatures is the primary loss mechanism. Radiant heat loss used as a heating source showed significantly higher thermal efficiency when compared with electrical power generation. The advancements in low bandgap semiconductor materials brought new interest in thermophotovoltaic solutions [22]. The heat recirculating reactors have been studied as the main radiant source for a thermophotovoltaic generation due to their high intensity, consistent output [23, 24].

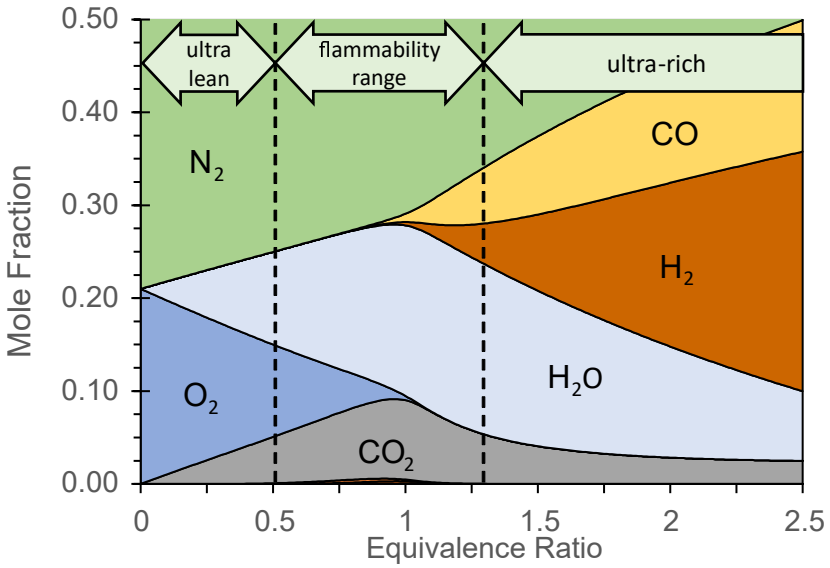

Figure 1.2: Equilibrium products prediction for methane/air combustion at atmospheric pressure.

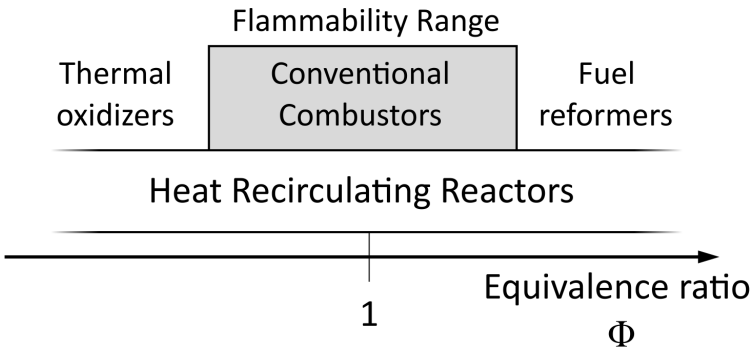

Figure 1.3: Applications of heat recirculating reactors

Chen and Ronney [25], presented the unique use of a microscale ultra-lean HRR as a thermal oxidizer for a face mask to destroy air pollutants.

Heat recirculating reactors under ultra-rich operation produce substantial amounts of H_2 and CO. The review by Ellzey et al. [26] found that nearly 50% of hydrogen H atoms hydrocarbon fuel can be reformed into hydrogen gas H_2 under ultra-rich fuel reforming. The efficiency of carbon C to CO conversion is even higher and reaches 75%. Notably, the hydrogen generation is supplemented by the high-temperature water shift reaction downstream of the flame. The experimental work by Hamare et al. [27] showed that superadiabatic temperatures and slow velocities are beneficial for this secondary reaction. The resulting syngas, a mixture of H_2 and CO, is used as a feedstock for a range of chemical reactions or burned directly for additional energy release [28]. Ahn et al. [29] showed a direct implementation of fuel reforming by running the exhaust of ultra-rich fuel reformer into a solid oxide fuel cell. The utility of reformed gases can be further improved by low-energy separation processes to obtain pure hydrogen gas. Subsequently, hydrogen can be used for powering a wide range of applications, including highly efficient proton exchange membrane (PEM) fuel cells. The low density makes hydrogen storage and distribution a problematic task requiring large tanks, very high pressures, or an energy-intensive liquefaction process [30]. A compact, portable method of converting hydrocarbon fuels into hydrogen could address the lack of infrastructure for hydrogen supply. The ability to power a PEM fuel cell with a standard hydrocarbon fuel via the onboard fuel reformer can substantially improve the adaptation of fuel cell technology [30]. The on-demand production of hydrogen from commonly available fuels would improve hydrogen availability without the required infrastructural expanse associated with production and delivery networks.

1.2 Counter-flow Heat Recirculating Reactors

The operation of heat recirculating reactors relies on the efficient transfer of thermal energy between reactants and products. The fundamental idea guiding the counter-flow heat recirculating reactor design is shown in Figure 1.4. Two adjacent narrow channels share a common conductive wall. The gas in adjacent channels flows in opposite directions, with the heat being transferred via the wall. Heat is transferred through the wall from the hot products on one side to the cold products on the other, as illustrated by black arrows. The majority of the energy is exchanged transversely between adjacent channels, which substantially reduced the interaction distance. Some heat is redistributed axially within the same channel, although this effect is of lower importance. The wall conduction is supplemented by the radiative heat exchange between the solid walls. The unique characteristic of the counter-flow

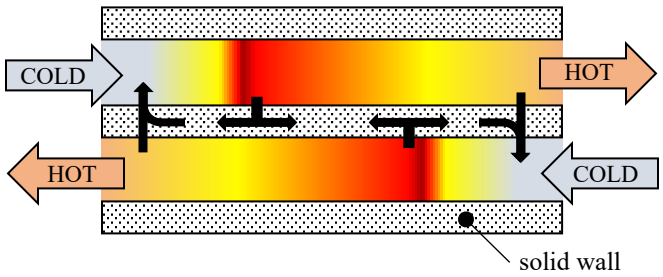

Figure 1.4: Simplified schematic of a counter-flow heat recirculating reactor

design is the ability to self-regulate. The preheating of incoming reactants increases the effective flame speed, which must be balanced by the local flow velocity for stable operation. The interplay between heat recirculation, flame speed, and local flow conditions creates a range of inlet conditions where the flame can stabilize at a fixed position. A mismatch between the flow velocity and burning rate results in the flame exiting downstream (blow-off) or upstream (flashback) of the reactor. Since the degree of heat recirculation strongly affects the burning velocity, stability is driven by heat

transfer. Additionally, the heat release rate remains an essential factor for energy-lean flows, where combustion can extinguish without exiting the reactor (extinction). Moreover, the stable flame position can only be achieved when there a positive separation between flame fronts in adjacent channels as shown in the stable configuration in Figure 1.5. The flame occupies a stable position at a given flow conditions because of negative feedback that restores the system stability. Once the flame crosses the adjacent flame position (the unstable configuration) any disturbance is further amplified, eventually leading to a blow-off. A range of analytical studies [6, 31–33] identified

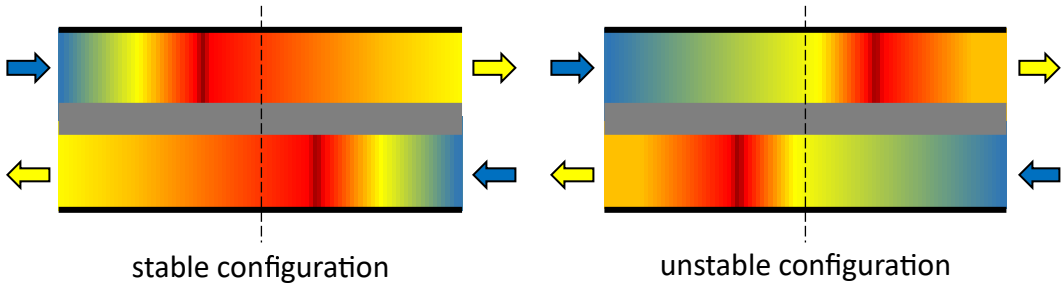

Figure 1.5: Example of stable and unstable operation of counter-flow heat recirculating reactor

wall conduction, internal convective heat exchange, and external heat losses as main factors in the stability of the reactor. Those findings were verified by further numerical [34–37] and experimental [38–42] examinations. The importance of internal heat convection favors high surface areas of exposed surfaces within the reactor. Meanwhile, the propensity of excessive heat losses has motivated the designs that reduce the external surfaces. Minimization of stray heat loss is fundamental for the efficient operation of any combustor. The most common designs addressing those goals have been presented in Figure 1.6. The original design is a folded "U" configuration, where hot exhaust gases are redirected to form a counter flow that heats reactants and shields them from external heat loss. There are multiple variants of the folded forms that were not shown, such as a single fold or axis-symmetric arrangement of concentric

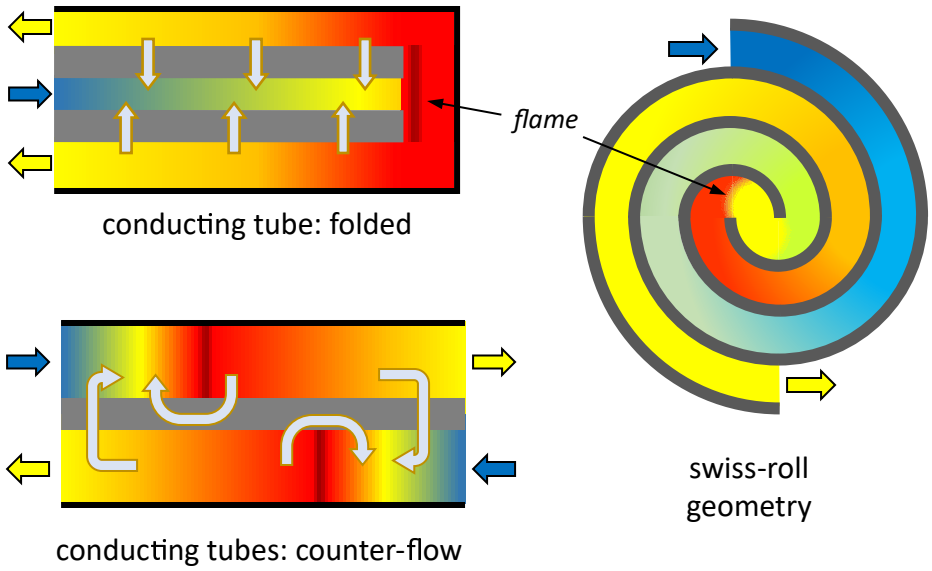

Figure 1.6: Various types of counter-flow heat recirculating reactors

tubes. The heat recirculation is achieved via long-distance axial conduction along the length of the inner wall and a short-distance transverse conduction-convection from flowing hot combustion products. The relative importance between the two depends on the convective heat exchange coefficient, by extension the characteristic Biot number. Higher convection has been found to increase the role of axial conduction within the inner tube [32]. The impact of thermal conductivity in a folded reactor was studied by Chen et al. [37]. It was found that thermal conductivity harms the overall performance. The heat recirculation has a substantial role in extending the operating range only with the low conductivity wall. Meanwhile, the high conductivity was detrimental due to enabling excessive heat loss. The exposed outer surface provided a convenient venue for the experimental examination of the fundamental role of heat loss and chemical heat release on flame stability. Maruta et al. [38] covered the outer channel with an external heat source, therefore finely controlling heat loss and recirculation. A substantial extension of flammability limits in Φ and inlet velocity was observed. This experimental result confirms that excess

enthalpy enhances the reaction rates enabling faster flow rates and combustion of less reactive mixtures. The swirl geometry, also called a swiss-roll, is another type of counter-flow reactor first introduced by Lloyd and Weinberg [43]. This design uses a single long channel that wraps on itself. This approach maximized the heat exchange distance while minimizing the external surface area [34]. The swirl geometry reactor retains previously discussed folded designs' properties with a significant role of low solid conductivity. Additionally, a high wall emissivity was found to have a detrimental effect on the reactor by increasing radiant losses without improving the internal heat transfer [44]. Overall the intricate geometry of swiss-roll reactors provided a superior stability range compared with other counter-flow designs [7, 39], bested only by a few types of porous-media devices [45]. The main difficulty in implementing this reactor type is a complex geometry combined with the need for ultra-high temperature materials. Furthermore, the circular geometry impedes the system scaling in practical applications. The most straightforward geometry is a counter-flow straight channel arrangement utilizing the separating wall for heat recirculation. The flame position in this design is only defined by the interaction between the gas flow and heat exchange. Flame positions itself in the position where the local burning velocity is equal to the flow speed of heated reactants. The flame velocity is substantially higher than the laminar speed due to heat recirculation. The analytical model [33] showed that the gas-solid convection governs the heat recirculation in this reactor type as the conduction mostly happens in the transverse direction. The numerical study by Belmont et al. [46] found narrower channels to be more efficient due to improved heat convection, which further supports the limiting nature of convective heat transfer. Meanwhile, the excessive axial conduction has the potential to hurt reactors' performance by increasing heat losses for high conductivity walls [6]. The heat loss remains a substantial stability factor causing a thermal quench within the

channels for high losses. The simple geometry allows for modularity with multiple channels operating as a single reactor. Such configuration external channels act as an insulation for the internal ones, which reduces the effective heat loss per-channel.

1.3 Previous work

The presented work is a continuation of an on-going investigation by Ellzey Combustion Group on straight channel reactors. Schoegl's work concentrated on the rich combustion and non-catalytic fuel reforming operations in counter- and co-flow configurations. The extensive experimental work on parallel-tubes combustor [40], Figure 1.7, was accompanied by analytical [6] and numerical [35] modeling that supported his findings. The reactor operated at the ultra-rich premixed mixtures for methane and propane. The experimental results showed high H_2 yields methane reforming and good flexibility on operating conditions. The analytical and numerical work identified the convective heat transfer and channel length as principal parameters controlling the counter-flow design performance. Furthermore, the counter-flow concept shown a better superadiabatic performance allowing for a wider range of operation. Schoegl's

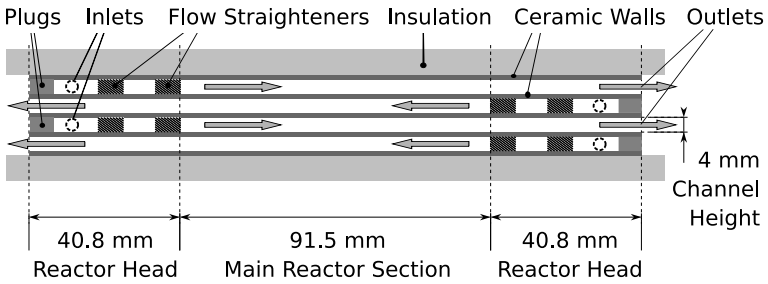

Figure 1.7: Schematic of counter-flow heat recirculating reactor used by Schoegl and Belmont [40]

work was continued by Belmont, who examined the parallel-channel design on a broader range of conditions. Rich combustion of liquid heptane was characterized to better understand the utility for higher hydrocarbons as a fuel source [47]. Subse-

quently, the lean combustion was investigated [42, 48]. The ultra-lean operation was established, indicating good fuel economy and low emissions. The experimentally obtained stability map for methane/air operation under lean and rich conditions is shown in Figure 1.8, where FB is flashback, BO is blow-off, and EX is extinction. It shows a relatively narrow range of stable operations without the capacity to operate near the conventional flammability limits. Finally, a numerical study was performed that analyzed the influence of reactor's length, and channel width on the superadiabatic combustion [46]. The pictures of the original reactor used in experiments are

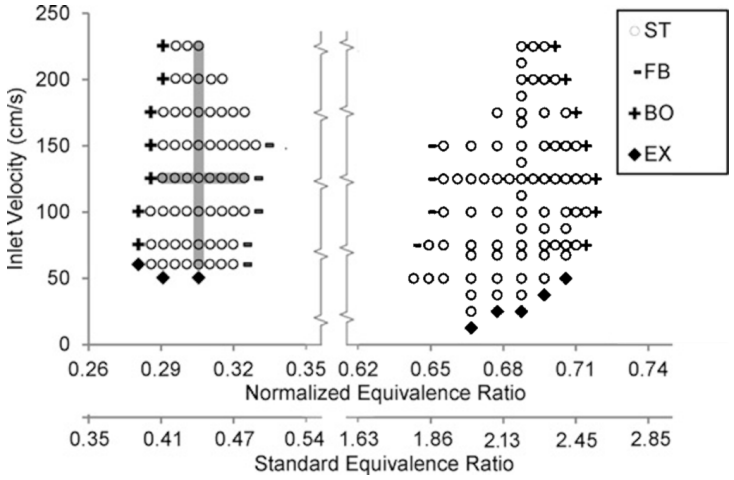

Figure 1.8: The operational range map for counter-flow reactor with premixed methane-air. Adapted [42]

shown in Figure 1.9. The entirely handmade assembly was created from carved zirconia blocks forming the top and bottom bases that housed SiC parallel plates. Each wall was made from five pieces of SiC due to supply limitations. This discontinuity has artificially reduced the axial conduction within the wall. The practical assembly is quite complex despite the conceptually simple flow path. A new manufacturing method utilizing additive manufacturing had to be investigated in order to achieve more intricate geometries.

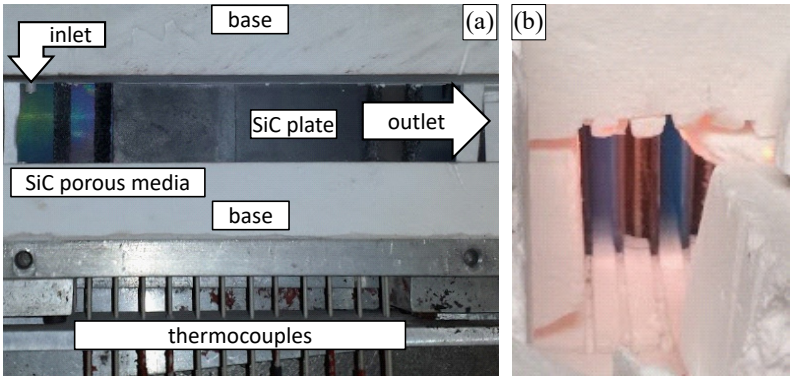

Figure 1.9: Pictures of Schoegl reactor: a) side, partially disassembled b) exits during operation

1.4 Objective

There are two main objectives for the presented research. Firstly the utilization of a new additively-manufactured material system is examined for use in combustion applications. Chapter 2 provides a detailed discussion on this topic. The combustion research objective is the examination the role of heat transfer in counter-flow parallel channel heat recirculating reactors under lean combustion conditions. The role of exposed wall surface area in the heat recirculation is investigated using freeform capabilities of additive manufacturing. The experimental activity aimed at establishing a steady-state range of operation. The combustion performance is evaluated at a range of inlet velocities and lean equivalence ratios Φ via temperature and emission measurements measurement.

1.5 Method

The combustion experiments on the actual reactors used a methane/air premixed mixture that has a well-understood combustion chemistry. The central part of the apparatus is the additively manufactured core section, where the combustion takes place. A custom support structure and instrumentation were used to monitor the

properties of interest. The modularity of this solution allowed for the examination of a range of reactor cores with different internal geometry. The goal of investigating the heat recirculation influence on combustion performance is achieved by modifying the channel shape. The simple straight channel is compared against a diverging channel geometry that reduces the convective heat exchange by increasing the width. The third studied configuration was a splitter-wall design that increased the wall surface area, improving the reactor's heat recirculation. Stability maps were established for all three configurations. The difference between the stable range of operations of those reactors identified the regions where increased or decreased heat recirculation was of the utmost importance. The addition of previous data collected handmade reactor [42] highlighted a significant change in the mode of operation with the new material. Wall temperature measurements further aided the comparison providing a more detailed picture of system conditions. An analytical model adapted from Schoegl [40] was used to understand the discrepancies. Finally, the emission measurements compared against equilibrium prediction provided insight on kinetic reaction changes with increased heat recirculation.

The feasibility of the materials process is evaluated based on the geometric reproduction capabilities and the degree of oxidation damage sustained over prolonged operation. A successful physical part was compared with the digital model, with the discrepancies tracked through the process. The improvements in processing allowed for better feature reproduction and a smoother surface finish. Each reactor has undergone a complete set of combustion experiments with the optical inspection for signs of degradation at even time intervals. The material-related change in reactor performance was tracked by repeated measurement at the same flow conditions throughout the device's lifetime. Furthermore, a detailed analysis of material degradation was performed in a separate combustion apparatus. Material samples were

placed at the lean flame interface inside the surface-stabilized ceramic combustor as discussed in Section 3.1.2. This configuration represented the most demanding application with flame interface impinging on the material surface. Samples were held at a constant temperature for a period of 10 hours and subsequently analyzed optically and under a scanning electron microscope (SEM). The energy-dispersive X-ray spectroscopy (EDS) showed the atomic change on the surface of the parts due to combustion exposure.

Chapter 2: Additive Manufacturing

2.1 High Temperature Materials

High-temperature materials selection is an important and mature topic of research. In principle, a higher temperature process allows for a more significant temperature difference between hot and cold reservoirs, hence improving the thermodynamic efficiency [49]. In terms of non-catalytic combustion, there is a minimum temperature required to sustain the flame's reaction rates. Depending on the fuel, this temperature is high enough to limit the material selection severely. An excellent review of high-temperature materials and the involved processes have been published by Ban-Cohen [50]. There are several factors important for the high-temperature selection [51]:

- ultimate maximum use temperature: usually the melting point, but can be a limit of thermo-chemical stability
- strength at temperature: many metals drastically reduce in strength above $\approx$ 1000°C or sooner,
- oxidation/corrosion resistance: the rate of deterioration at a highly energetic state
- creep behavior: long-term plastic deformation under stress greatly accelerated at high temperature
- thermal shock: response to high thermal stresses during rapid temperature changes such as ignition

In practical terms, high-temperature materials are classified for stressed (turbine blades, structural elements) or unstressed (combustors, heat exchangers) uses. Stress-

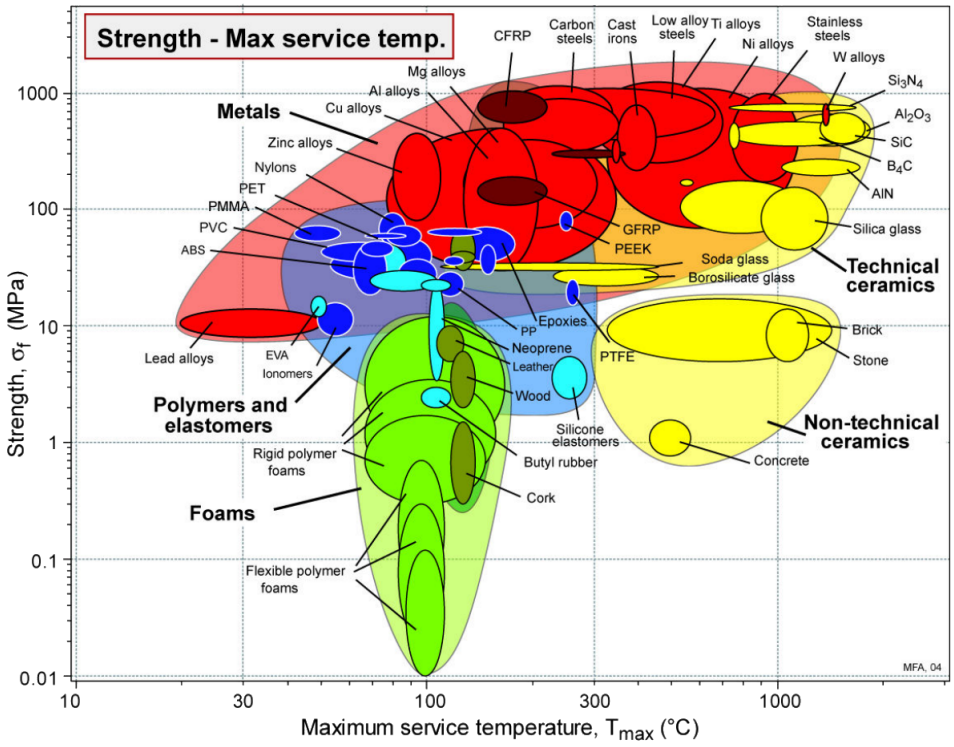

Figure 2.1: Ashby material selection plot for strength vs maximum service temperature [52]

dedicated materials have to withstand high mechanical loads with minimal creep in applications such as jet engines or structural applications at moderately high temperatures. The unstressed materials include combustors and heat exchangers where external parts provide structural integrity, and the goal for high-temperature material is to withstand the highest possible temperature for the longest time. The main topic of this dissertation is focused unstressed applications.

The common method of material selection are Ashby plots, named after the inventor Michael Ashby [52]. The relevant plot for strength versus maximum service temperature is shown in Figure 2.1. It identifies several material types of interest for combustion applications. The vast group of metals with the upper end of the high-temperature compatibility also showing a high strength. Therefore metals are

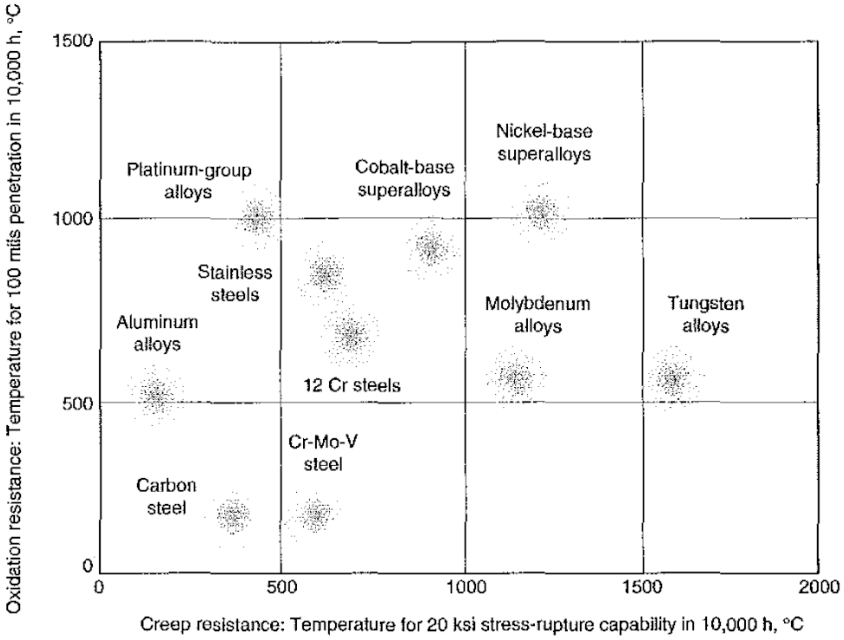

Figure 2.2: High temperature oxidation and creep resistance review of metallic materials [53]

the primary choice for high-stress high-temperature applications. Furthermore, the generally acceptable toughness and generally good machinability make them an attractive choice due to simpler shaping and processing. High-temperature metals can be subdivided into four major subgroups [51]: light metals (titanium, aluminum, magnesium, and their alloys), stainless steels, nickel or cobalt-based superalloys, and refractory metals (tungsten, molybdenum). Figure 2.2 shows the overview of metals in context of oxidation and creep resistance [51]. Light metals are an attractive choice, but their maximum use temperature is insufficient to be considered for combustion applications. Doped stainless steels provide excellent oxidation and corrosion resistance with temperatures suitable for specific low-temperature combustion applications [21, 41]. Unfortunately, their strength drastically reduces at temperatures. Superalloys have been developed for high-temperature service under stress, with the most advanced alloys reaching 1200° temperature, making them an attractive choice

for many combustion applications [11, 36, 39]. Finally, the refractory metals provide the highest operating temperature due to high melting points but have severe oxidation issues that require inert or vacuum atmospheres.

A particular type of high-temperature materials are carbon-carbon composites that provide the ultimate combination of strength, low weight, and temperature capability of any presented materials [50, 51]. However, their high cost and extreme vulnerability to oxidation render them incompatible for practical combustion applications.

Other popular type of high-temperature materials are technical and non-technical ceramics. Oxide, nitride, carbide, or boride-based ceramics can achieve significantly higher temperatures than metals while maintaining high strength. Boride-based ultra-high temperature ceramics can approach the operational temperatures of 2000°C in atmosphere [54]. Oxidation and creep resistance of ceramics are usually better than metal counterparts due to chemical and structural configuration. The main issue with ceramics is their high brittleness, which means their practical strength is driven by fracture rather than plastic deformation. The fracture mechanism is a complex topic that, in addition to material properties, also depends on the items' history and manufacturing process. Therefore, the strength is defined statistically by Weibull modulus [55] and stress intensity factors. Another issue related to high-temperature ceramic materials is manufacturing. Unlike metals, most technical ceramics cannot be melt-cast nor easily machined. The common method of high-temperature ceramic manufacturing involves dry pressing in purposely designed molds. This process has significant limitations on the final shape as the press has to distribute the pressure evenly. Certain ceramics can be extruded or injection molded with the use of plasticizers. Certain complex chemical processes can achieve intricate, yet random reticulated ceramic foams, which are commonly used in porous media combustors

[9, 10, 19, 56, 57]. The simple ceramic shapes are then used in assemblies that can accommodate their geometric limitations. Complex ceramic shapes are usually avoided due to the great difficulty of associated machining.

This work tries to utilize a new field of additive manufacturing to produce high-temperature ceramics directly in the final shape without the need for machining. Furthermore, the studied material, a ceramic-metal composite called a cermet, combines the high-temperature capabilities of a ceramic base matrix with the shape-preserving densification and machinability of infiltrating metal.

2.2 Additive Manufacturing: Laser Sintering Method

Additive manufacturing (AM) is based on building the desired object by addition of the material instead of subtraction. The process starts with an empty space where the desired material is deposited in a controlled fashion such that an expected geometry is obtained. This is unlike traditional manufacturing methods that begin with a volume of source substance, which is selectively removed to obtain the desired shape. The AM approach gives significant resource savings, improved output control and allows for more complex structures. There are various techniques available, including a popular fused deposition modeling, as well as highly sophisticated metal AM processes, including ultrasonic consolidation. AM of ceramics has been widely investigated over the last 20 years [58–61]. However, efforts to directly AM process engineering ceramics via a melt-and-solidify approach have universally failed due to the inability to avoid defect formation (voids) and cracking due to thermal stress [58, 62]. In this context, laser sintering (LS) is particularly attractive, as it is a proven technique that is capable of producing complex, sharp features in the milli- [63] and micro-size scales [64, 65]. The indirect approach significantly extends the capabilities of this system. Instead of fully melting the matrix particulate, a precise

mixture of unreactive ceramic and easily melted transient binder is processed in the LS device. The subsequent processing, outlined in Figure 6, replaces the binder with metal infiltration. This process is further discussed in the following subsections. The base LS process, shown in Figure 2.3, starts with the software representing the 3D model as a stack of individual solid slices. A powder mixture is loaded into the powder supply piston assembly. Through the process, a leveling roller distributes thin layers of powder onto the powder heated bed, where a computer-controlled laser selectively melts the thermoplastic-based on the current model slice. Once a layer is complete, a new thin-film the powder bed piston drops, a fresh powder layer is deposited on top, and the new layer slice is processed, as shown in the right of Figure 2.3. This process is repeated until a full part height is reached. This concludes the LS process with the final part embedded in the loose powder. Subsequently, the part can be excavated from the powder bed and the loose powder removed.

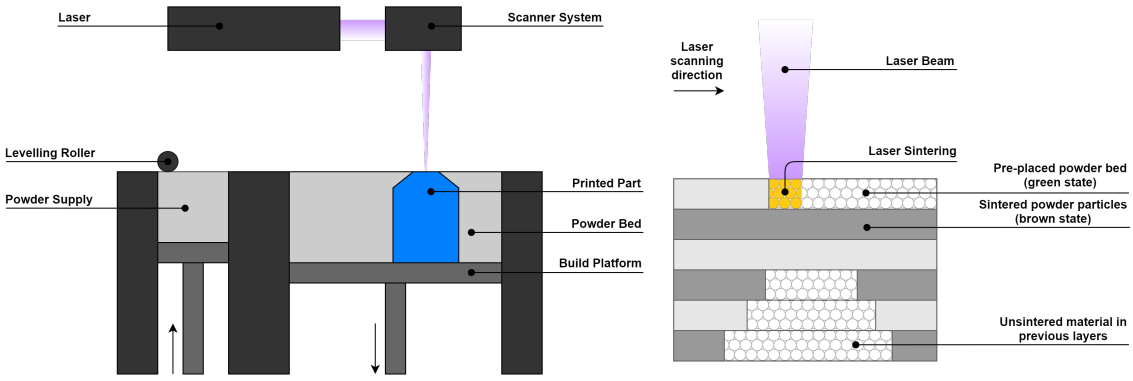

Figure 2.3: Process diagram of the SLS system [66]

2.3 Si-SiC Cermet

Cermet is a metal-ceramic composite produced by infiltration of ceramic preforms with liquid metal. The specific material of interest in the current research is silicon infilled silicon carbide matrix Si-SiC. The optical and etched SEM imagining of the

SiC material is shown in Figure 2.4. This particular material combination has the advantage of reactive melt infiltration, where molten silicon chemically reacts with carbon in the preform to form new SiC grains that further improve structural stability and SiC-to-Si ratio. The newly-formed SiC uses the existing grains as the nucleation sites, forming shells of fresh SiC around them, as seen in Figure 2.4b. Those shells eventually connect with the nearby grains, further improving the part strength. The degree of reaction bonding can be controlled by the amount of residual carbon in the ceramic preform. There is an upper limit to this process, where an excessive SiC formation obstructs the capillary channels before all voids are infiltrated [67] leading to a weaker part.

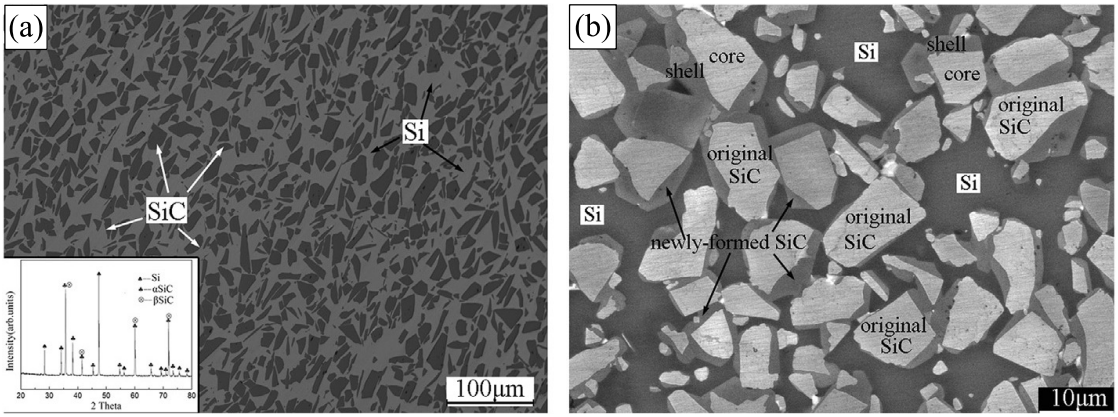

Figure 2.4: Morphology photographs of Si-SiC cermet [67] a) optical b) SEM

The Si-SiC cermet material was developed before the advent of additive manufacturing [68, 69] with the ceramic preform manufactured via traditional methods. The early review of REFEL brand Si-SiC used in cladding applications for UK nuclear reactors [68] identified the materials' exceptional mechanical and physical properties at high-temperature applications. Si-SiC has a high strength, which remains invariant with temperature until the melting point of the infiltrant. The high surface hardness of SiC is preserved, leading to excellent abrasion resistance. With the low thermal

expansion and good thermal conductivity, the Si-SiC material is highly resistant to thermal shock and thermal stresses usually present in combustion applications. A good oxidation resistance has been reported by Kennedy and Shennan [68], and an in-depth study of the oxidation behavior of Si-SiC was performed by Ernstberger et al. [69]. It has been found that Si-SiC undergoes passive oxidation that, upon sufficient oxide layer growth, significantly reduces the rate of material oxidation. The mass gain versus time plot for Si and Si-SiC material is presented in Figure 2.5. Si-SiC samples have lower oxidation rates than pure Si metal due to a substantial fraction of SiC grains on the surface. Notably, the oxidation of Si-SiC becomes active at partial oxygen pressures below 10^{-4} bar, which should not be an issue for the majority of combustion applications at atmospheric pressures. The high water content of combustion gases is of concern as the water molecules react with SiO_2 scale, forming gaseous orthosilicic acid $Si(OH)_4$. This process is known to overpower the SiO_2 formation under predominantly water vapor atmospheres. The effect of water pressure present in lean combustion exhaust gasses on Si-SiC material should be investigated.

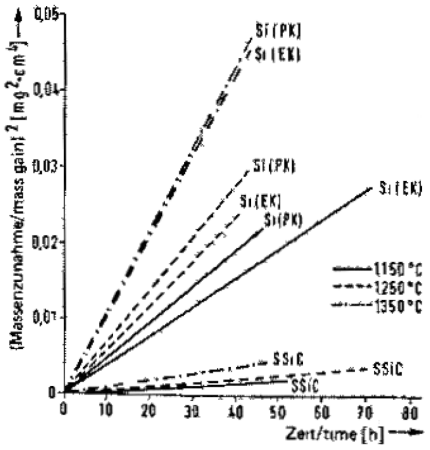

Figure 2.5: Oxidation mass gain rate for polycrystaline Silicon (PK), monocrystaline Silicon (EK) and Siliconized Si-SiC at various temperatures and atmospheric pressure [69]

The presented Si-SiC properties are specific to the material created via traditional methods. Additive manufacturing uses unique processing that can alter the internal morphology of the part. Since the material performance at high temperatures is strongly dependent on the internal structure, the common knowledge presented before should be considered only as an overview. The performance of the AM manufactured Si-SiC has to be evaluated independently as the resulting morphology difference can impact the physical and thermal properties.

This study concentrates on additive manufacturing and non-structural applications of Si-SiC cermet in combustors. Therefore no structural strength data was taken. There was a particular interest in AM Si-SiC oxidation resistance and applicability for flame exposure due to its intended use in combustion devices.

2.3.1 Si-SiC In-Direct Sintering Process

The indirect laser sintering approach used in the current work is illustrated in Figure 2.6. Figures 2.8 and 2.9 show photographs taken through all steps of the process.

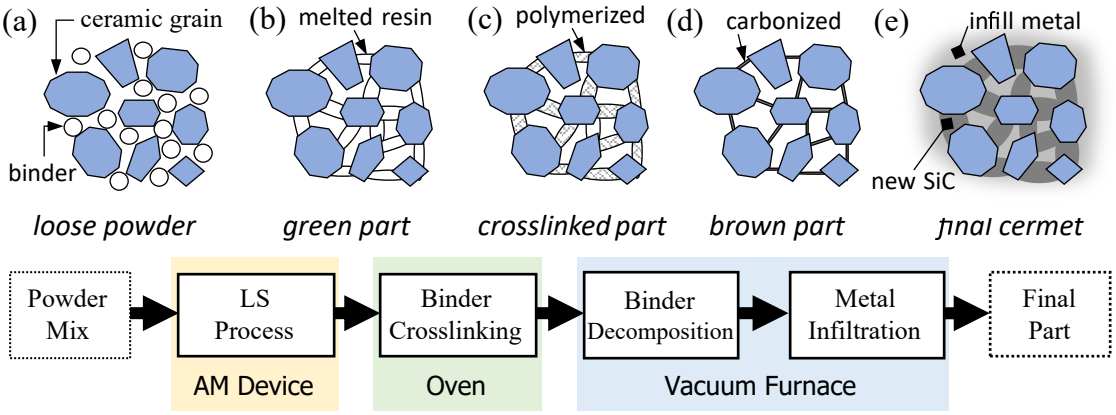

Figure 2.6: Schematic of AM Si-SiC process: indirect laser sintering with metal infiltration

Initially, the ceramic, typically in powder form, is mixed with a binder suitable for AM processing (2.6a, 2.10). The details on powder sourcing and mixing are

provided in section 2.3.2. In the AM step, the phenolic binder is activated to hold ceramic particles together, creating a green part (2.6b, 2.8a). The feedstock powder mixture is kept at a temperature just below the melting point of the binder to reduce thermal stresses and curling of sintered layers. At each layer, the part slice is inscribed by continuous-wave CO_2 laser that selectively melts the powder 2.8b). The laser power of 40W with contouring power of 45W provided the best geometric reproduction and green part strength. Upon finishing the build, the green part is retrieved from the LS machine, and the loose powder is removed (2.8c). This is a delicate operation as the bonding strength of the binder at this stage is very low. A special technique with miniaturized air blasting assembly was developed (2.8d) that included a 10 inch long, 14 gauge needle used for clearing internal channels of the experimental reactor. The microstructure of the green part is shown in Figure 2.7a. Once all loose powder was removed, the phenolic binder had to be crosslinked (thermoset) to prevent remelting at higher temperatures (2.6c). This is a complex process described in section 2.3.4. Once crosslinked (2.9a), the part also gains sufficient strength to allow safe handling. The crosslinked green state is the most suitable for making any modification, such as drilling holes or wall carving. The following is a burn-out step, where the binder is carbonized (2.6d) into 50% remaining carbon in the form of bridges holding the part together. This process takes place in the vacuum furnace with a maximum temperature of 900°C. The exact temperature and pressure log used in fabrication is shown in Figure 2.14. A slow 50°C/hr ramp is required until 500°C to allow the decomposing gasses to escape without damage to the part. Most of the resin has been transformed at 500°C, hence it is safe to perform a quick 400°C/hr ramp-up to 900°C allowing the residual amounts to carbonize fully. The result is a ceramic preform, generally referred to as a brown part. Figure 2.7b shown the SEM photograph of carbonized brown part. If carbon is undesired for further processing, a non-ash binder

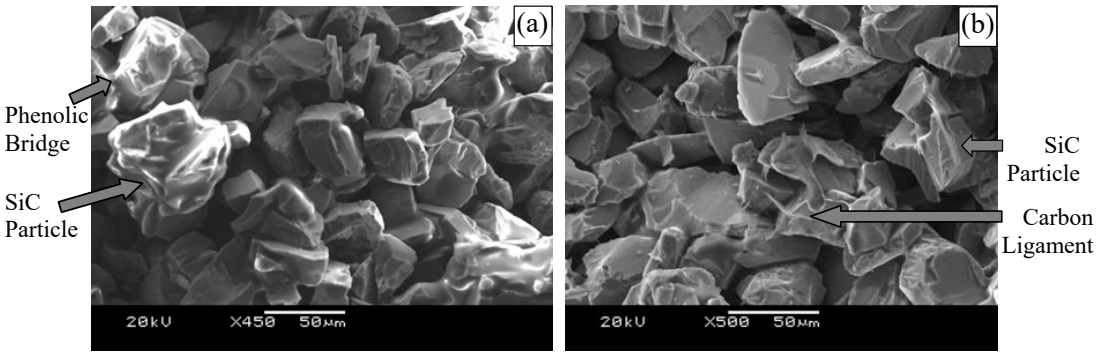

Figure 2.7: Microscopic images of Si-SiC processing stages [70]: (a) SEM green part (b) SEM brown part

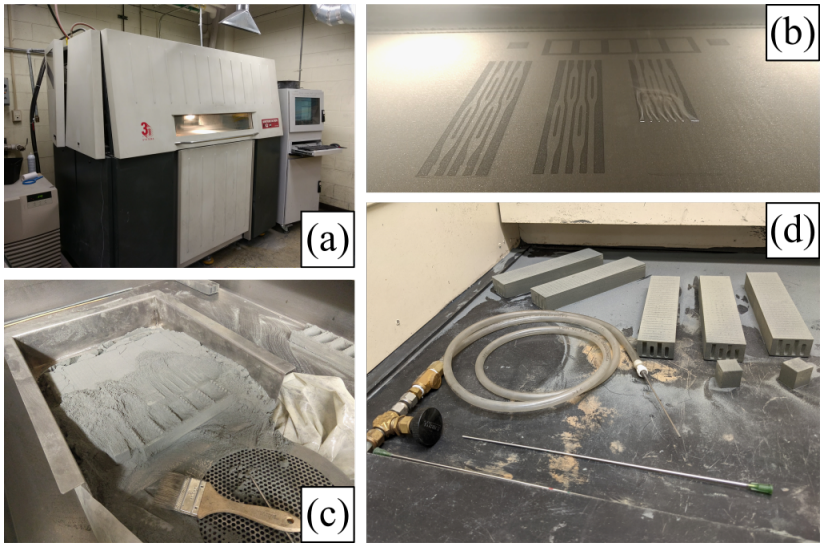

Figure 2.8: Pictures of SLS processing: (a) Sinterstation HiQ device (b) Laser inscribing a new layer (c) rough excavation stage (d) fine excavation stage of internal cavities with compressed air

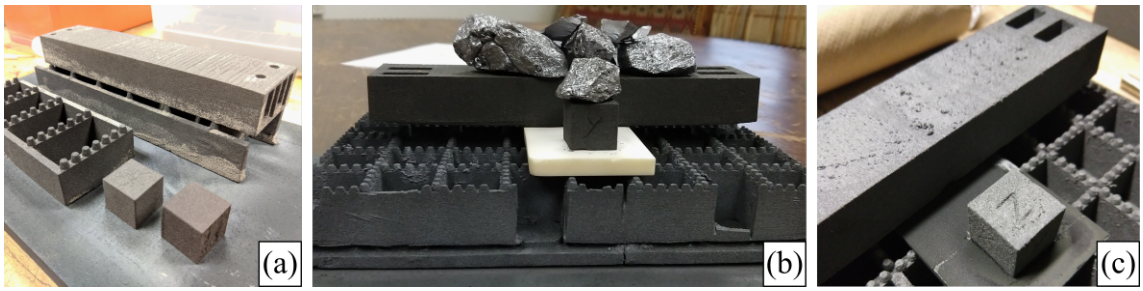

Figure 2.9: Pictures of infiltration processing: (a) crosslinked part setup (b) infiltration assembly with brown parts (c) final parts

can be used (nylon, PMMA), which will completely decompose to gaseous products at this stage. Therefore this approach would require an external means to retain the shape, such as submerging the part in a separate bed of inert powder. In an alternative scenario, the brown part is subsequently heated to a high temperature and sintered to create a pure ceramic piece. While the part would have intrinsic properties of the neat ceramic, it would also experience a significant (>10%) shape change with resulting distortions. There is also residual porosity involved, which reduces the mechanical performance of the part. The solution used in this study infiltrates the part with a suitable infiltrant (2.6e). The assembly of brown parts and metal chunks prepared for the infiltration step is shown in Figure 2.9b. In the case of the Si-SiC system, when molten silicon contacts the carbon binder residue, more silicon carbide is formed. Because there is negligible sintering shrinkage, the dimensional accuracy is largely maintained, as discussed in the geometric capabilities section 2.3.3. The final result is shown in Figure 2.9c. The detailed infiltration process is described in section 2.3.5.

2.3.2 Powder Preparation

The powder for the LS processing is a mixture of SiC and binder particles. Powder flowability is an important factor for successful LS processing. Based on the previous research [70, 71] the optimal grain sizes were identified as $\approx 45\mu$m for SiC and $<10\mu$m for the binder particles. Therefore 280 grit SiC powder (average particle size 39-44μm) was ordered from a commercial sandblasting abrasives supplier. There are two types of SiC powder available: black and green. The difference lies in the chemical processing with the black SiC powder containing a carbon residue on the surface. The green SiC powder was selected due to its purity, which improved the process control. A phenolic binder is chosen due to carbon residue deposition upon thermal decomposition, which is desirable for reactive Si infiltration. GP-5546 phenolic resin

was obtained from Georgia Pacific Resins, Inc., and attrition milled down to the size of 10μm. SiC powder and phenolic binder were combined at a 100:10 weight ratio and mixed in a ball mill with alumina grinding medium for 12 hours. The SEM photograph of final powder is shown in Figure 2.10. The higher magnification, Figure 2.10b, allows easy identification of finer binder particles among the bigger and coarser SiC grains.

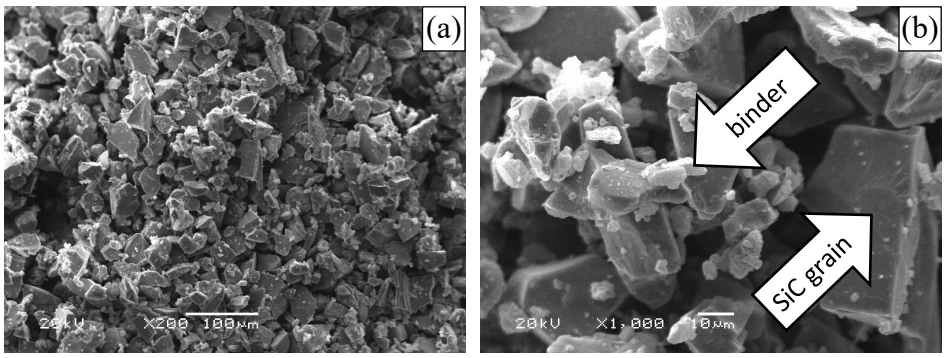

Figure 2.10: SEM image of the source powder mixture used in the process: (a) 200x zoom (b) 1000x zoom

The powder prepared in this process is ready for use in the SLS device. Upon completion, a sifting on 280 mesh sieve is recommended prior to reusing the powder in another print. Furthermore, it is advisable to periodically mix the powder in the ball mill, especially after prolonged storage.

2.3.3 Geometric Capabilities

The model reproduction via laser sintering into a green part has a resolution of approximately 1 mm. The minimum feature size in the layer plane (X-Y) is fundamentally limited by the laser spot's focus diameter in laser sintering - 0.5mm diameter in the case of Sinterstation HiQ used in this study. However, the high conductivity of the powder causes wider hotspots, limiting the minimal practical feature to approximately 1 mm. The cross-layer (Z) features are limited by layer thickness, which can

be as low as 0.05 mm. The curling of melted parts and vibration introduced by the powder deposition system limited the vertical features to 0.5 mm in practice. Further research and thermal modeling are required to enable reliable sub 1 mm feature sizes. It should be noted that presented limitations are machine-specific, with other teams successfully achieving a microfeature reproduction [65].

The subsequent processing steps introduce their own limitations to achievable geometric features. The highly fragile green part produced by LS has to be removed from a powder bed via mechanical methods. The most challenging part is a clearing of the internal channels, with the usual success rate of this step for presented designs being $\approx 25\%$. Although thinner separating walls can be reproduced via laser sintering, the channel clearing process is likely to become an impossible task due to the low green part strength. Another limitation is the metal infiltration with the affinity to bridge narrow gaps and smooth (fillet) sharp corners due to high surface energies.

The current study has produced a set of reactors with the narrowest wall of 2 mm and the channel width of 3 mm. Furthermore, a 1 mm 45° chamfers were the wall corners, and the 1 mm radius fillets on the leading edge of the splitter wall (split-channel reactor) were successfully created. The thermocouple holes at the bottom wall were 4 mm in diameter, which required resizing in the final part due to partial obstruction by the infilling metal.

The external dimensions of the split-channel reactor were tracked through the manufacturing process. The relative size change compared with the CAD model is presented in Figure 2.11. The CAD-green step, involving the laser sintering processing, shows a 3% increase in the layer plane and 2% growth in the cross-layer direction. This change is a stable feature of the laser sintering process usually accounted for by the software prescaling for the expected volume changes. A subsequent 4% decrease in the vertical Z direction between green and brown stages is associated with the

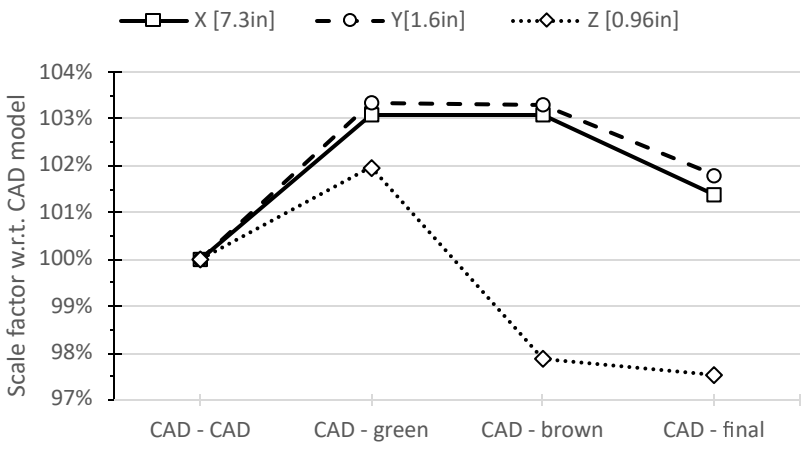

Figure 2.11: Geometric variance from the CAD model along various stages of the process in the three primary directions

crosslinking step. There a short period of material softening allowed the gravity to compactify the part in the vertical direction, section 2.3.4. This issue can be prevented in the future by better control of the crosslinking process or preemptive model scaling during the LS step. Finally, there is ≈1% decrease in all directions during the infiltration step. All volumetric changes thorough the process are significantly lower than during the ceramic densification methods.

2.3.4 Green Part Crosslinking

Phenol formaldehyde resins used as a binder are two-stage thermosetting polymers. Phenol monomers are branched together via the formaldehyde group, which drives a full-strength in the crosslinked resin form. GP-5546 used in the study is a novolac resin type that, by design, contains an insufficient amount of formaldehyde to react with the available phenol groups fully. The result is a mixture of poorly interlinked and short phenolic chains in the form of a yellowish solid that easily crumbles into a fine powder. The unreacted phenolic resin softens and flows at temperatures between 80°C and 105°C. The formaldehyde required for completing the polymerization pro-

cess is released by thermally activated donor chemical hexamethylenetetramine (hexamine) blended within the powder (7% by volume). The crosslinking process occurs at temperatures above 90°C and is greatly accelerated at higher temperatures. The ability to melt without fully crosslinking is an important feature for laser sintering, where repeated remelting at consecutive layers is necessary for intra-layer bonding. However, this also brings the requirement of subsequent processing. A dedicated, well-controlled crosslinking step is required to preserve major features and overhangs from melting when exposed to high temperatures.

The original "shock" method placed the green part into a preheated oven at 250°. A high thermal gradient aimed at reducing the residence time at the intermediate temperature was meant to minimize the plastic flow. This approach worked reasonably well for the majority of shapes, although unsupported overhangs were severely affected. A set of thin 100x20x2 mm samples was printed and used to evaluate this method at various unsupported bridge distances. Figure 2.12a shows the crosslinking outcome for a shock method. The 1.5" long bridge failed, while the narrower distances visible in the background (1", 0.75", 0.5") show a severe deformation. Two approaches were used to maintain the structural integrity during shock-based crosslinking. The first method infiltrated the green part with a self-hardening epoxy resin that held the shape through the crosslinking period. A 50:50 volume mixture of resin with xylene was used to aid infiltration by reducing the liquid viscosity. The epoxy was eventually removed by a thermal dissociation into gaseous species during the bake-out process leaving the metal infiltration process unaffected. This method preserved the part features well but was time-consuming and harsh on the bake-out step's equipment. Therefore an alternative method was favored with the part embedded in the inert media that provided mechanical support. Fine white silica sand rendered satisfactory results, but the surface finished was affected by sand grains that

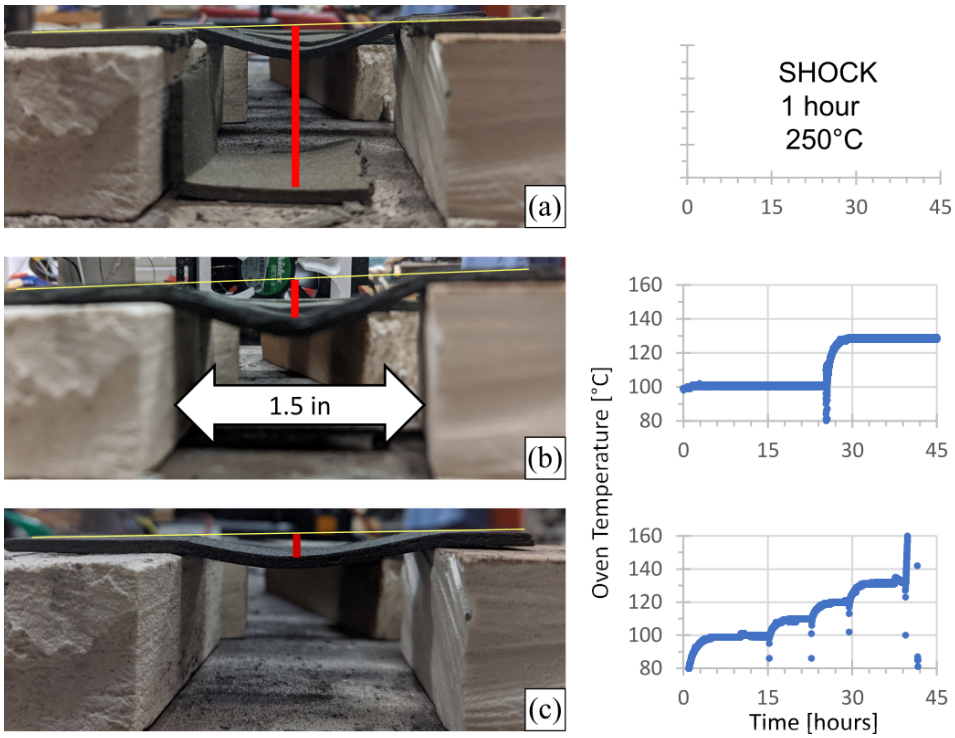

Figure 2.12: Phenolic binder cross-linking method with the resulting deformation of unsupported bridge: (a) original shock method (b) 2-temperature slow approach (c) temperature ramp

adhered to part surfaces, as seen in Figure 2.9a. Importantly the internal cavities had to be filled with sand, which was a challenging task due to the low strength of the green part before crosslinking.

The technical support from Georgia Pacific suggested an alternative crosslinking strategy. Both formaldehyde release and phenol polymerization processes are thermally activated processes with rates growing exponentially above the threshold temperature. Nonetheless, the lower temperatures still enable crosslinking, just at a reduced pace. Therefore a slower heating approach can improve the geometric preservation as the premature crosslinking is allowed sufficient time to provide the necessary strength. The new approach was tested using the test samples with results presented in Figure 2.12b for a simple 2-step attempt and Figure 2.12c for the es-

tablished process that approximates a 1.25°C/hour ramp. The testing bridge section has only a minor deformation over a 1.5" distance, which is an excellent prognosis for the actual parts. This approach was established in time for processing the most geometrically complex split-channel design. The ability to crosslink the part without epoxy infiltration or sand embedding was a critical step in successfully reproducing 2 mm internal feature sizes present in this geometry. Interestingly the track of geometric changes of the part, Figure 2.11, shows a significant 4% decrease in the vertical Z direction between green and brown stages with no change in the other two major dimensions. This vertical change is likely an outcome of the crosslinking step, where the unsupported part uniformly shrunk due to gravity.

2.3.5 Metal Infiltration

The metal infiltration of brown parts takes place in the vacuum furnace capable of reaching at least 1500°C. The brown part is positioned on a stand and surrounded by 99.5% pure silicon chunks, as shown in Figure 2.9b. The role of the stand is to contain the melt pool and provide a wicking path for molten metal. Therefore the stand is made of the same material as the main part. Successful pressureless metal infiltration into a ceramic preform requires a favorable wetting angle of the metallic melt on the preform. The driving force is related to surface energy and is historically described using the Washburn Equation for traditional capillarity. Cornie [72] in the late 1980s modified the Washburn Equation to account for a liquid wetting and to infiltrate into a porous powder mass:

$$P^* = \frac{6\lambda(-\gamma_{lv}\cos\theta)\Delta}{(1-\Delta)D}$$

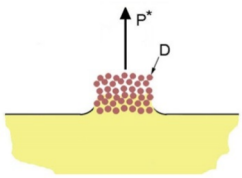

Figure 2.13: Cornie's infiltration theoretical basis for liquid wetting

where P* is the effective driving pressure, λ is a geometry factor, γ_{lv} is the liquid surface energy, θ is the wetting angle, Δ is the porous preform apparent density divided by its theoretical density and D is the particle diameter. In the schematic, the lower (yellow) region is the molten metal being drawn by the effective pressure P* into the porous preform (brown) of particle size D. The predicted driving pressure for Si - SiC pair is sufficient to infiltrate the part over a 1.5m distance from the original melt pool. However, the clogging of capillary paths by the newly reacted SiC [67] is possible. Hence an extensive contact surface between melt and preform is recommended. The conical tops on the stand provide many paths for melted silicon to travel into the part while minimizing the contact area per connection. This approach helps with the removal of the supporting structure glued to the part by solidified metal. The small cross-sectional area of joints and relatively high brittleness of pure silicon allows for fracturing the stand from the main part with an impact. The temperature and pressure history during the infiltration process is shown in Figure 2.14. The initial warm-up is quite fast at 300°C/hr up to 800°C followed by 200°C/hr ramp to 1400°C, which is just below the melting point of silicon. The final melting is performed at 125°C/hr ramp to 1550°C followed by a 1-hour isothermal hold and a controlled cool-down back to 1400°C at 75°C/hr rate. Additional controlled cooling step down to 1100°C at 200°C/hr rate reduces thermal stresses within the part. Finally, the furnace is allowed to cool down naturally to room temperature. The silicon is heated 136°C above its melting temperature to reduce the melt viscosity, which aids the infiltration. The disadvantage of this approach is the increased partial pressure of silicon, as registered in the pressure plot. In the initial experiments, the oven was heated to 1650°C, at which point the rate of silicon vapor reaction with graphite furnace elements was high enough to form a visible scale after a single infiltration cycle. The issue is substantially alleviated at 1550°C, where multiple

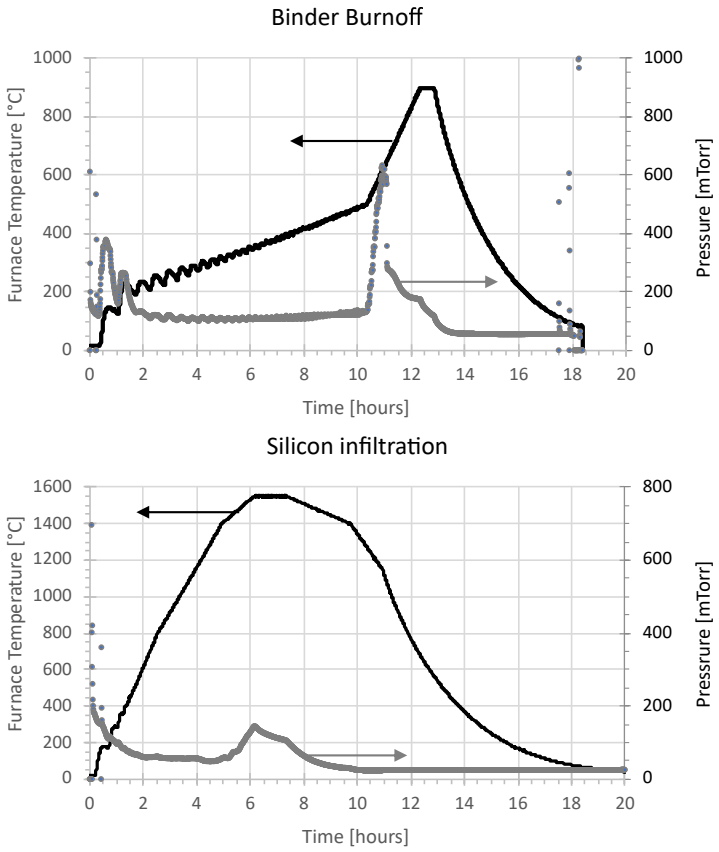

Figure 2.14: Temperature and pressure plots for vacuum furnace processing

infiltrations did not show any degradation to graphite elements.

The Si-SiC composite suffers from over-infiltration if the ratio of silicon to porous preform is not properly controlled [73]. The metal protrusions are caused by Si expansion during solidification, as seen in Figure 2.15a. The surface energy minimization makes excessive silicon collect in sharp corners and obstruct small features such as holes or overhangs. In extreme cases major pooling and blockages take place, Figure 2.15b. The overfilling issues can be avoided by using the exact amount of silicon required to fill the internal part porosity when solid. The part porosity is estimated based on pycnometer measurement for the true solid volume and the bulk volume of the shape obtained by part dimensions or the Archimedes principle. An

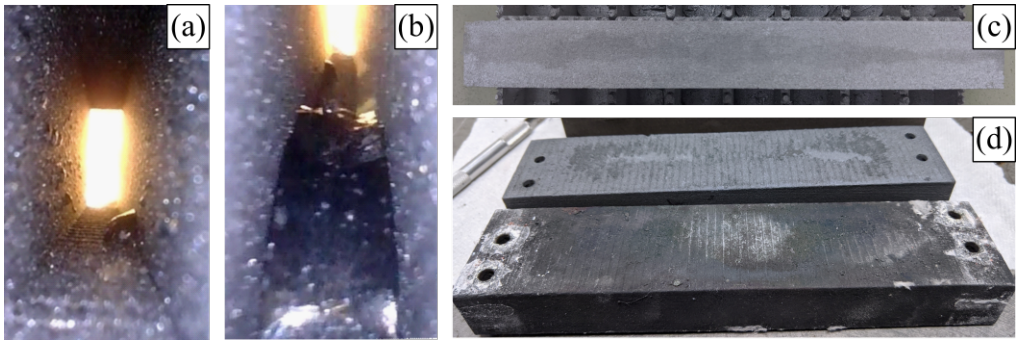

Figure 2.15: Possible imperfections of the cermet process: (a) Si protrusions (b) Si pooling (c) incomplete infiltration (d) influence of processing atmosphere

indicator cube, Figure 2.9, was manufactured and processed alongside each part for this purpose. Once carbonized, the external dimensions of the cube were determined to obtain the bulk volume. Subsequently, a pycnometer was used to measure the actual solid volume. The difference between the two is a void volume that has to be filled by the silicon metal. The resulting porosity is subsequently used to calculate the required mass of Si to infiltrate the actual part. This approach assumes full utilization of the provided metal and neglects the volume change when a denser SiC is formed during reactive infiltration. In practice, those issues often led to an incomplete infiltration, as shown in Figure 2.15c. In such case, the infiltration had to be repeated until the target mass (preform mass + required Si mass) was achieved in the final part. Usually, a successful infiltration required two high temperatures cycles to reach $\approx$ 95 - 98 % relative density with closed porosity.

The processing temperature affected the finish of the final part, as shown in Figure 2.15d. Under nominal conditions (<200 mTorr), the final parts are bright gray with metallic flashes of pure Si within the structure (upper part). During the straight channel combustor processing, a broken valve resulted in the processing pressure increased to $\approx$ 2 Torr. The new atmosphere mainly consisted of nitrogen and CO from oxidizing the graphite liner. The final part, the lower one in Figure 2.15d,

is significantly darker than the normal Si-SiC, which indicates the presence of excessive carbon on the surface. The black color remained through the complete set of combustion tests but did not influence the reactor's performance.

2.4 Future Work

Future work on the Si-SiC system should concentrate on thermal and physical properties at high temperatures and the long-term oxidation resistance of additively manufactured specimens. Physical strength at temperature and detailed fracture behavior is required for designing new, reliable components. Thermal properties used in this study were assumed as a linear combination of Si and SiC-based on the mass fraction; however, this assumption should be experimentally tested. Finally, a long-term oxidation study is required to assess the oxidation lifetime of cermet parts and the creep behavior.

The preliminary oxidation tests identified two modes of material deterioration: unstable oxide spalling and molten silicon protrusion. The potential solution for increasing the maximum operating temperature is a zirconium-based material system discussed in section 2.4.1. Meanwhile, the increased oxidation rate at temperatures below 1200°C needs to be addressed to accommodate the flexibility required by combustion devices. The root cause of this behavior is a structural change in SiO_2 around the glass transition. The threshold temperature can be depressed by surface additives forming low concentration alloys with SiC, Si, and SiO_2. A prominent candidate is elemental boron, which oxidizes to boron trioxide B_2O_3, an amorphous glass that readily melts at 450°C-510°C and does not boil until 1860°C. A molten boron oxide provides a diffusion barrier to oxidation and can stabilize the spalling SiO_2. Furthermore, the chemical interaction between the two oxides has been shown to further improve oxidation resistance in ZrB_2-SiC systems [74].

An additional goal would be to investigate the use of metal infiltration as a bonding solution. Specific complex shapes can be printed as a set of components to aid the delicate LS process. Once cleaned from the loose powder, the parts can be reassembled prior to infiltration. The wicking action of ceramic preform should bridge the small gaps and therefore bond pieces together. The strength and composition of the bond should be analyzed and reported. This process, if successful, can also be applied to produce superior interfaces between cermets and other materials.

2.4.1 Zirconiated Zirconium Diboride Cermet

Zirconium diboride infiltrated with zirconium, Zr-ZrB_2, is an attractive candidate to replace the Si-SiC system. While the AM indirect processing of Zr-ZrB_2 composites is novel, researchers have shown that the critical step of infiltrating the metal into the ceramic for this particular case is possible [75, 76]. Phenolic binders have proven successful as a high-temperature binder leaving behind a small amount of residual carbon. It is expected that this carbon will eventually react with infilling Zr metal and form zirconium carbide ZrC. This molecule has been proven to be a beneficial additive for oxidation resistance of ceramic parts [77]. A modified binder system based on a mixture of phenolic and polyamide (no carbon residual) can optimize the ZrC fraction in the final part. Notably, the zirconium contracts upon solidification, unlike the currently investigated silicon that expands. This should prevent over-infiltration issues. The zirconium diboride based systems has been shown to operate at 1200°C - 1500°C range for moderate times [77–79]. The ultimate temperature limit is the melting temperature of zirconium of 1855°C. Figure 2.16 overlays the infiltrants temperature limits on the adiabatic flame temperature of methane-air flame. The new zirconium-based cermet system substantially extends the material applications in the combustion field. Unfortunately, the infiltration of currently established SiC preforms

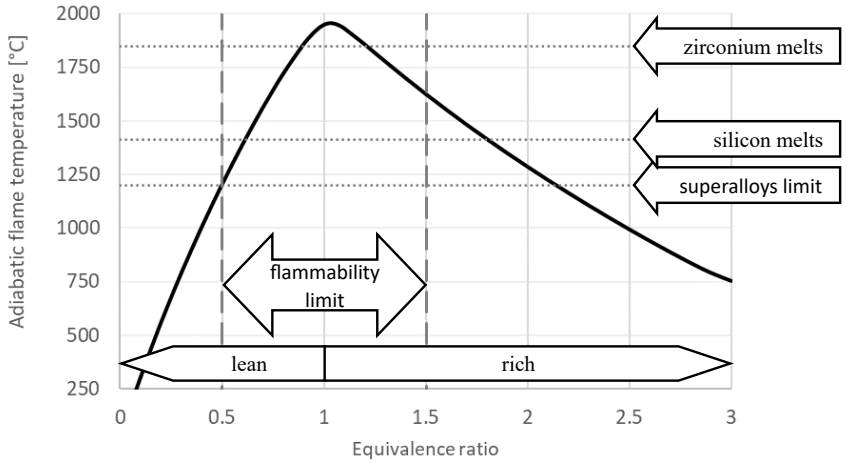

Figure 2.16: Adiabatic flame temperatures compared to maximum operational temperature limits of various metals

is not possible. Based on the Ellingham diagrams, the ZrC has higher bond strength than SiC over the whole temperature range. That means the Zr infiltration attempt on SiC would result in breaking the SiC into ZrC and a variety of Zr-Si alloys or intermetallic compounds instead of a hypothetical ZrSiC. Therefore a ZrB_2 ceramic preform is required for zirconium infiltration.

Chapter 3: Examination of Si-SiC reactor

The material performance and the utility of freeform capabilities of cermets in combustion applications. The results will be used to design heat recirculating reactors with improved performance. The experimental apparatus consisted of two major components: the AM core and the support equipment. The combustion core was the active part of the device, where the combustion took place. Meanwhile, the external equipment provided structural support, instrumentation, and flow-controlled premixed air-fuel delivery to the inlet pipe of the core element. This modular approach allowed for accommodating a variety of AM printed cores that explored a range of geometric changes while minimizing external systems variability. A detailed description of support equipment is provided in section 3.1.1. A total of three AM designs were tested, starting with a simple straight channel section 3.3, that was adapted from the previous reactor studied by Schoegl et al. [40] and Belmont et al. [48]. The results of research on this geometry were published as [80][1]. Using the AM straight design as a base-case, two subsequent geometries were created to explore the relationship between heat exchange and stabilization. A diverging channel design, discussed in section 3.4, implemented a channel width expansion, which locally decreased the flow velocity and reduced the wall surface area to channel volume ratio $R_{A/V}$. This geometry was presented at a meeting of The Combustion Institute in 2019 [81][1]. Finally, a split-channel design, 3.5, increased the heat exchange by introducing

[1]In the listed bibliography items, the author has performed all presented work and has written the entire publication. Co-authors have advised the primary author through the process and provided feedback on the written part. Analytical work in Chapter 3.2 is based on Dr. Schoegl's original, published work. All the results and required modifications to the computer model are the current author's own work.

a fin in the middle of the channel hence increasing the available surface area and $R_{A/V}$. The performance for all reactors is compared in section 3.6, together with the analytical model predictions[1]. The results from the split-channel geometry along with a complete comparison of all geometries were the subject of a publication in Combustion Science and Technology [82][1]. For all experiments, a premixed methane/air was used at various velocities and equivalence ratios. Each combustor was operated for an extended time to evaluate the material degradation under the typical application. Furthermore, dedicated flame exposure experiments were performed (section 3.1.2), where the Si-SiC test sample was exposed to an impinging flame at two temperature levels for 10 hour period. Section 3.7 present the results of those experiments.

3.1 Experimental Methods

3.1.1 Combustion Apparatus

The combustor was assembled inside a purposely built combustion stand with a dedicated negative ventilation system and full encasement by over-pressure resistant plexiglass panels. The main part of the combustor, where the flames are stabilized, is manufactured using AM as described in chapter 2, later referred to as an AM core. A detailed discussion of the internal structure of each AM core is included in the respective subsections for straight, diverging, and split-channel designs. There were two iterations of the external support mechanism. In the early experiments involving diverging reactor, section 3.4, the core was fully enclosed by refractory brick, as shown in Figure 3.1. Further details on this setup are provided in section 3.4.2. This arrangement was characterized by a long warm-up time due to a high thermal mass. Therefore the improved design was incorporated, shown in Figure 3.2.

The installed AM core rested on two zirconia insulation blocks, suspended

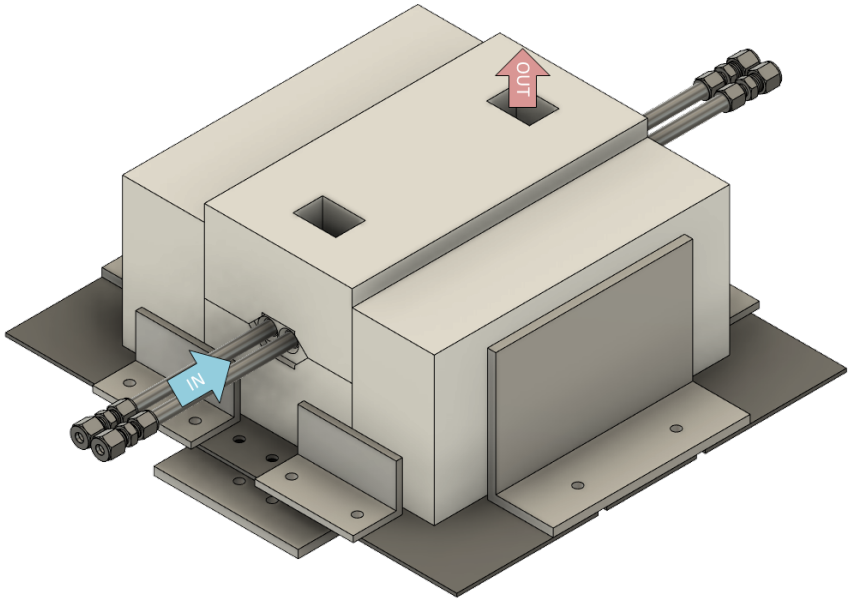

Figure 3.1: Early experimental apparatus - structure overview

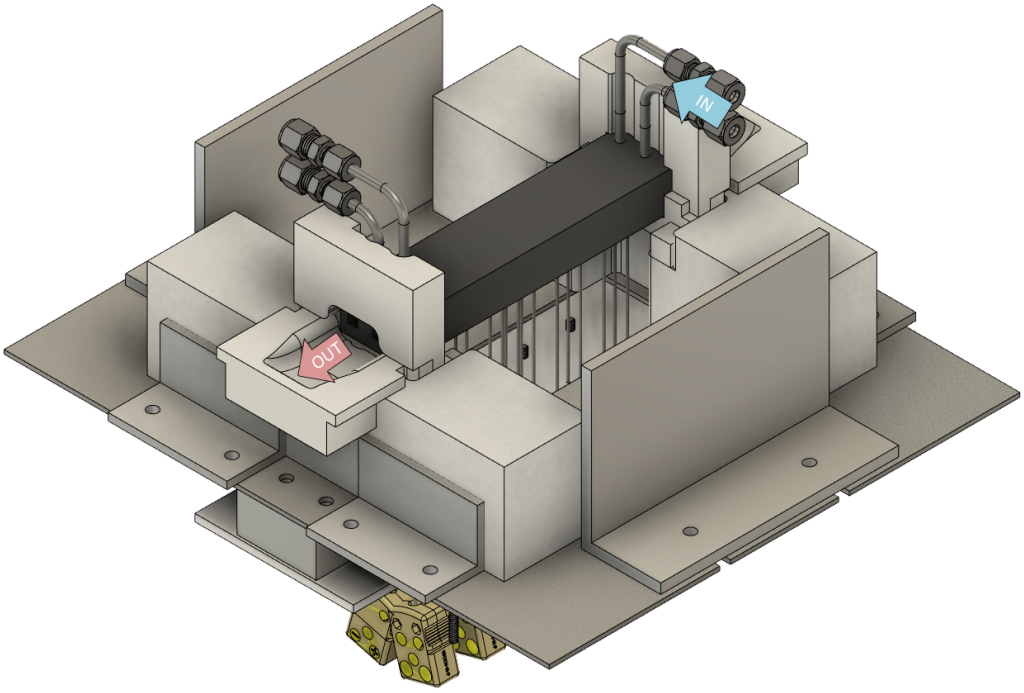

Figure 3.2: Experimental apparatus - structure overview, wrap insulation not shown

by the narrow ends. The insulation is provided by a 2-inch thick kaowool blanket wrapped around the suspended section to minimize the heat loss (not shown in Figure 3.2). A partially assembled reactor, just before the kaowool installation, is shown in Figure 3.4b. The base of the apparatus was made out of a 3/16 inch thick steel plate, on which the refractory bricks were secured by multiple L-shaped aluminum extrusions bolted in-place. Space underneath was occupied by a bank of 18 metal sheath thermocouples. They were routed through an alignment plate suspended 1 inch below the base plate. Each thermocouple was held in place by a dedicated holder arm as shown in Figure 3.3. The tip of the thermocouple went through the plate, penetrated the blanket insulation, and entered the AM core via a dedicated hole. The thermocouple remained flush with the bottom of the combustion channel to avoid disturbing the flow. Internal view of the channel with visible thermocouple ends is shown in Figure 3.4c. The differential thermal expansion between the thermocouple and AM core sealed the ingress point upon the warm-up. The position of the

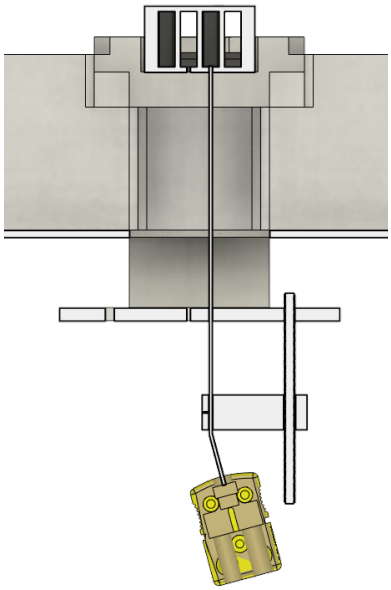

Figure 3.3: Experimental apparatus - thermocouple mount

thermocouple was fixed by a custom-machined aluminum mount suspended from the plate by a size 8 threaded rod. A small set screw within the mount enabled securing the thin thermocouple sheath in place.

The incoming mixture entered the core via a 3/16 inch stainless 316-grade steel pipe as shown in Figure 3.4. The pipes exposed length was sufficient for an infinite fin with a heated base approximation i.e. the far end of the pipe was within 10°C from the environment. It is confirmed both by a simplified CFD simulation in OpenFOAM and supplemental thermocouple measurements at both ends of the pipe. This coupled with a narrow inner diameter acted as a thermal quench flame arrestor. Furthermore, the inlet pipes were separated from the exhaust stream to avoid external preheating. The precise sizing of the inlet hole allowed a pressure fit between Si-SiC and steel pipe that is fully sealed upon warm-up due to the higher thermal expansion of steel. The receiving end of the inlet pipe was terminated by a 3/16 compression fitting that mated with the external supply system. The opposite side of the tube, entering the reactor, is purposely slotted to allow the mixture to enter and redistribute inside the Si-SiC channel. This feature best seen in Figures 3.4a and 3.4c. The flow

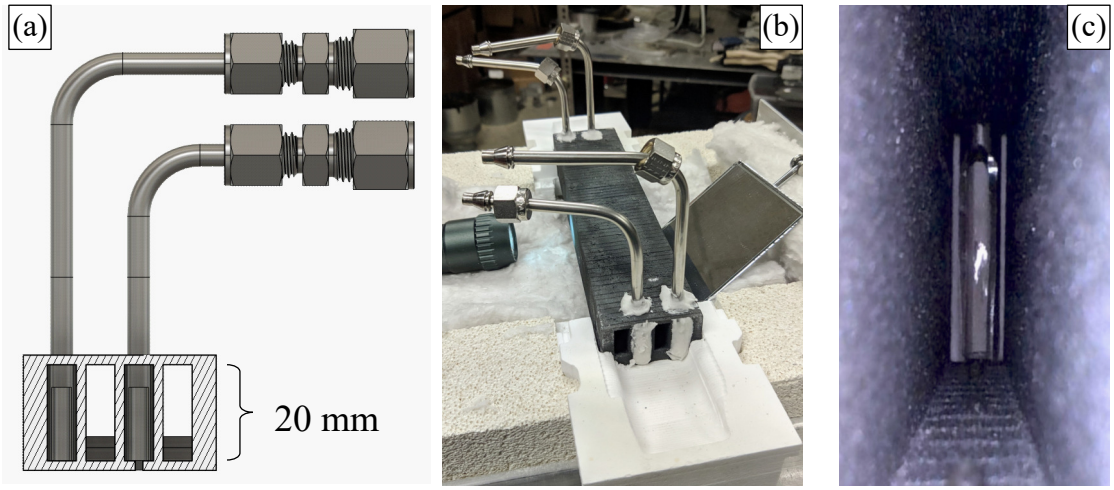

Figure 3.4: Inlet/Outlet geometry: a) cross-section view b) reactor during assembly c) internal view of the inlet pipe

straightener was omitted due to low Reynolds numbers during operation. This led to prompt dampening of induced turbulence. The entry hole and space behind the pipe (an artifact of AM process) were sealed by Resbond 940LE ceramic adhesive, as seen in the assembly photograph in Figure 3.4b. The exhaust gases exited directly into the combustion stand and were removed through an overhead ventilation hood. A carved zirconia seat, seen in Figure 3.4b, aided at redirecting the hot stream upwards. The outlets are visible in Figure 3.4b as the empty openings between the ceramic-covered counter-flow channels. There was a quartz sampling probe located at the exit of one of the channels. The samples were obtained from the exit of the inner channels unless otherwise states.

A flow delivery system, data acquisition system, and emissions analyzer were part of the complete experimental setup. The schematic of the full system is shown in Figure 3.5. The experiment was controlled via a LabView-enabled PC with a National Instruments PCI-6225 data acquisition (DAQ) card. The computer system was used to register temperature readings from all thermocouples as well as digitally control flow controllers via USB-RS232 bridges. A premixed methane-air mixture was delivered through a calibrated set of Omega FMA 2600 flow controllers (rebranded Alicat MC-series Scientific device). Air was sourced from the building utility compressed air lines available in the room. The compressed air was filtered (SPEEDAIRE 4ZL28 5μm), desiccated, and pressure regulated down to 30 psi before entering the Omega FMA-2611A 250 SLPM flow controller. Fuel was 99.97% ultra-high purity methane sourced from Praxair in 2400 psi 345 CF cylinders. The pressure was down-regulated to 25 psi and supplied to FMA-2607A 10 SLPM flow controller. All tubing and pressure regulation devices were properly sized to provide at least double the flowrate required by controllers. The supply pressures and controller PID settings were optimized to minimize downstream flow fluctuations. The flowrate reported by each

flow controllers via the RS232 interface was recorded by computer at a rate of 1Hz. Downstream of the controllers both streams were combined in a common diverging-converging mixer and equally distributed via a manifold into the four channels of the reactor. Subsequent flows in all four channels were cross-balanced via a dedicated valve-rotameter couple to ensure equal distribution, as shown in Figure 3.5. The rotameters used for this purpose were of the same model and manufacturer hence they did not require calibration. The flow delivery system allowed for control over inlet velocities between 50 cm/s and 250 cm/s with an uncertainty of ± 4 cm/s up to ± 14 cm/s, respectively. The accuracy of the mixture's Φ ranges from ± 0.055 to ± 0.02, inversely proportional to velocity. The inlet velocity range of 50 cm/s to 250 cm/s corresponds to an internal flow Reynolds number range of 100 to 1500, based on hydraulic diameter and fluid properties evaluated at temperatures between $25°C$ and $1200°C$. This indicates that the internal flow is in the laminar regime for all conditions. There was a low-flow configuration introduced during split-channel testing, where the inlet air controller was replaced by the Omega FMA6500 30 SLPM model allowing for improved accuracy at velocities below 100 cm/s. The resulting low-flow uncertainty of velocity varied from ±2 cm/s up to ±6 cm/s for the 25 cm/s to 100 cm/s range and mixture's Φ uncertainty range between 0.08 to 0.02 accordingly. The detailed uncertainty calculations are presented in Appendix A. The pressure system was regularly tested for leaks using a soapy water method.

Both equivalence ratio Φ and inlet velocity u_{inlet} influence the flame characteristics. Those can be coupled into a single Firing Rate parameter (FR), that represents the chemical energy input into the reactor. FR is defined as:

$$FR = \frac{A_{CS} \cdot u_{inlet}}{1000} \cdot \frac{\Phi}{\Phi + 9.52} \cdot \rho_{CH_4} \cdot \mathrm{LHV}_{CH_4} \quad [\mathrm{kW}] \tag{3.1}$$

where A_{CS} is the total channels cross-sectional area in cm^2, u_{inlet} is the inlet velocity in cm/s, Φ is equivalence ratio, ρ_{CH_4} is methane density at standard conditions in g/cm^3, and LHV_{CH_4} is lower heating value for methane in kJ/g. The propagated relative uncertainty for FR ranges from $\pm 4\%$ to $\pm 10\%$ of the FR value. This representation allowed examining flow and heat recirculation effects independent of the overall energy content of the reactor. Table 3.1 lists the velocity and equivalence ratio combination for each FR level. It applies for all discussed AM reactors since the effective flow area remained the same at 0.48 cm^2.

FR	$\Phi = 0.5$	$\Phi = 0.6$	$\Phi = 0.7$	$\Phi = 0.8$
0.8 kW	103 cm/s	85.6 cm/s	74.9 cm/s	66.2 cm/s
1.2 kW	146 cm/s	123 cm/s	107 cm/s	94.2 cm/s
1.6 kW	205 cm/s	173 cm/s	150 cm/s	133 cm/s
2.2 kW	275 cm/s	231 cm/s	200 cm/s	177 cm/s

Table 3.1: Constant FR line experimental conditions

The temperature was measured by a set of 18 N-type Omega SNNXL-062U-6-SHX thermocouples covered in Omegaclad XL sheath that is non-catalytic to hydrocarbon combustion. Direct measurement of gas temperature was not possible since any exposed probe would act as a flame holder and impact the overall reactor behavior. Instead, thermocouples were positioned flush with the wall inside dedicated holes, as seen in Figure 3.5. Due to the placement, each thermocouple was considered in thermal equilibrium with the wall at a given position. There were nine thermocouples per channel in each of the two counter-flowing channels in the middle of the reactor. The exact positioning of thermocouples is dependent on the AM core configuration, with details provided in the respective subsection. The instantaneous temperature measurement from all thermocouples during steady-state operation is

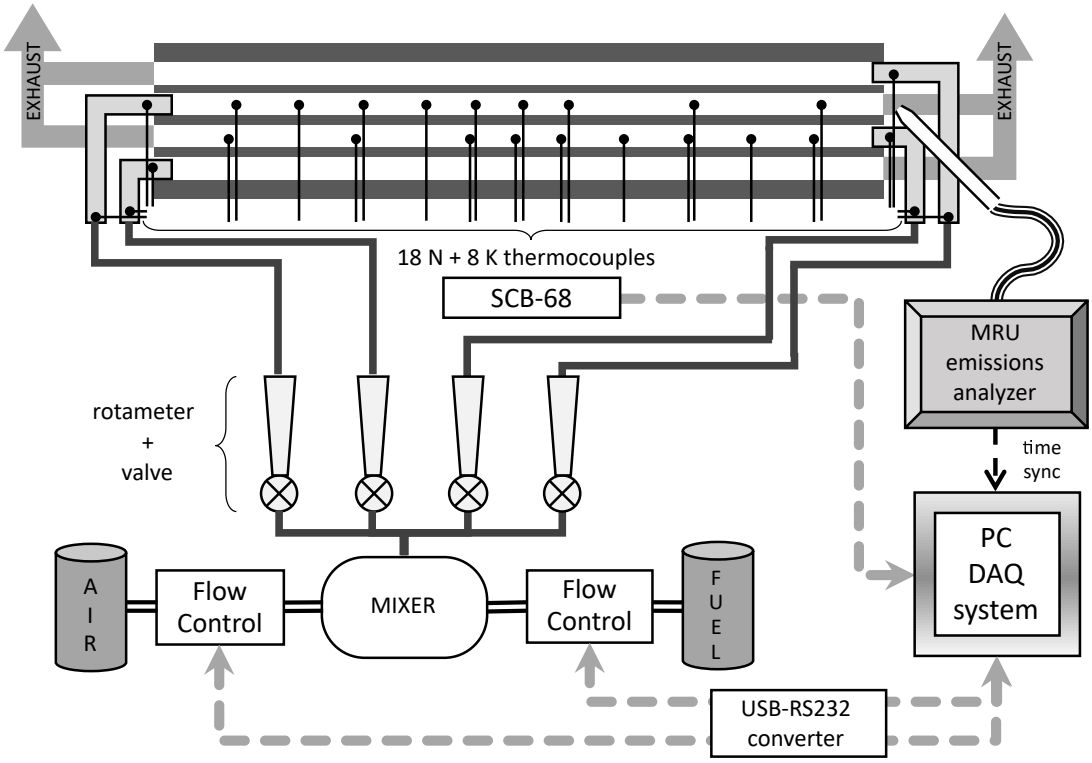

Figure 3.5: Experimental apparatus - system overview

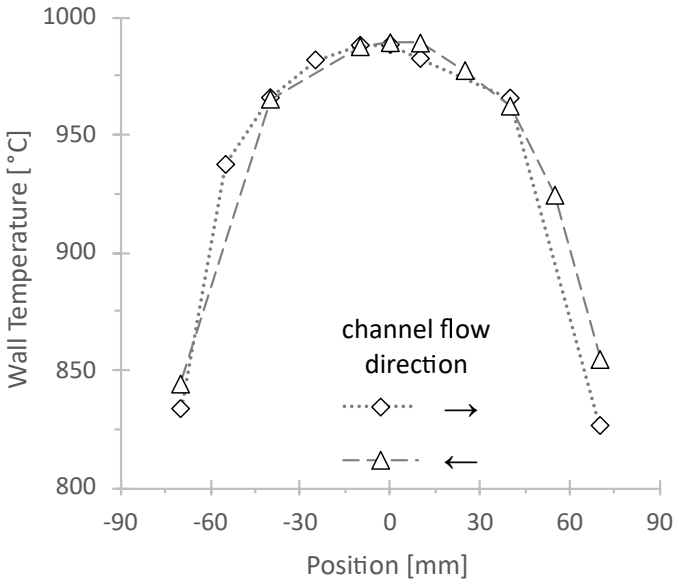

Figure 3.6: Counter-flow wall temperature profiles - complete thermocouple data in two counter-flowing channels in straight reactor at $\Phi = 0.55$ and inlet velocity 100cm/s.

shown in Figure 3.6 with diamonds indicating channel 2 (left-to-right flow) and triangles for channel 3 (right-to-left flow). The temperature profiles along both channels are symmetrical about the middle point under a nominal operation. Therefore the two-channel averaged profiles are used in the remainder of this dissertation as a single profile. Thermocouple readings were also used in the post-processing to establish the steady-state operation. It was characterized by the lack of long-term non-periodic trends with the remaining temperature variations within the uncertainty range. The steady-state time window was identified based on this criterion, and a time-averaged temperature reading was recorded. Additionally, eight K-type thermocouples attached to inlet pipes via ceramic adhesive are used to monitor the inlet conditions. Although the pipe end closer to the AM core could reach up to 760°C the far end never exceeded 35°C due to the low conductivity of stainless steel. Inlet pipe measurements were only used to monitor for safety and are not reported.

All thermocouples were connected to a DAQ system via the SCB-68 interface board in a differential configuration. SCB-68 board also provided basic signal filtering, ground loop isolation, and cold junction compensation (CJC) temperature via the on-board circuitry. The native 16-bit resolution of PCI-6225 DAQ card paired with low Seebeck coefficient of N- and K-type thermocouples resulted in poor temperature resolution (effective $\approx$ 8 °C steps). Therefore post-processing used the oversampling with dithering approach to increase the resolution to 21-bits (effective $\approx$ 0.25 °C steps) and reduce noise at a cost of lower temporal resolution (final Δt = 0.5 s). Obtained high-speed raw data was down-sampled to 21bit resolution, converted to μV, and translated to temperature using NIST ITS-90 polynomial including the CJC correction. The development work has eventually lead to improvements in a public nptdms python library in regards to the handling of mixed data types from proprietary LabView TDMS format. The DAQ card underwent a self-calibration procedure before

each experiment leading to a quantization uncertainty of ±1.5 °C (calculated per National Instruments specification). Combined with inherent thermocouples limit of error the overall temperature reading uncertainty is between ±6.75 °C and ±11.5 °C for the 700 °C to 1400 °C reading range respectively. The details on data processing and uncertainty analysis are provided in Appendix A.

When appropriate a handheld MEMS microphone was used to register sound data for fast Fourier transform (FFT) processing to identify dominant frequency peaks. The sound power magnitude was not used due to high sensitivity to a multitude of factors. Due to the nature of the frequency measurement and a very high sampling rate of modern microphone systems the measurement uncertainty was driven by the FFT frequency binning error of ±6 Hz.

The emissions of CO, NO, NO_2, and CH_4-equivalent hydrocarbons at the exit of the reactor were continuously monitored using a calibrated MRU Vario Luxx gas analyzer. The sample was obtained through a heated sampling probe with a quartz tip located near the exit of the inner channels. The sample was continuously drawn at 1 SLPM, dehumidified by a thermoelectric cooler, and analyzed by a combination of electrochemical and NDIR sensors. Emission data were recorded at 1 Hz in the internal memory of the device. In order to synchronize temperature and emissions data, an additional electrical link between MRU and DAQ was established via 4-20mA industrial interface. Consequently, the probe tip temperature was registered by both the emission analyzer and PC DAQ device and could be used to synchronize both data streams. Finally, the reported emission reading was a 5-minute average taken upon reaching a reactor's stable operation. The analyzer was frequently re-calibrated leading to the following manufacturer-stated accuracies: CO ±10 ppm or 5% of the reading, NO and NO_2 ±2 ppm or 5% of the reading, and CH_4 ±20 ppm or 2% of the reading. The reported NO_x value carries a propagated error from NO and NO_2

measurements, details in Appendix A.

The secondary use of the gas analyzer was a leak detection of AM core. A stream of pure CH_4 gas was flown through one channel at a time. The quartz probe was used to check thermocouple holes and the inlet steel pipe ingress points. To positively pass a leak test, all registered CH_4 signals had to remain within ± 20 ppm measurement uncertainty. In the process of methane leak testing, a mild permeability of the thin wall separating adjacent channels was detected. When the outlet of a dormant channel adjacent to one under test was sampled a small amount of CH_4 (up to 350 ppm) was registered. Due to a counter-flow configuration and no detectable leaks at the pipe inlet itself, the main suspect is a residual porosity of the Si-SiC cermet. This behavior further extends to a normal operation, where trace amounts of CH_4 ($\approx$30 ppm $\pm$20 ppm) were detected at the channel outlet among combustion products. The overall magnitude of observed intra-channel mass flux was minuscule compared to a nominal inter-channel mass flow.

The efficient heat recirculation necessary for nominal operation is absent in a cold reactor. Furthermore, the high thermal mass of the walls made it more challenging to establish a flame inside the channel. Both factors negatively impacted the ability of start the reactor from cold. Straight and diverging reactors were able to immediately sustain the flame internally for mixture's Φ above 0.8 and low flow velocity of 40 cm/s. Initially, during the warmup phase, the flame resided at the inlet pipe providing sustained heating of the overall structure. High thermal conductivity and low thermal expansion make the Si-SiC a suitable material to withstand the temperature difference experienced during the startup process without cracking. As the wall temperature approached the operational values, over 700°C, the flow conditions were gradually adjusted towards the target value. In contrast, the split-channel design was unable to sustain an internal flame when cold. The ignited mixture quenched

at the narrowest part of the channel. A special procedure was adopted where the outermost channels were purposely set under a blow-off condition. This acted as a continuous ignition source for inner channels that remained at the nominal flow rate. This resulted in a periodic ignition-quench action with the period in the range of 1 to 10 seconds. Eventually, the reactor wall heated sufficiently to allow a successful propagation of the flame, a condition shown in Figure 3.7. Subsequently, the velocity of the outer channels was lowered until all four were flow-balanced and holding the flame internally. The remainder of the startup was analogous to the procedure for the straight and diverging channel reactors as discussed before. The overall startup sequence took between 15 and 30 minutes with a straight channel nearing the lower end of this range. Additional 30-60 minutes were required to reach a steady-state operation, depending on the targeted conditions. This is significantly slower than the original handmade reactor, which can be accounted for by a higher thermal mass of the AM device.

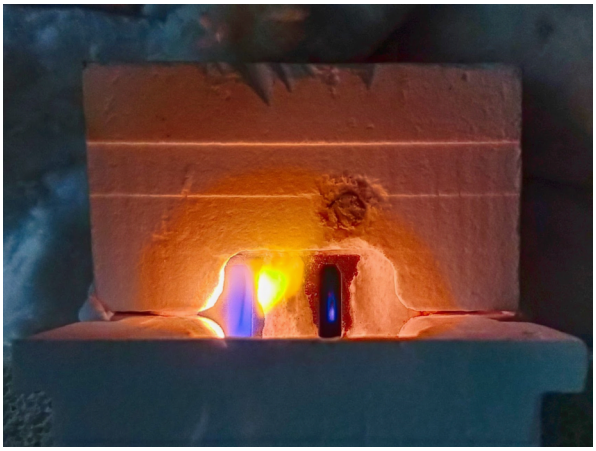

Figure 3.7: Split-channel reactor warmup procedure: outer channel under blow-off, inner channel stabilized internally

The shutdown procedure started by bringing the combustor to low power mode and allowing it to cool while maintaining the flame. Once a near steady-state opera-

tion is achieved (usually within 10 minutes) the fuel was disabled while maintaining the airflow. As the temperature of the reactor drops the airflow rate is increased to maintain a consistent cooling rate until the temperature falls below 100°C. At this point the air was disabled and the reactor continued to cool via natural convection.

3.1.2 Flame Exposure Apparatus

The flame exposure test of Si-SiC material was performed in a ceramic combustor built by Smith et al. [83]. This burner was originally used to analyze burner-stabilized methane flames. The construction was based on a design similar to a McKenna burner and produced a stable flame with a substantial standoff distance above the ceramic medium. The system diagram is shown in Figure 3.8. The internal diameter of the quartz tube was 2 in with a total height above the ceramic matrix of 6 in. An additional 1 in thick alumina insulation around the quartz shield was installed to reduce heat loss. The Si-SiC samples were suspended on a Nichrome wire such that the flame impinged at its bottom surface. The methane and air streams were mixed in a diverging-converging mixer followed by a porous media and alumina pellets situated in the burner itself. Air was sourced from the compressed air line and controlled by a Teledyne HFC-203 110 SLPM flow controller. The 99.9% pure methane was delivered from the Airgas 320 cf 2400 psi cylinder via a Teledyne HFC-202 10 SLPM flow controller. Both controllers were operated by Hastings model 400 power supply and the measured flow rate was recorded by PC equipped with the National Instruments PCI-6024E DAQ card. The flow delivery system allowed for control over inlet velocities between 20 cm/s and 100 cm/s with an uncertainty of $\pm$ 1 cm/s up to $\pm$ 3.5 cm/s, respectively. The accuracy of the mixture's Φ ranged from $\pm$ 0.02 to $\pm$ 0.1, inversely proportional to velocity. The temperature at the middle of sample height ($\approx$ 0.5 cm above flame) was measured by a single K-type thermocouple connected to National

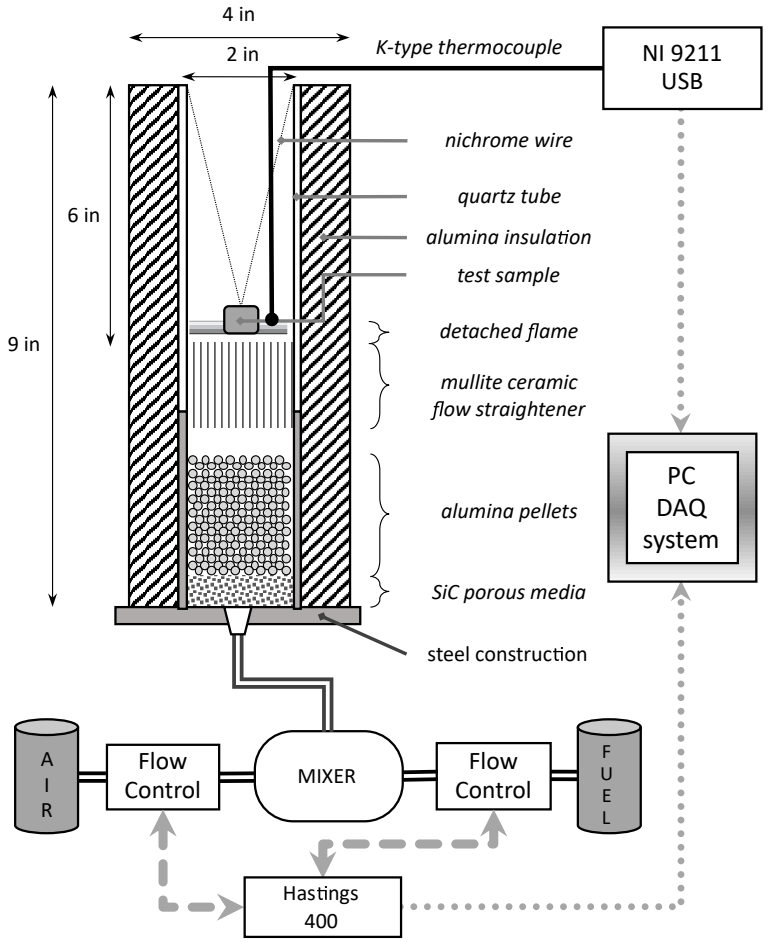

Figure 3.8: Flame exposure apparatus - system overview

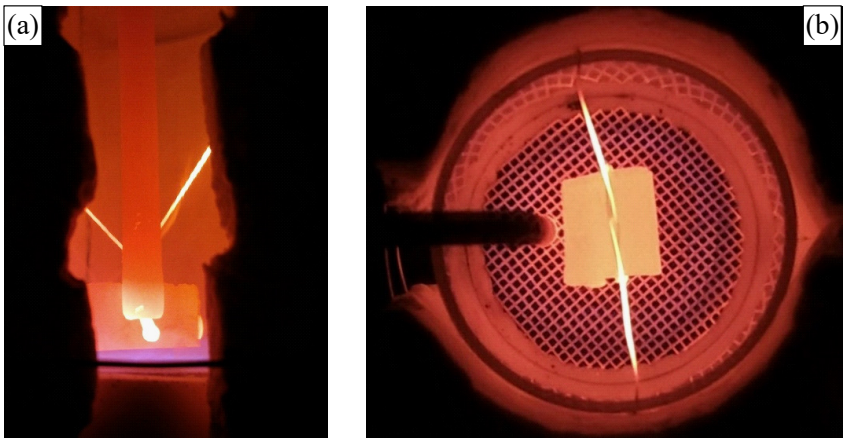

Figure 3.9: Picture of material sample during the exposure test: a) side view b) top view

Instruments 9211 temperature input USB module with a built-in amplifier and CJC compensation. The temperature resolution was 0.05°C at the 2Hz acquisition rate and a maximum measurement error of ±1.6°C.

The experiment was designed for a long-term exposure of the suspended material in a combustion environment. The main goal was to maintain a stable temperature and flame position near the sample for a prolonged time. The apparatus was started with a sample at a specified height. A near-stoichiometric mixture was introduced to the system and ignited. Upon ignition the flame was arrested at the surface of the ceramic flow straightener by the high thermal mass, a transient state eventually leading to a flashback. The flow was adjusted to achieve a stable, detached flame that can be sustained for a long time without damage to the combustor itself. Once detached the steady-state was achieved in a short time due to a small thermal mass in the immediate flame vicinity. The flow conditions were actively adjusted to maintain the desired temperature at the measurement point. At the end of the experiment, both air and fuel streams are stopped at the same time allowing the sample to cool via natural convection.

There were two combustion environments studied as presented in Table 3.2. The low temperature, low Φ had a higher partial pressure of oxygen P_{O_2} in combustion products representative for practical flames. Meanwhile, the high-temperature test aimed at higher thermal stress at lower oxygen content. The experiment was performed in 5-hour increments for a total of 10 hours. After each exposure, the sample was weighed and photographed. Upon completion, an SEM surface imagining was performed, complemented by the EDS analysis of its atomic composition.

Test name	**Temperature range [°C]**	**Equivalence ratio Φ**	**Flow velocity [cm/s]**	**P_{O_2} products [atm]**
1000°C	990 - 1010	0.69	26	0.0607
1260°C	1250 - 1270	0.9	74.5	0.0192

Table 3.2: Material combustion test environments

3.2 Analytical Model

3.2.1 Mathematical Model

A one-dimensional analytical model for heat recirculating reactors operating under rich conditions was developed by Schoegl and Ellzey [6]. This model was recalibrated to represent lean combustion conditions and used to analyze the performance of experimental reactors. Following is a simplified description of the analytical model with the full derivation available in Schoegl's dissertation [84]. Notably the approach has been further developed in the following years [85, 86], however this work is adapted from the original formulation. The geometry is represented by two adjacent counter-flow channels coupled by a conductive wall. The model domain for counter-flow configuration together with variables of interest are shown in Figure 3.10. Arrows indicate position of the inlets and general flow direction through the channel. The flame is indicated by thick vertical triple lines and marked by positions $x_{c,1}$ for upper channel, and $x_{c,2}$ for the lower channel. An extensive summary of model parameters is presented in Table 3.3.

Combustion is approximated via a one-step model with all thermophysical properties assumed constant and evaluated at 1000°C. Radiative heat exchange is neglected except for radiative heat loss from the solid ends of the reactor. Operating

Accent		Properties	
$'$	Dimensional value	$L^{'}$	Reactor length
$_{ref}$	Reference value	a	Channel width $\equiv \frac{2a^{'}}{L^{'}}$
$_{g}$	Gas property	b	Wall thickness $\equiv \frac{2b^{'}}{L^{'}}$
$_{w}$	Wall property	x	Axial position $\equiv \frac{2x^{'}}{L^{'}}$
$_{i}$	Channel indicator	T	Temperature $\equiv \frac{T^{'}}{T^{'}_{ref}}$
$_{c}$	Combustion location	u	Velocity ratio $\equiv \frac{u^{'}}{u^{'}_{ref}}$
$_{0}$	Inlet condition	k	Relative thermal conductivity $\equiv \frac{k^{'}_{g}}{k^{'}_{w}}$
$_{\infty}$	Environment	$h^{'}$	Convective heat transfer coefficient
$_{ad}$	Adiabatic flame prediction	$\alpha^{'}$	Thermal diffusivity
		ε	Solid emissivity
		$\sigma^{'}_{B}$	Stefan-Boltzmann constant

Common Dimensionless		Model parameters	
Le	Lewis number	β	Modified Zeldovich number $\equiv Ze\frac{T^{'}_{ref}}{\Delta T^{'}_{ad}}$
Nu	Nusselt number	ϵ	Geometry factor $\equiv \frac{a}{Pe} = \frac{2\alpha^{'}_{g}}{L^{'}u^{'}_{ref}}$
Pe	Peclet number	κ	Conductivity factor $\equiv \frac{b}{2ak} = \frac{b^{'}}{2a^{'}}\frac{k^{'}_{w}}{k^{'}_{g}}$
Re	Reynolds number	μ	Heat transfer factor $\equiv \frac{Nu}{Pe^{2}} = \frac{h^{'}}{u^{'}_{ref}}\frac{\alpha^{'}}{k^{'}_{g}}$
Ze	Zeldovich number	χ	Heat loss factor $\equiv \frac{Nu_{\infty}}{2\cdot Nu} = \frac{h^{'}_{\infty}}{2h^{'}}$
Φ	Equivalence ratio	σ	Radiation factor $\equiv \frac{1}{2}\,\varepsilon\,\sigma^{'}_{B}\,\frac{L^{'}}{k^{'}_{w}}\,T^{'3}_{ref}$

Table 3.3: Common Variables

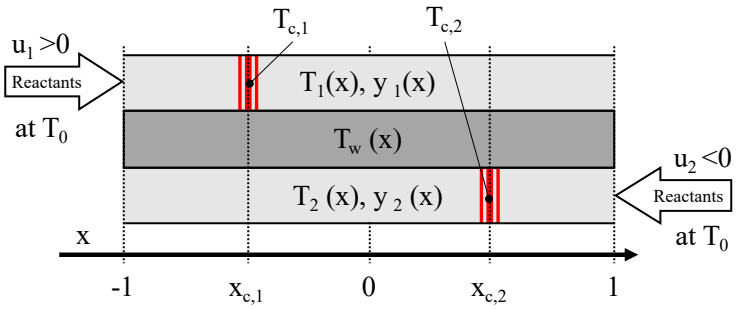

Figure 3.10: Graphical representation of the solution domain for counter-flow configuration

conditions are a function of equivalence ratio Φ, inlet temperature T_0, and temperature of surroundings T_∞. The large activation energy asymptotic assumption [87] links the inlet flow velocity u_{inlet} with the peak temperature at the predicted flame position. The normalized conservation of energy for the counter-flow reactor operating at steady state with the above assumptions, including conductive and convective heat transfers, mass transfer, external heat losses, and chemical reaction for the gas (T_i) and wall (T_w) temperatures are

$$\frac{d^2T_i}{dx^2} = \pm\frac{u_i}{\epsilon}\frac{dT_i}{dx} + \frac{\mu}{\epsilon^2}(T_i - T_w) + \frac{(T_{ad} - T_\infty)}{\epsilon^2}w_i \tag{3.2}$$

$$\frac{d^2T_w}{dx^2} = \frac{\mu}{\kappa\epsilon^2}\left[(1+\chi)T_w - \frac{1}{2}(T_1 + T_2) - \chi T_\infty\right] \tag{3.3}$$

with w_i reaction term approximated as a point source via Dirac delta function δ due to activation energy asymptotic [87]:

$$w_i(x) \approx \epsilon\,\delta(x - x_{c,i})\exp\left(\frac{\beta\cdot[T_i(x) - T_{ad}(\Phi)]}{2\cdot T_i(x)/T_{ad}(\Phi)}\right) \tag{3.4}$$

where T_{ad} is a normalized adiabatic flame temperature as a function of Φ. This approach necessitates the subdivision of the analytical domain into three sections: $x = -1$ to $x_{c,1}$, $x_{c,1}$ to $x_{c,2}$, and $x_{c,2}$ to $x = 1$. The inlet is defined by Neumann

boundary condition:

$$\frac{dT_i}{dx} = \frac{u_i}{\epsilon}(T_i - T_0) \tag{3.5}$$

$$\frac{dy_i}{dx} = \frac{u_i Le}{\epsilon}(y_i - y_0) \tag{3.6}$$

with the outlet:

$$\frac{dT_i}{dx} = 0 \tag{3.7}$$

$$y_i = \frac{dy_i}{dx} = 0 \tag{3.8}$$

Additionally the ends of a solid wall ($x = -1$ and $x = 1$) are assumed to experience a radiative heat loss to the environment:

$$\frac{dT_w}{dx} = \pm\sigma\left(T_w^4 - T_\infty^4\right) \tag{3.9}$$

The internal boundary conditions in absence of flame are provided by continuity:

$$[T_w]_-^+ = \left[\frac{dT_w}{dx}\right]_-^+ = 0 \tag{3.10}$$

$$[T_i]_-^+ = \left[\frac{dT_i}{dx}\right]_-^+ = 0 \tag{3.11}$$

$$[y_i]_-^+ = \left[\frac{dy_i}{dx}\right]_-^+ = 0 \tag{3.12}$$

where $[\,]_-^+$ denotes no change in function value on both ends of the internal boundary. The influence of flame is incorporated by the internal boundary condition that represents the chemical reaction energy source:

$$[T_i]_-^+ = 0 \quad \text{and} \quad \left[\frac{dT_i}{dx}\right]_-^+ = \frac{1}{\epsilon}\frac{T'_{ref}}{\Delta T'_{ad}}\exp\left(\frac{\beta \cdot [T_i(x) - T_{ad}(\Phi)]}{2 \cdot T_i(x)/T_{ad}(\Phi)}\right) \tag{3.13}$$

$$[y_i]_-^+ = 0 \quad \text{and} \quad \left[\frac{dy_i}{dx}\right]_-^+ = -\frac{Le}{\epsilon}\exp\left(\frac{\beta\cdot[T_i(x)-T_{ad}(\Phi)]}{2\cdot T_i(x)/T_{ad}(\Phi)}\right) \tag{3.14}$$

The model is completed with a limiting species conservation equation involving transport, diffusion, and reactions rate:

$$\frac{1}{Le}\frac{d^2y_i}{dx^2} = \pm\frac{u_i}{\epsilon}\frac{dy_i}{dx} - \frac{1}{\epsilon^2}w_i \tag{3.15}$$

This coupled with a large energy activation asymptotic approximation yields the coupling between inlet velocity and combustion peak temperature $\mathrm{T}_{c,i}$:

$$|u_{i,\text{coupled}}| = \exp\left(\frac{\beta\cdot[T_{c,i}-T_{ad}(\Phi)]}{2\cdot T_{c,i}/T_{ad}(\Phi)}\right) \tag{3.16}$$

The above formulation is iteratively solved for a refined x_c guess until the calculated $u_{i,\text{coupled}}$ matches the prescribed inlet velocity. Conceptually this analytical approach is equivalent to the actual stability condition, where the effective flame speed equals the burning velocity of a mixture. If the real solution cannot be found or the solution x_c is outside the $-1 < x_c < 1$ range that means flame would not stabilize within reactor. The velocity versus position stable range can be plotted by repeating the solution process for a range of inlet velocities.

Equation 3.16 was also used for calibration of T_{ad} and β terms for lean methane-air combustion based on a detailed Cantera 2.4 [14] freeflame simulation with UCSD chemical mechanism [88]. The calibration data at each Φ is selected such that the inlet velocity at standard conditions (298K, 1 atm) is equal to the reference velocity. The fundamental nonlinearity of combustion processes limits the accuracy of this approach to inlet velocities moderately close to the reference value. The calibration for selected $\Phi_{ref} = 0.65$ ($\mathrm{T}_{ref} = 2130.7$ K, $\mathrm{u}_{ref} = 54.31$ cm/s) are presented in Table 3.4.

Φ	0.45	0.5	0.55	0.6	0.65	0.7	0.75	0.8
T'_{ad} [K]	1984	2022	2059	2095	2131	2166	2202	2238
$\frac{T'_{ref}}{\Delta T'_{ad}}$	0.45	0.50	0.54	0.58	0.62	0.67	0.70	0.74
β	15.69	14.75	14.08	13.53	13.22	13.11	13.23	13.59

Table 3.4: Analytical model combustion calibration details

3.2.2 Results and Discussion

The predicted performance of counter-flow reactors under lean combustion was analyzed using a representative set of thermal and flow parameters approximating the physical reactors. The following study looks at differences in the stability range as each of major parameters is changed independently. A set of model parameters representative for an experimental device is used as a base case for the following discussion. The values are provided in Table 3.5. The significant simplifications of the analytical model limit its applicability to only qualitative predictions of the reactor behavior. The model is capable of representing the stabilization mechanism and was used in inspecting the system response to changes in the operating conditions and reactor parameters.

Geometry factor	ϵ	0.0046
Conductivity factor	κ	95.24
Heat transfer factor	μ	0.035
Wall heat loss factor	χ	0.0092
Radiative solid heat loss	σ	0.9873

Table 3.5: Reactor parameters used in analytical model as a base case

Figures 3.11a and 3.11b illustrate the respective impact of equivalence ratio and inlet temperature on predicted reactor performance. Model solutions are shown as

the locus of points combining predicted non-dimensional flame location and reduced inlet flow velocity u/u_{ref}. At each location, two velocities are identified. As explained in [6], only the upper left region, where $\frac{du}{dx}$ is positive, represent stable flame locations within the reactor channels.

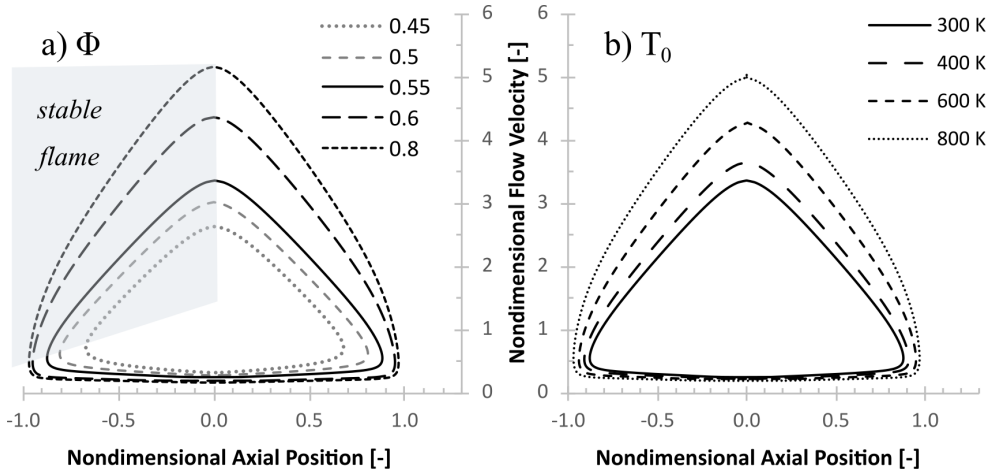

Figure 3.11: Analytical Model: Impact of operating parameters on combustion characteristics: a) equivalence ratio Φ b) inlet temperature T_0 at Φ = 0.55.

At a fixed equivalence ratio the flame stabilizes nearer the reactor's centerline ($x = 0$) as inlet velocity is increased. Stabilization nearer the center allows a greater heat recirculation hence higher effective flame speed to balance the incoming flow. As the equivalence ratio approaches the lower flammability limit for methane (Φ = 0.5) the stable velocity range becomes significantly narrower, although operation below the limit remains possible at low velocities. Increasing Φ, from 0.55 to 0.6 and higher, the maximum velocity also increases. This indicates the necessity of a higher inlet flow rate to balance the increased effective flame speed. Similar behavior can be observed for higher inlet temperatures at a fixed Φ = 0.55 as shown in Figure 3.11b. Increasing the inlet temperature T_0 results in a higher inlet velocity in order to balance the increased effective flame speed , but also extends the velocity range. A higher inlet temperature means that less heat recirculation is necessary and flames

tend to stabilize further upstream at the same inlet velocity.

In Figure 3.12, the influence of reactor-specific parameters is shown at constant $\Phi = 0.55$ and $T_0 = 300$ K. The parameter change is implemented as a multiplication of the base case values, listed in Table 3.5. The base value result is depicted by the solid black line. The geometry factor ϵ, Figure 3.12a, is inversely proportional to the gas channel length. Longer channels, hence smaller ϵ values, are capable of sustaining higher inlet flow velocities. Meanwhile, channels substantially shorter than the studied reactors, higher ϵ values, tend to have stable flame positions only near the midpoint of the device. The observed importance of ϵ is tied to the availability of heat exchange surface, which increases with the longer channels.

The axial thermal conductivity, Figure 3.12b for κ, shows very little effect on the stable range in the counter-flow configuration. In contrast, the gas/solid convective heat exchange factor μ, Figure 3.12c, has a very strong impact on combustion behavior. Lowered convection, low μ, implies less heat recirculation, which leads to stabilization closer to the middle of the reactor at fixed inlet velocity. Respectively the increase of the convective heat exchange expands the allowable inlet velocity range. It should be noted that it also increases the the minimum velocity, which might be detrimental to low firing rate operation. Finally, the heat losses χ, Figure 3.12d, have an expected impact by reducing the stable range as χ increases. This corresponds with previous analytical findings by Takeno and Hosi [89, 90], who found a similar correlation for participating porous media combustors. The same work predicts an increase in velocity range at longer channels, lower ϵ values, as seen in Figure 3.12a.

The analytical model was also used to augment the experimental temperature measurements with an estimate of the gas temperature. As discussed in Section 3.1 a direct reading of gas temperature was impossible without interrupting the flow pattern, hence only the wall temperature was collected. The model parameters shown

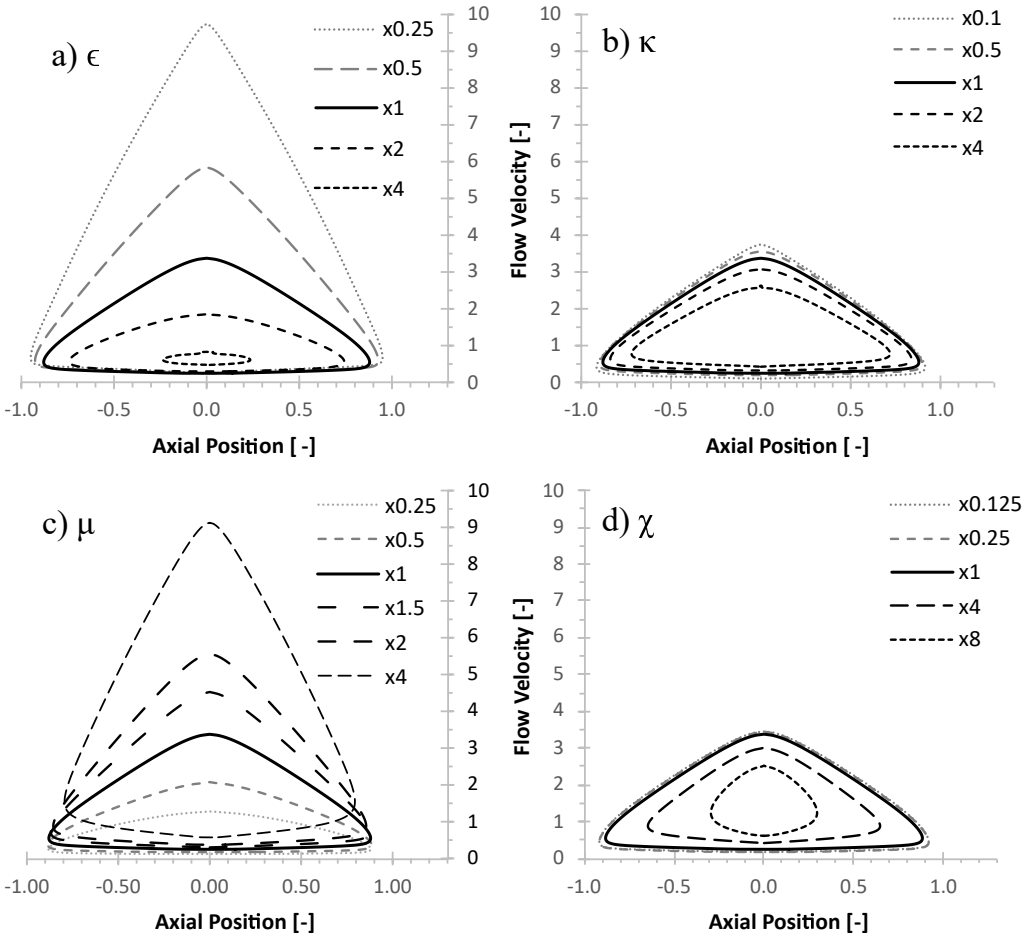

Figure 3.12: Analytical Model: Impact of multiplying base case reactor parameters on combustion characteristics at $\Phi = 0.55$: a) geometry factor ϵ b) conductivity factor κ c) convective heat transfer factor μ d) heat loss factor χ.

in Table 3.5 were fine-tuned to best-fit the wall temperature data of straight reactor at $\Phi = 0.55$ mixture and velocities between 75 cm/s and 225 cm/s. Velocities outside this bound resulted in no solution due to a lack of convergence of the analytical model, which corresponds with observed stability limits, Figure 3.15. The wall-gas heat exchange coefficient was representative of an internal flow while the external loss coefficient was typical for natural convection. The preheating of the reactants via the inlet tube was approximated using the inlet thermocouple measurement coupled with

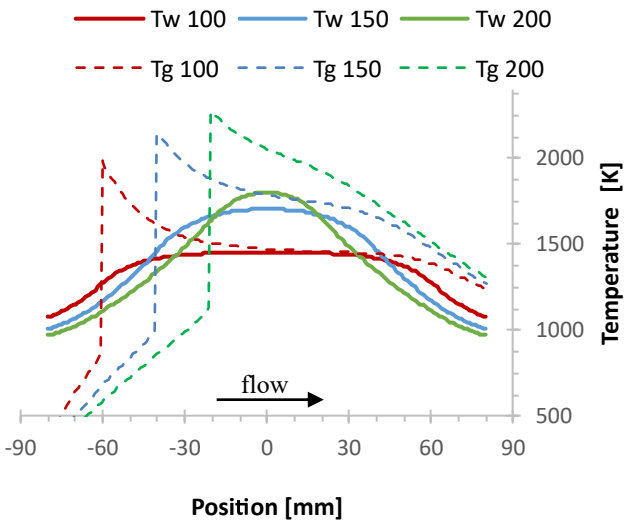

Figure 3.13: Analytical model wall (T_w) and gas (T_g) temperatures at $\Phi = 0.55$ for a range of inlet velocities.

a simplistic OpenFOAM conjugate flow and heat transfer numerical simulation. The range of T_0 spanned from 142°C to 300°C depending on the inlet velocity, where slower flow resulted in a higher preheat. Figure 3.13 shows the predicted wall temperatures, solid lines, together with predicted gas temperatures depicted by dashed lines. Distinct gas temperature peaks indicate the expected flame position. Furthermore all predicted temperature peaks substantially exceeded the adiabatic flame temperature of methane/air mixture at Φ=0.55 of 1302°C, supporting a superadiabatic nature of studied reactor. The cross-comparison provided a guidance on how the wall temperature may be interpreted with respect to the flame location. Higher inlet velocities result in flames stabilized nearer the mid-line of the reactor with a distinct peak in wall temperature. Meanwhile, low inlet velocity flames stabilized near the inlet produced wider and flatter profiles.

3.3 Straight Channel Reactor

The straight channel reactor was chronologically the second examined flow configuration. The design was analogous to the handcrafted reactor by Schoegl [6] and Belmont [42]. It was a reference case in comparison with more complex geometries presented in later sections.

3.3.1 Design

The straight design was made of constant cross-section channels that extended through the length of the reactor. The top-down cross-section view of the actual CAD model is shown in Figure 3.14 with might highlighted major features and arrows indicating the flow direction. Additionally, a side cut, including inlet pipes, is presented in Figure 3.4a. Each channel has width has rectangular cross-section of 6 mm wide and 20 mm tall. The wall separating channels is 2 mm thick. The single-channel cross-sectional area is 0.12 cm^2 for a total flow area of 0.48 cm^2 for the whole reactor. Although the AM capacity would allow directly reproducing the handcrafted reactor (4 x 20 x 1 mm respectively), a more conservative dimensions were incorporated for a greater flexibility with more complex designs. The thermocouple positions are indicated by round holes in two inner channels shown in Figure 3.14. The unequal thermocouple spacing is intended to provide an improved measurement coverage in the area of interest.

3.3.2 Operating Range

The operating range of the reactor in the form of stability map is presented in Figure 3.15. Each point in the inlet velocity - Φ space indicates a single test point. The Φ ratio spans from slightly beyond the lean flammability limit, $\Phi < 0.5$, up to Φ

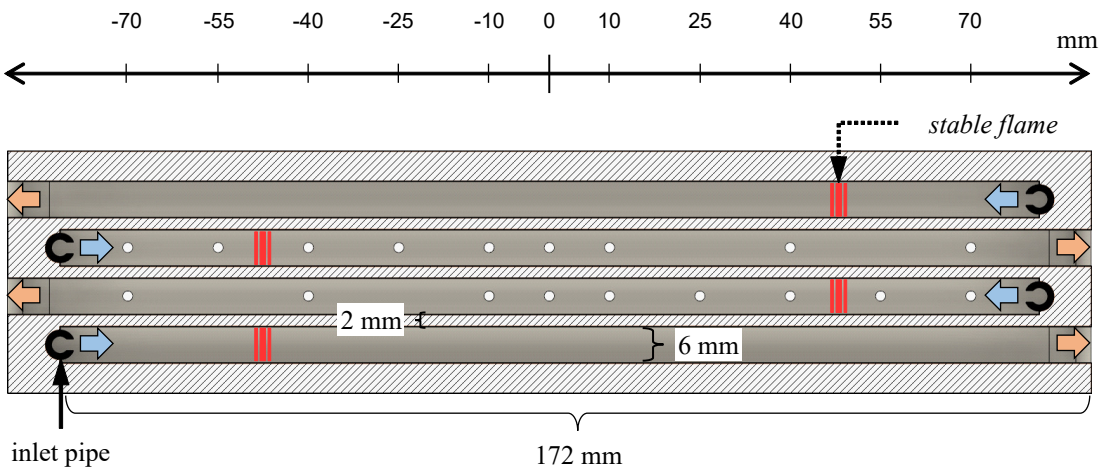

Figure 3.14: Straight Geometry: reactor sketch - top view

= 0.8. There are two main types of observed instabilities: flashback and blow-off. Flashback usually occured with mixtures closer to stoichiometric, when the effective flame speed exceeded the flow velocity allowing the flame to enter the supply line. In the case of AM reactors, the flame propagated upstream and stabilized at the inlet pipe due to a significantly smaller cross-sectional area of the pipe opening. This condition was identified as an arrested operation to differentiate from the actual flashback. Although the reactor could operate in a stable manner under the arrested mode, the heat recirculation was not properly developed and therefore it was not the optimal operating condition. Blow-off is the opposite situation, where high inlet velocity pushed the flame position past the lengthwise middle point of the channel. This made the overall system inherently unstable. Subsequently, the flame rapidly propagated further downstream and exited through the combustor outlet. Blow-off was identified when the temperature in either channel started to rapidly drop due to the loss of the flame. Furthermore, the reactor's straight layout and unobstructed outlet made it possible to visually confirm the absence of flame in the channel. In previous experiments [40, 42] an extinction was observed at the lowest velocity, when

the combustion energy release was insufficient to sustain temperatures high enough to continue chemical reactions. This was not identified in the straight AM reactor, instead, being replaced by an inlet-arrested operation. The major difference from the original handmade design is a lack of porous media flow straighteners at the inlet which reduced the heat losses experienced by flame arrested at the entry location.

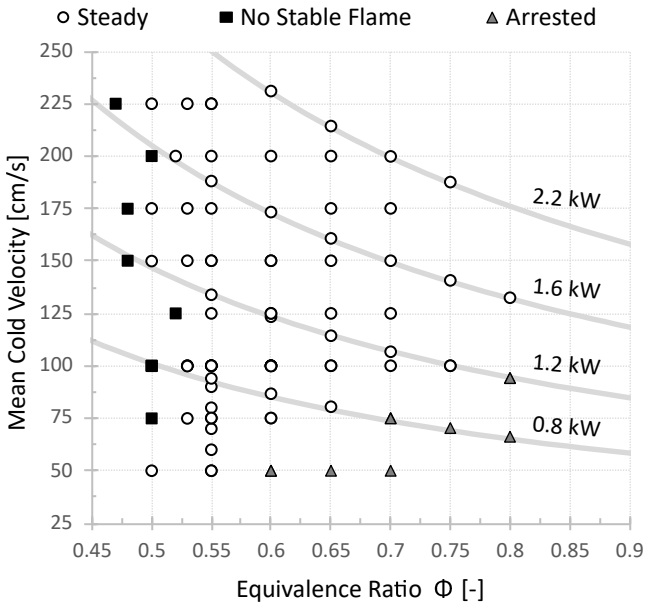

Figure 3.15: Straight Geometry: stability map in the range of Φ and inlet speeds. Solid lines represent constant FR.

Experimental data shown in Figure 3.15 indicate a wide operating range from $\Phi = 0.5$ up to $\Phi = 0.8$ and higher, with a minimum stable velocity of 75 cm/s. The reactor reached a maximum allowed material temperature of $1350°C$ before an upper velocity bound could be identified. Any further increase of temperature carried the risk of melting the silicon metal ($1414°C$) constituent of Si-SiC cermet. The lowest Φ limit was defined by flame blow-off occurring at approximately $\Phi = 0.5$. The AM reactor operated effectively at $\Phi = 0.55$ over a wide range of velocities with even leaner operation possible at higher velocities. All observed velocities at this Φ are significantly higher than the laminar flame velocity of 6.9 cm/s [91] for methane at Φ

= 0.55. Notably, the minimum velocity required to avoid inlet-arrested operation was at least 75 cm/s, which is 11 times higher than the laminar flame speed at respective Φ. The lower velocity bound increased with a higher Φ eventually reaching 94 cm/s for Φ = 0.8, approximately 2.6 times the laminar flame velocity at that equivalence ratio. This is consistent with the analytical model, Figure 3.11, that predicted that an increase of Φ at constant velocity shifts the stable position closer to reactor ends making it more likely to flashback.

3.3.3 Wall Temperatures

Figure 3.16 shows experimental measurements of wall temperature for a range of inlet velocities and a fixed Φ = 0.55. Consistent with the analytical model results discussed in Section 3.2.2, at higher inlet velocities the temperature profile became more peaked, indicating that the flames were stabilizing near the mid-line of the reactor. A detailed look at two velocities for a range of equivalence ratios is shown in Figure 3.17. The increased flow rate at a higher velocity, 200 cm/s, required more heating to reach the temperature required to initiate chemical reactions. Thus, the flame stabilized further away from the inlet. The efficiency of heat recirculation became a limiting factor at the leaner Φ = 0.5 case, where the flame resided near the midpoint of channel length. Due to the inherent stability criteria of counter-flow design a stable operation was not possible with flame residing past the middle point of the channel length. Therefore the Φ = 0.5 case with 200 cm/s inlet velocity is an example of operation near the blow-off limit. In contrast, all cases at the lower inlet velocities presented in Figure 3.17, solid lines, showed nearly flat temperature profile at any value of Φ. The lower volumetric flow rate, leading to reduced energy input, caused the wall conduction and external heat loss to become a substantial parts of the reactors' energy balance. This, in turn, resulted in the observed flattening of wall temperature profiles. Furthermore,

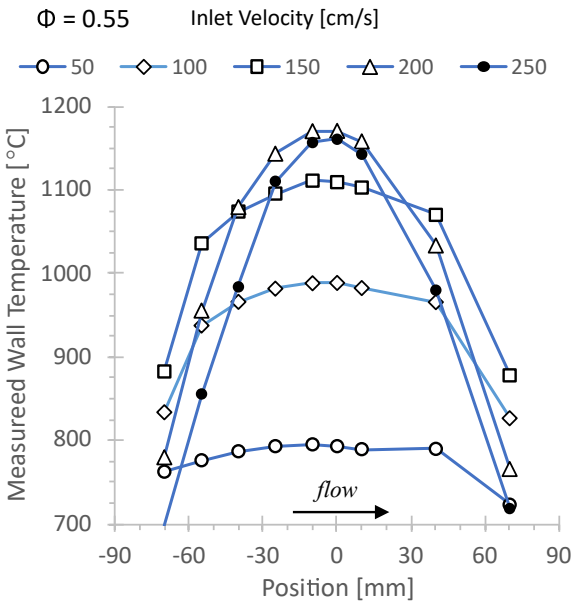

Figure 3.16: Straight Geometry: impact of inlet velocity on measured wall temperature profiles at fixed $\Phi = 0.55$.

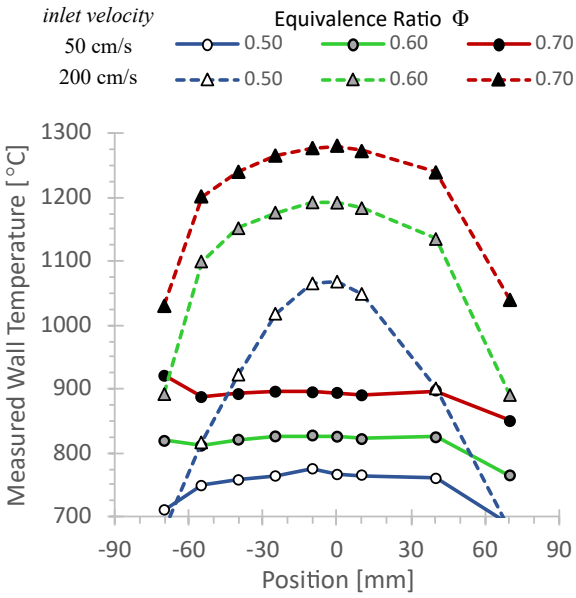

Figure 3.17: Straight Geometry: impact of Φ on measured wall temperature profiles for two inlet velocities.

the low inlet velocity facilitated flame stabilization far upstream, near the inlet. At the limit, when the effective flame velocity exceeded the inlet flow velocity in the main channel, the reaction front was stabilized at the narrower inlet pipe, an arrested condition. This was identified when the wall temperature at the thermocouple closest to the inlet was within $25°C$ (or hotter) than the middle of the reactor. All but the leanest cases associated with the velocity of 50 cm/s in Figure 3.17 showed the arrested operation. The effective laminar flame speed increase associated with richer mixtures ($\Phi = 0.6, 0.7$) was expressed in a significant increase of the inlet temperature thus exceeding the flashback/arrested criterion. The lowest $\Phi = 0.5$ case resulted in the slowest effective flame speed allowing for a flame stabilization within the main channel. Hence the dome shape developed that met the criteria to be classified as a stable point.

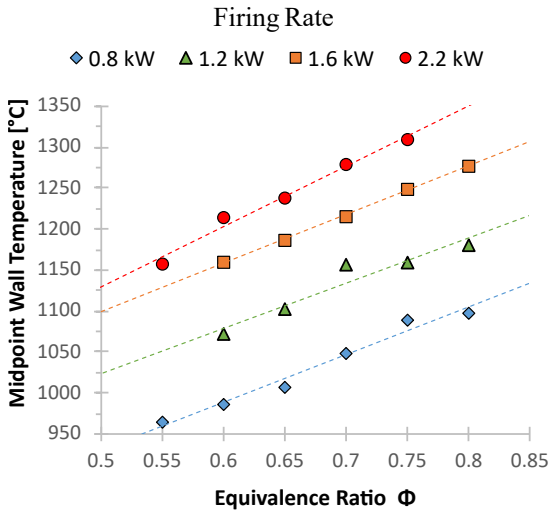

Figure 3.18: Straight Geometry: experimental averaged midpoint wall temperature vs velocity plot for a range of Φ

Presenting the data in terms of constant FR, equation 3.1, allowed the inspection of the flame behavior related only to the heat recirculation and flow characteristics as the thermal energy input remained the same despite changing Φ. The lines of

constant FR are shown on the stability map, Figure 3.15 together with an annotation indicating the FR value. The relation between FR, Φ, and midpoint wall temperature is shown in Figure 3.18. The reported midpoint wall temperature is an average value obtained from the measurement of three thermocouples in both channels closest to the middle point of the reactor at positions -10mm, 0mm, and +10mm (6 total). There was a linear temperature drop with lowering Φ at all FR levels despite the same amount of power being delivered to the device. This was expected due to leaner flames containing a higher quantity of excess air that had to be heated by the fixed amount of available energy. Increasing the FR between 0.8 kW and 1.6 kW produced a consistent increase in midpoint temperatures, however, the 2.2 kW noted a smaller relative increase. This indicates that the heat exchange became insufficient at this FR level for efficient energy recirculation and the reactor approached the overall maximum FR value. The finding is further supported by temperature profiles shown in Figure 3.16, where the maximum inlet velocity, 250 cm/s, resulted in lower temperatures than the 200 cm/s case. At 250 cm/s the reactor operated close to the blow-off as the heat recirculation was insufficient to fully preheat the incoming reactants. This finding highlights the importance of heat recirculation during the high FR operation.

Temperature profiles for a range of Φ values at $\mathrm{FR}_{LOW} = 0.8$ kW and $\mathrm{FR}_{HIGH} = 2.1$ kW are presented in Figures 3.19 and 3.20 respectively. At low power operation, Figure 3.19, mixtures nearer to stoichiometric were prone to flashback due to the flame speeds being greater than the associated low inlet velocities. At higher FR, Figure 3.20, leaner mixtures stabilized nearer the mid-line. Further reduction of Φ would result in insufficient heat recirculation to keep the flame inside the channel leading to a blow-off condition. This shows that high power yet very lean conditions are most sensitive to the efficiency of heat recirculation.

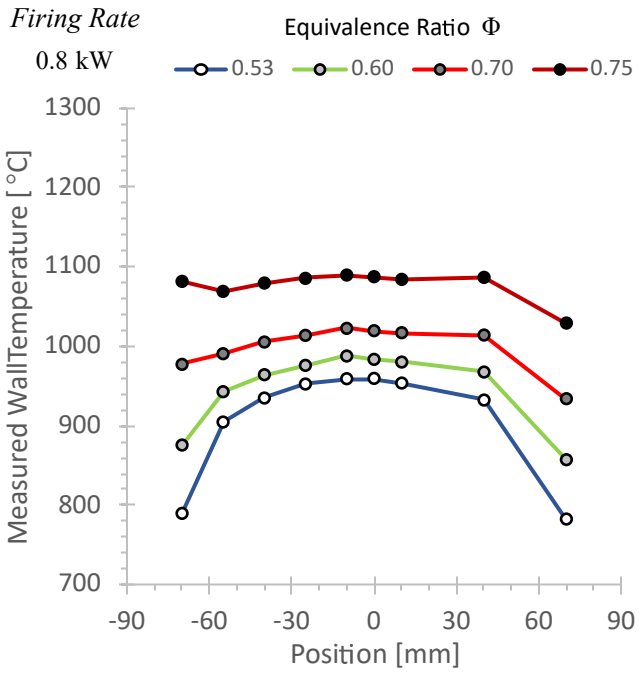

Figure 3.19: Straight Geometry: wall temperature profiles at a range of Φ for constant $\mathrm{FR}_{LOW} = 0.8$ kW

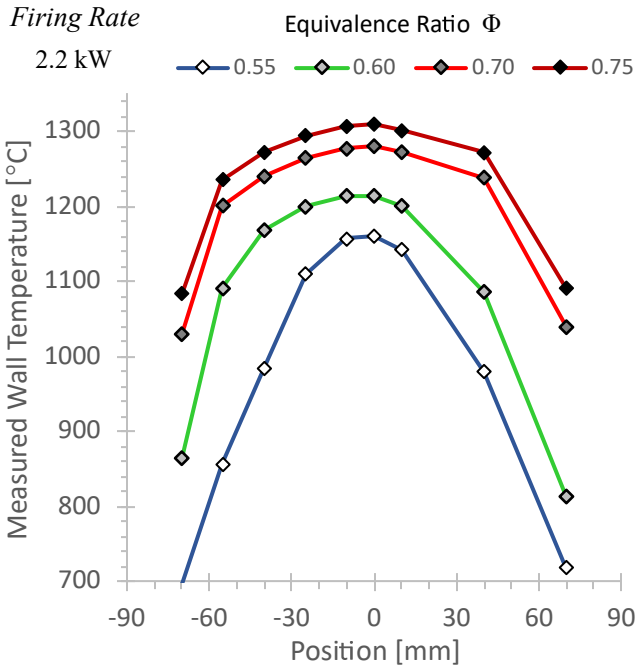

Figure 3.20: Straight Geometry: wall temperature profiles at a range of Φ for constant $\mathrm{FR}_{HIGH} = 2.1$ kW

3.3.4 Sound

The operation of the straight AM reactor was accompanied by a loud, high-pitched continuous sound at the intensity necessitating the use of hearing protection. The

	Inlet Velocity [cm/s]							
Φ	75	100	125	150	175	200	225	250
0.5	X	X	X	830	840	X	840	X
0.53	X	X	X	812	840	828	855	?
0.55	790	825	?	864	860	855	870	929
0.6	803	835	850	886	903	927	940	H
0.65	823	840	900	924	934	951	H	H
0.7	853	911	?	932	984	984	H	H
0.75	859	931	958	H	H	H	H	H

Figure 3.21: Straight Geometry: sound frequency map for a range of Φ and inlet velocities

sound was generated only when the flame was present and the acoustic power increased with higher Φ. It immediately disappeared when the flame extinguished. The compiled sound frequency measurements are presented in Figure 3.21, where X implies no stable flame, ? stands for missing value and H indicates no data due to the upper-temperature limit. The frequency lines for constant FR at a range of Φ are shown in Figure 3.22.All frequencies below 825 Hz were characterized by a wide peak with a low signal-to-noise ratio (SNR) making them nearly indistinguishable from the background sound of flowing gas. Higher frequencies have a sharp, distinct peak on the frequency spectrum and a significant SNR of 30 dB or higher. Moreover, weaker harmonics were identified at higher frequencies. Both figures show a mild linear correlation between the sound frequency with Φ. Similar behavior can be observed for the midpoint wall temperature shown in Figure 3.18, which suggests that frequency shift is related to a temperature within the reactor.

3.3.5 Emissions

The AM reactor produced low levels of CO and NO_x emissions that were close to the sensitivity limits of the MRU gas analyzer. The combined measurements for CO and NO_x emissions at two values of Φ and varying inlet velocity are presented in Figure 3.23. CO levels increased with both the inlet velocity and Φ as indicated by the best-fit dashed line. Notably, both lines converge at trace ppm levels at low velocities.Meanwhile, NO_x readings remain insensitive to flow velocity but change with the mixture's Φ. NO_x levels remained an order of magnitude lower than the adiabatic flame equilibrium prediction of 1103 ppm_{NOx} for $\Phi = 0.55$ and 2393 ppm_{NOx} for $\Phi = 0.7$. Observed behavior supports previous findings by Belmont and Ellzey on a handmade counter-flow combustor [42].

A closer look into CO emissions is presented in Figure 3.24 with all measurements organized by constant FR. A full kinetics simulation of a laminar flame indicated shorter CO chemistry timescales than the flow residence time for all but the fastest flows. Therefore, the plot includes equilibrium predictions at constant temperature and pressure for CO over a range of product temperatures close to exhaust conditions. There is a significant dependence of measured CO on the FR level in agreement with the increase of wall temperatures shown in Figure 3.18. For low FR, CO remains low and nearly independent of Φ, similar to the equilibrium calculation at low product temperatures. At higher FR, the CO production increases for richer mixtures, as predicted by the equilibrium at higher exhaust temperatures. Furthermore, at FR = 1.5 kW and FR = 2.2 kW, CO levels increase again as the mixture approaches the lean operational limit, $\Phi < 0.6$. Faster inlet velocities associated with those operating conditions reduce the residence time in the proximity of chemical timescale, leading to a departure from equilibrium. This behavior agrees with previ-

ous observations by Belmont et al. [42] for a similar counter-flow combustor operating at leaner conditions ($0.4 < \Phi < 0.48$).

NO_x emissions for constant FR are presented in Figure 3.25. Equilibrium values are not shown as they are at least an order of magnitude higher than the measured values. The timescale of thermal NO_x creation is substantially higher than the residence time. Therefore, equilibrium does not correctly predict NO_x emissions. Instead, the figure shows the prediction for flame-generated NO_x determined from a Cantera simulation [14] using GRI-Mech 3.0 kinetic mechanism that includes nitrogen chemistry [92]. Simulations were conducted for inlet temperatures of 300 K and 600 K, with the higher value representing the effect of heat recirculation in the combustor. Most of the measured points follow a single trendline indicating that NO_x production depends on the stoichiometry of the mixture only. The visible divergence of certain points is associated with low FR, high Φ conditions in which the flame has flashed back. Under nominal operation, the NO_x levels decrease for leaner mixtures, similar to analytical prediction. The vertical shift between measurement and simulation suggests that small amounts of thermal NO_x form downstream of the flame front.

3.4 Diverging Geometry - Changing Surface to Volume Ratio

The diverging geometry reactor is chronologically the first flow layout investigated in the AM core. The goal was to study the flame behavior as the ratio of wall surface area to channel volume decreases, hence limiting the available heat transfer. It was achieved via a diverging channel profile. The secondary goal was to validate the freeform capabilities of the AM process as the smooth sinusoidal shape of the wall was unattainable via traditional manufacturing means. Additionally, as the first attempted reactor experiment, the apparatus acted as a development platform for the flow delivery system bridging the legacy system used by Belmont [42] with a new one

described in Section 3.1. As such a dedicated sub-chapter 3.4.2 discusses the setup differences that should be taken into account.

3.4.1 Design

A straight channel has a near-minimum wall surface to volume ratio, $R_{A/V}$, at a given cross-sectional area. A diverging channel geometry, shown in Figure 3.26, was used to locally influence $R_{A/V}$, while maintaining the effective cross-sectional area of the reactor. The main feature of this reactor is a wall in the shape of a half-sine curve that expands the channel width from 4 mm to 8 mm as the flow continues downstream. The reduced channel height of 16 mm was accounted for in the volumetric flow supply to match the effective mean flow velocity of the remaining reactors. The change of local cross-sectional area reduced the gas speed by a factor of two between the inlet and the outlet while the mean velocity was equal to reported inlet velocity speed. The local speed reduction was found to have much lower significance for steady operation than the enhanced laminar flame speed change due to heat recirculation. The diverging section centered about the midpoint of the reactor with a long inlet and outlet section also aimed at shifting the flame position towards the middle. This combined with the increased flow velocity in the 4 mm section was intended to reduce the risk of flashback. Due to a small inlet channel width, it was necessary to incorporate ceramic headers that housed inlet pipes as seen in Figure 3.27. This picture shows the reactor under a steady operation with the top insulation removed. The white blocks at the edges of the reactor adapted the 3/16" ($\approx$ 4.8 mm) inlet pipe to the narrow flow channel.

3.4.2 Special Considerations

The early version of the experimental apparatus used in the diverging reactor experiments is shown in Figure 3.28. The flow delivery system used only the high flow configuration, therefore the few data points below 100 cm/s carry increased velocity and Φ uncertainties. Furthermore, the cross-balancing between channels was achieved with only two rotameter-valve assemblies, one per direction of flow. Therefore a per-channel control was not possible. The influence of the ceramic flow headers discussed above should be also taken into account. The temperature was recorded by the same 18 N-type thermocouples, however, spaced equidistantly along the channel as indicated by designed holes in Figure 3.26. Finally, there were no emissions nor sound measurements attempted for this geometry.

There was a major change in the thermal insulation strategy: the reactor was embedded between two grooved refractory insulation bricks. The external CAD view of a completed assembly is shown in Figure 3.1. This thermal solution proved to be inferior to the kaowool insulation due to increased heat low and overall thermal mass. The good thermal interface between the brick and AM reactor meant that the supporting assembly had to be preheated to a higher operational temperature before a steady-state could be achieved. The considerable thermal mass resulted in unacceptably long preheating and settling times. Furthermore, the increased heat loss affected the low FR operation leading to an extinction at sub-100 cm/s inlet velocities.

3.4.3 Operating range

The stability map for the lean operation is presented in Figure 3.29. The upper velocity limit was not reached due to a maximum temperature limit of Si-SiC material.

The highest steady-state temperature of 1320°C was recorded at $\Phi = 0.8$ and inlet velocity of 184 cm/s. The stability map suggests, however, that operation closer to stoichiometric could be achieved at even higher flow velocities as long as the material is capable of withstanding higher temperatures.

The observed lower stable limit was closely tied to the firing rate. At FR = 0.8 kW the heat release rate was insufficient to overcome losses. The flame could not sustain reactions as the temperature continued to drop further reducing the temperature. This positive feedback loop led to flame extinction. Furthermore, the stable flow conditions just above of the extinction line (FR = 0.8 kW) experienced periodic oscillations in flame position accompanied by the audible feedback. Similar behavior was observed by Vogel in a two-section porous ceramic burner [57]. The reactor achieved the ultra-lean operation at low inlet velocities of around 125 cm/s. However, the leaner Φ limit again increased with higher inlet velocity due to a reduction in $R_{A/V}$ as the flame stabilized in wider sections along the diverging section. The diverging geometry reduces the heat recirculation in the zone, where it was most important for flame stabilization - high FR with high inlet velocity. The built-in flashback arrestor prevented the flame from fully propagating through the inlet section at high Φ operation. Instead, the flame lingered at the flame arrestor site, so an actual flashback could not be observed. Therefore an "arrested" flame condition was defined according to the criteria presented in section 3.1.

3.4.4 Wall Temperatures

The wall temperature profiles along the length of the channel are plotted in Figures 3.30 and 3.31. Figure 3.30 investigates the difference between high $\Phi = 0.7$ and low $\Phi = 0.51$ operation. The faster laminar flame speed of the richer mixture combined with a locally higher degree of heat recirculation allowed stabilization near the narrow

section of the reactor over all inlet velocities. Higher velocities at $\Phi = 0.7$ have increased the bulk temperature, however, without influencing the overall profile shape. It indicates that the flame remained at the same position over the inlet velocity range. Meanwhile, the lower Φ has the shape indicating a near blow-off condition. The bulk temperature remained completely unchanged over the velocity range indicating that the combustion is constrained by reduced $R_{A/V}$ due to the channel width increase. The change of temperature profile with equivalence ratio increase is shown in Figure 3.31 at a constant inlet velocity of 150 cm/s. It shows that increased Φ allows the flame to stabilize further upstream of the channel midpoint. The improved local $R_{A/V}$ at flame position causes the profile shape to be wider indicating an improved heat transfer thorough the reactor.

The importance of heat transfer is highlighted at constant FR, Figure 3.32. The moderate equivalence ratios, $0.6 \leq \Phi \leq 0.7$ showed a well-developed dome shape characteristic for stable operation. At $\Phi < 0.6$ the flame position near the midpoint of the reactor experienced reduced amount of heat recirculation due to channel diverging shape. This led to a reduced preheat amount and lower peak temperatures. Further reduction of equivalence ratio caused flame blow-off. In contrast, a high $\Phi > 0.7$ resulted in a shape that indicates the flame stabilized at the flame arrestor. Notably, the peak temperature location also is shifted upstream near the inlet, a further indication of the importance of the flame arrestor.

Midpoint wall temperatures for various FR values over a range of Φ is shown in Figure 3.33. At equivalence ratios below 0.65 all but the highest FR show a nonlinear decrease in temperature due to reduced $R_{A/V}$ at the location of the flame. At higher equivalence ratios at FR = 0.8 kW and FR = 1.1 kW show a slight reduction in wall temperature near the midpoint of the reactor. This happens due to the fact that flames at those conditions are stabilized further upstream of the reactor indicated

arrested operation. Therefore the midpoint wall temperature does not coincide with the peak temperature withing the combustor, as seen in Figure 3.32 for $0.7 \leq \Phi \leq 0.9$. The Φ at which the steady-to-arrested transition takes place is higher for bigger FR values due to higher associated inlet velocities.

3.5 Split-channel Geometry – Extended Surface Area

The complex split-channel reactor geometry demonstrated the potential of additive manufacturing in combustion research. The freeform capability enabled an intricate flow-path that increased the exposed wall surface area by 50% while maintaining the original cross-sectional area. The increased $R_{A/V}$ had improved the heat transfer within the narrow part of the reactor, which influenced the entropy recirculation.

3.5.1 Design

The split-channel design is presented in Figure 3.34. This reactor design aimed at increasing the $R_{A/V}$, hence enhancing the solid-gas heat transfer while the the effective cross-sectional area of the flow remained unchanged. It was achieved by an additional narrow wall in the middle of the channel that created two narrower co-flowing sub-channels within. To accommodate the splitter wall thickness the overall width of the channel had to be increased. The flow entered through the inlet pipe into a 4 mm wide entry length of the channel, as in the diverging design. The entry was followed by a diverging section bringing the overall width to 8 mm until the splitter-wall separated the flow into two 3 mm channels. The splitter wall resided between the inlet and the mid-point of the reactor to cover the range of stable flame positions. Subsequently the channel converges to 4 mm past the mid-point. This allowed for a global symmetry in the cross-flow pattern of the reactor.

The range of stable flame position was within the 3mm sub-channels, between

x = -50 mm and x = -5.5 mm, as indicated by "stable flame" in Figure 3.34. Theoretically the sub-channel should stretch to the midpoint (x = 0) to accommodate the full range of stable flame positions. This was not possible in this design due to symmetry limitations. Under sufficiently low inlet velocities the flame propagated upstream of splitter wall and was trapped by the diverging inlet section, an "arrested" mode of operation. The ability of studied geometry to safely contain the flame within the AM structure allowed for further investigation of the reactor's capabilities at low velocity. Further velocity decrease below $\approx$ 50 cm/s resulted in an actual flashback, where the flame entered the steel tube at the inlet.

3.5.2 Operating Range

A detailed stability map is presented in Figure 3.35. The reactor demonstrated a wide operating range in the lean regime ranging from the methane flammability limit at $\Phi = 0.55$ up to stoichiometric $\Phi = 1$. The ability to work steadily at a material-safe temperature near the stoichiometric condition is a unique characteristic of this reactor. The operation on the lower end of Φ range was limited by a blow-off at higher inlet velocities and extinction at lower inlet velocities. It was not possible to distinguish between the two from the measurement data, hence both conditions were classified as lacking the stable flame. The split-channel device under high-velocity, high- Φ inlet was constrained by the Si-SiC upper operational temperature limit of 1414°C. This required substantial reduction in the inlet velocity, however it was possible to maintain an arrested operation up to $\Phi = 1$. At velocities below $\approx$ 50 cm/s and $\Phi >$ 0.65 an actual flashback was observed. It was accompanied by the rapid decrease of measured wall temperatures and a disappearance of combustion-induced sound. The arrested operation produced a substantial noise that followed by a flashback with no audible sound. A sustained quasi-steady operation under flashback was possible due

to the long, uninsulated inlet pipe acting as a flame thermal quench arrester.

3.5.3 Wall Temperatures

Figure 3.36 shows the collection of wall temperature profiles for a range of equivalence ratios at a constant inlet velocity of 100 cm/s. The bulk temperatures rose as the amount of fuel, hence FR, increased. Notably, all but the leanest profiles in the Figure 3.36 have a characteristic double-peak shape coinciding with the location of the splitter wall. This shows a higher wall surface area in sub-channels had improved the heat recirculation within the reactor, which led to locally higher temperatures. Similar behavior is also expressed under a constant FR = 1.1 kw comparison, Figure 3.37.

Transitions between steady, arrested and flashback modes of operations are well demonstrated by the wall temperature data presented in Figure 3.38 for constant $\Phi = 0.8$. Steady operation with velocities $\geq$ 100 cm/s was characterized by significantly higher temperatures thorough the main section, where the splitter wall increased the heat recirculation. At velocities from 75 cm/s to 50 cm/s the maximum temperature decreases with the velocity for the majority of the channel length. However, the entrance of a diverging section, x = -70 mm, remained at a relatively constant temperature indicating the proximity of the flame front. The temperature subsequently dropped at x = -55mm due to a locally reduced $R_{A/V}$ in the wider end of the diverging inlet section prior to the splitter wall. Under arrested conditions the flame only stabilized near the narrow end due to lowered heat transfer of the wider end. The velocities below 50 cm/s resulted in a temperature drop throughout the reactor because the flame propagated further upstream and entered the inlet pipe.

The change of midpoint wall temperature for various FR over a range of Φ is shown in Figure 3.39. Similar to a straight reactor, the midpoint temperature was

linked to the amount of energy input. However, the slope of best-fit lines also changes with FR in contrast to a nearly parallel lines of the straight reactor. The low FR lines are very shallow due to spanning over the arrested zone of operation, where the midpoint temperature remained relatively constant, as discussed previously. Meanwhile higher FR conditions covered mostly a steady operation, hence the midpoint temperature increased as the heat recirculation improved with higher Φ.

3.5.4 Sound

The operation was accompanied by a flame-induced standing wave within the channel at an approximate frequency of 800 Hz. Frequencies above 700 Hz the FFT showed a distinct peak and were the loudest during the arrested operation and near the high-temperature limits. Additionally, the arrested operation produced the secondary, weaker frequency peak within 50 Hz margin of the dominant one. The detailed frequency map is shown in Figure 3.40 for a wide range of inlet velocities and in Figure 3.41 at the lower end of inlet velocities associated with arrested operation. For both maps X implies no stable flame, ? stands for a missing value and H indicates the maximum material temperature limit. Additionally, Figure 3.41 indicates the dual-peak operation by * next to the reported main peak frequency. During the stable operation and inlet velocities at or above 100 cm/s, the sound monotonically increased with Φ and velocity, similar to the straight reactor.

3.5.5 Emissions

Steady-state CO and NO_x emissions are presented in Figure 3.42 at constant $\Phi = 0.65$ (a), constant inlet velocity of 100 cm/s (b) and at a constant FR = 1.5 kW (c). In most cases, the emissions of CO and NO_x remained significantly below the equilibrium prediction at a given equivalence ratio. At constant Φ, Figure 3.42a, the CO level

mildly increased at higher flow velocities, while NO_x remained constant thorough the velocity range. The repeated emission readings from the arrested zone and its proximity (velocities below 100cm/s in Figure 3.42a) carried a substantial statistical uncertainty due to a wide range of recorded values. This indicates the flame stability issues under arrested operation. The significant influence of equivalence ratio on both CO and NO_x is shown in Figure 3.42b. The NO_x level strongly increased with Φ as the higher flame temperatures enabled the nitrogen kinetic chemistry. CO response was less pronounced as it is related to the equilibrium chemistry at products temperature rather than prompt kinetics of the flame. This is further supported by analyzing data at constant FR = 1.5 kW, Figure 3.42c. The recorded emissions of CH_4 fluctuated between 20 ppm and 30 ppm, which is marginally above the uncertainty envelope. Therefore, CH_4 levels during the steady operation were considered as a trace. An additional experiment was performed with the cold reactor that identified the the permeability of the Si-SiC wall as probable source of trace amounts of unburned hydrocarbon, as discussed in section 3.1.1. During the operation near the flashback limit, the CH_4 readings increased to $\approx$ 300 ppm $\pm$50 ppm indicating substantial combustion instabilities.

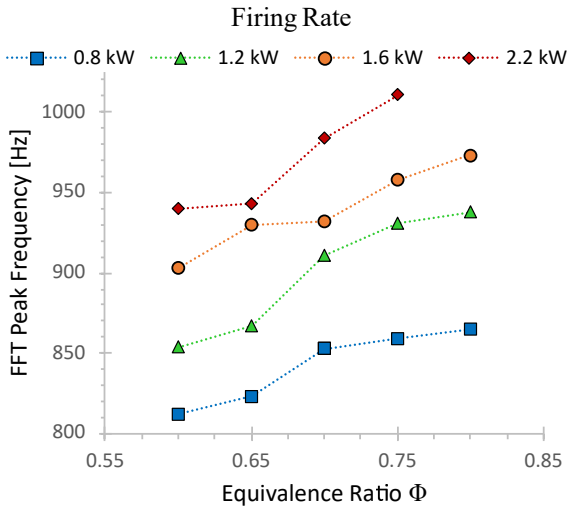

Figure 3.22: Straight Geometry: peak sound frequency observed during the operation – FR held constant

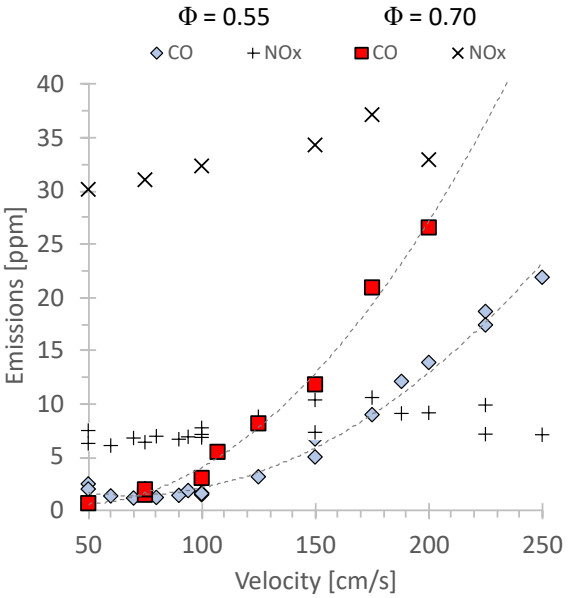

Figure 3.23: Straight Geometry: emissions vs velocity at two fixed values of $\Phi = 0.55$ and $\Phi = 0.7$

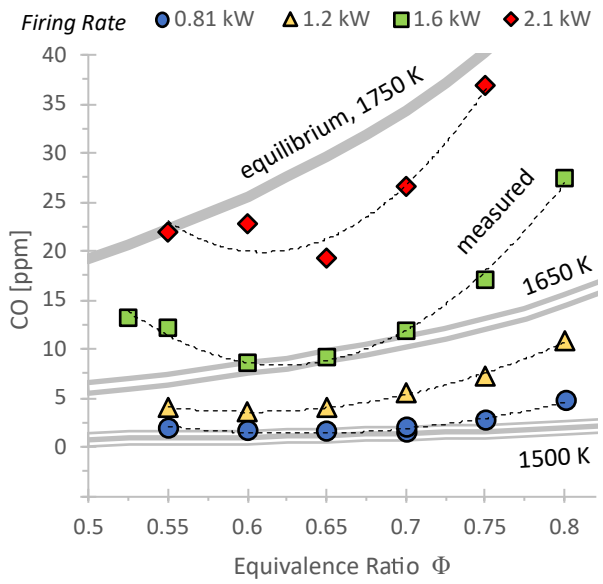

Figure 3.24: Straight Geometry: CO emissions against Φ range for various FR. Gray lines show equilibrium prediction for CO at specified temperature.

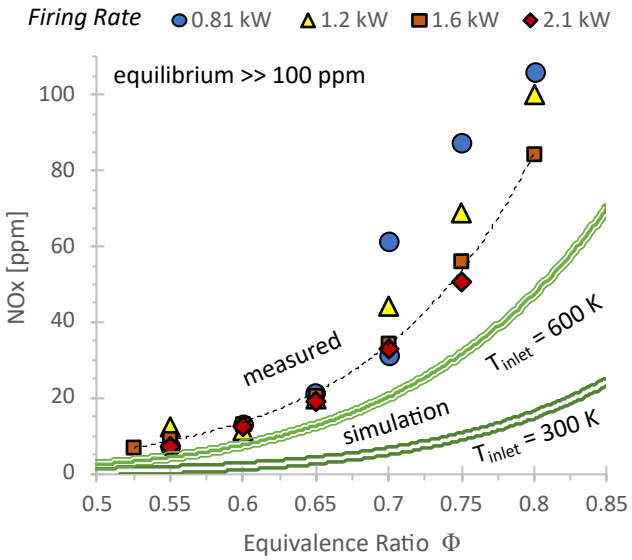

Figure 3.25: Straight Geometry: NO_x emissions against Φ range for various FR. Green lines show GRI-Mech 3.0 [92] kinetic simulation results for a flame-generated NO_x at two reactant temperatures.

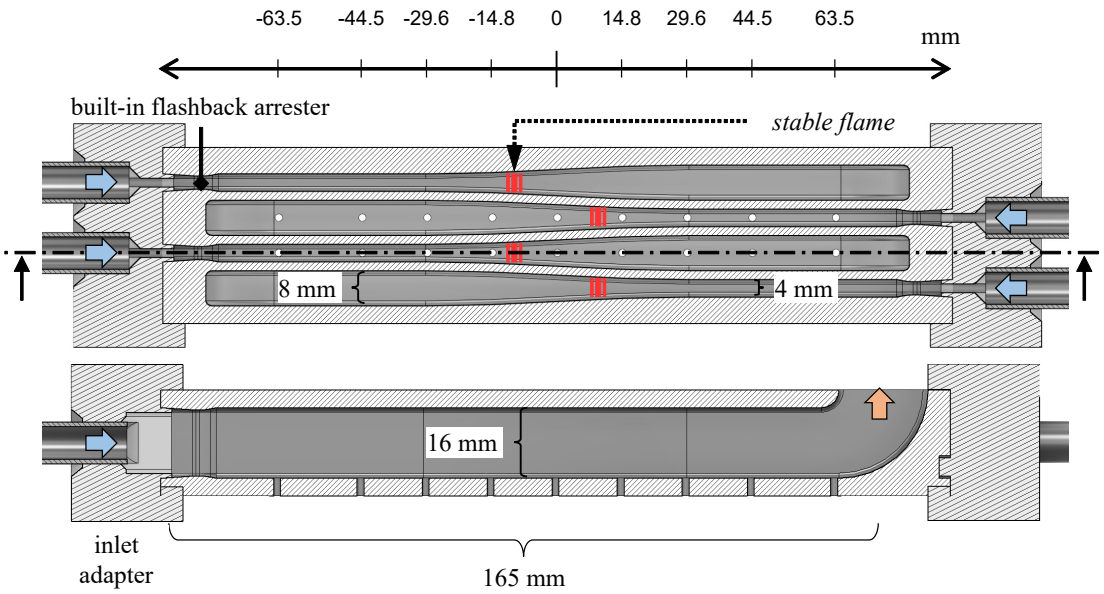

Figure 3.26: Divergent Geometry: reactor sketch - top view

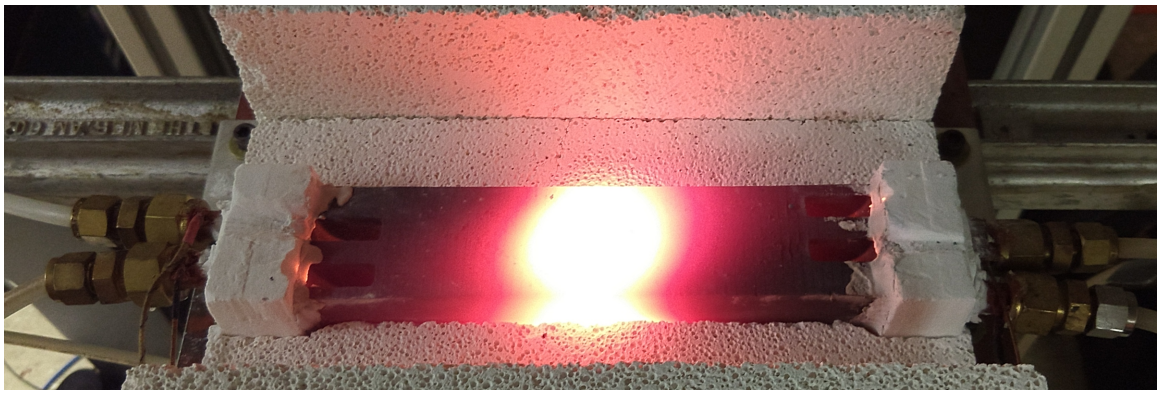

Figure 3.27: Divergent Geometry: reactor under operation with the top insulation removed

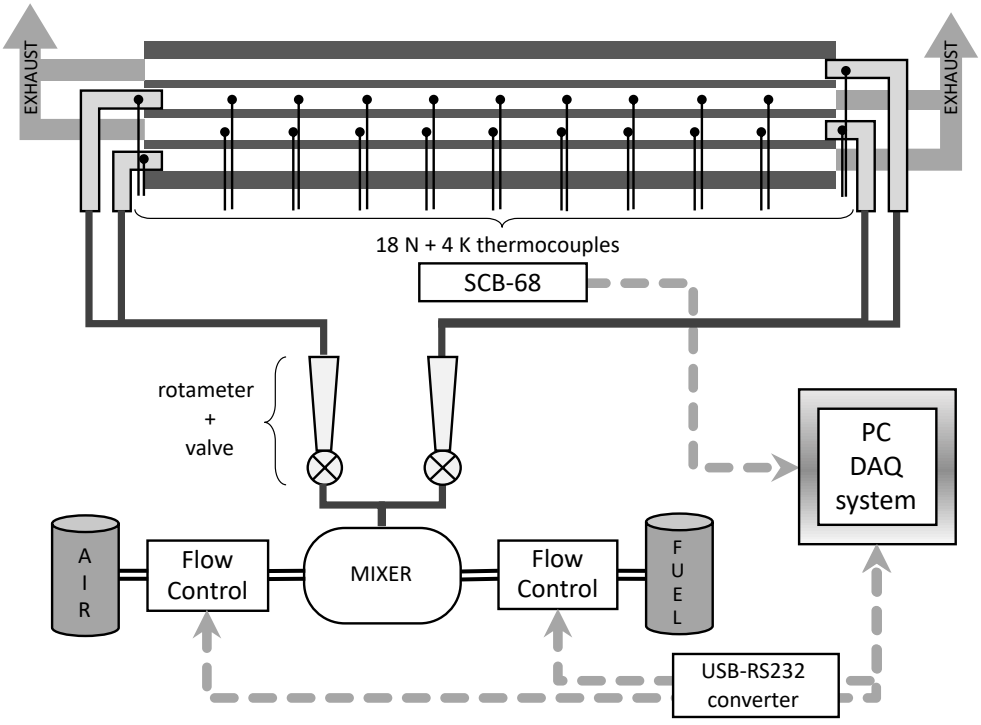

Figure 3.28: Divergent Geometry: Combustion apparatus sketch

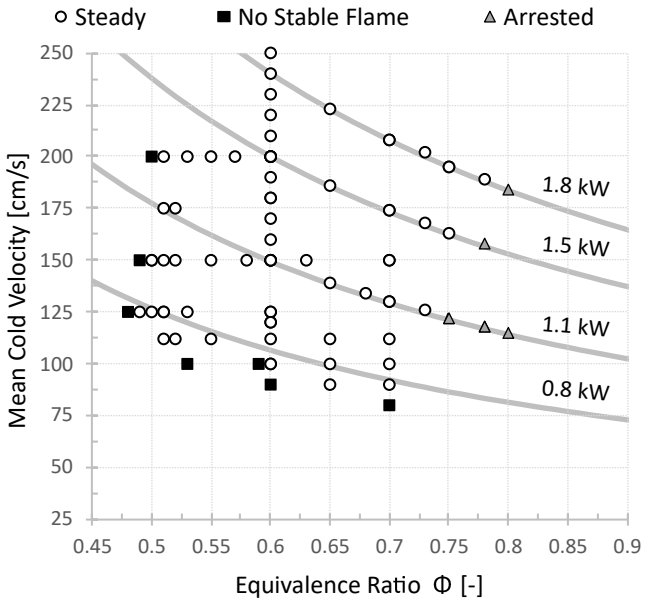

Figure 3.29: Divergent Geometry: stability map of the range of Φ and inlet speeds. Solid lines represent constant FR.

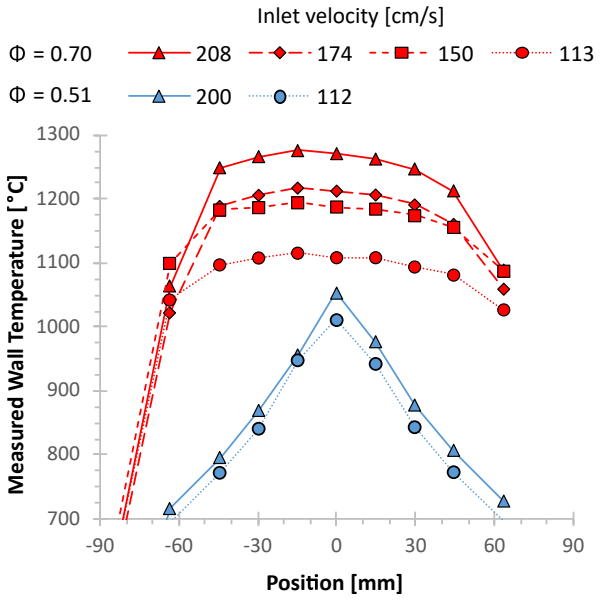

Figure 3.30: Divergent Geometry: impact of the inlet velocity on measured wall temperature profiles at two values of Φ

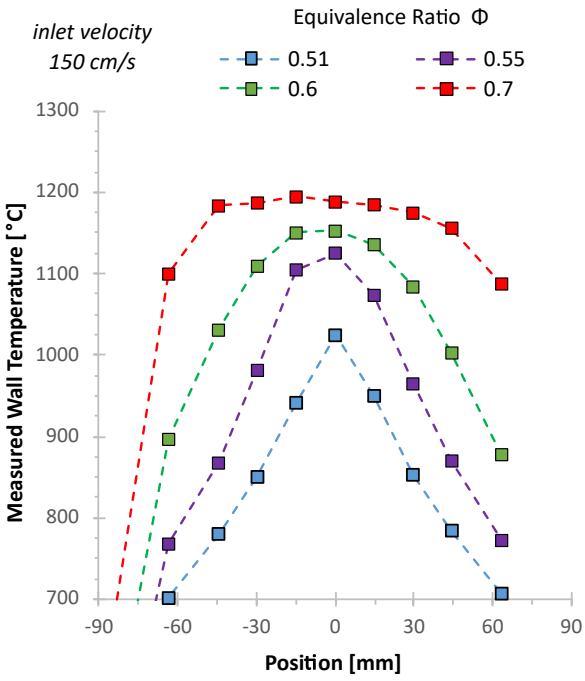

Figure 3.31: Divergent Geometry: impact of Φ on measured wall temperature profiles at inlet velocity of 150 cm/s.

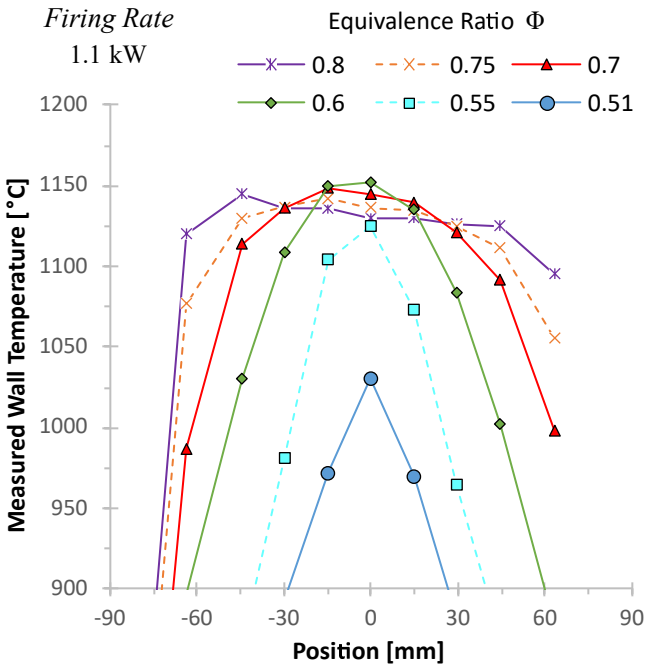

Figure 3.32: Divergent Geometry: wall temperature profiles at a range of Φ for constant FR = 1.1 kW

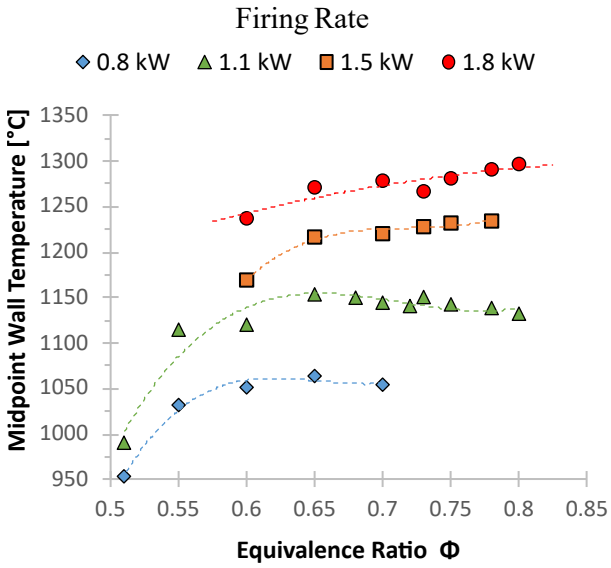

Figure 3.33: Divergent Geometry: averaged midpoint wall temperature vs velocity plot for a range of Φ

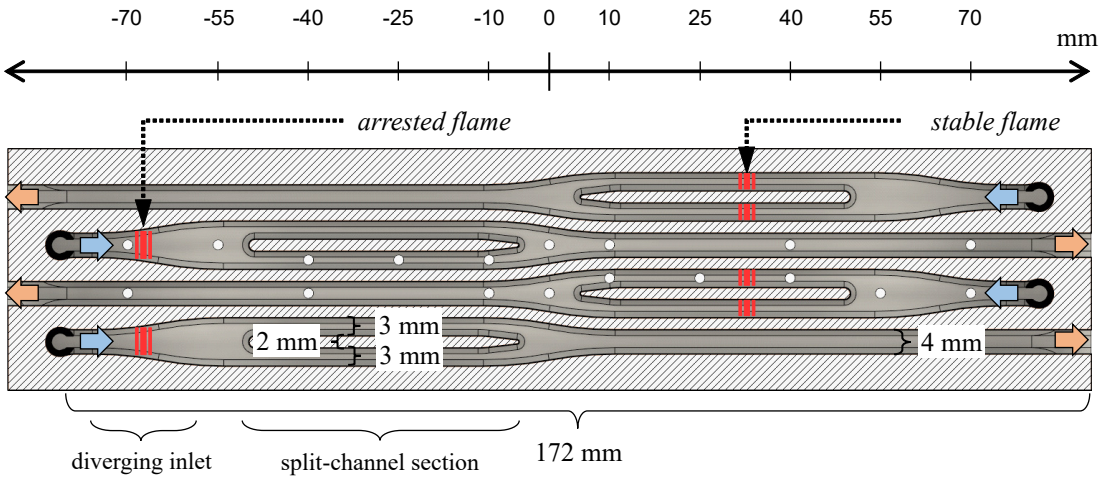

Figure 3.34: Split-channel Geometry: reactor sketch - top view

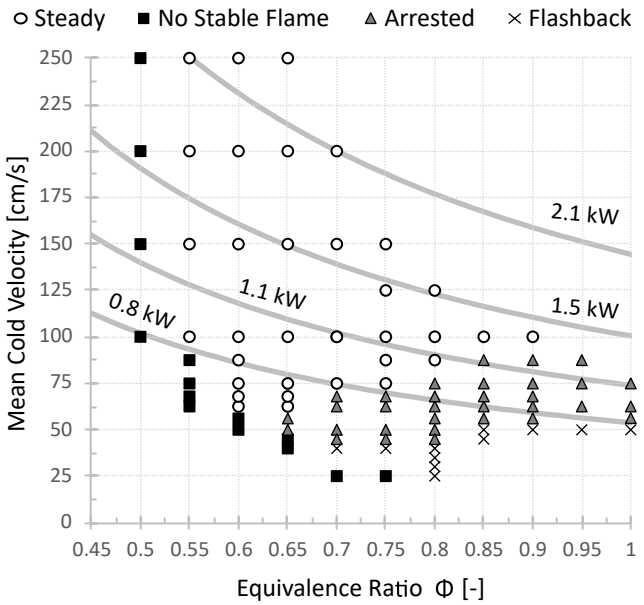

Figure 3.35: Split-channel Geometry: stability map of the range of Φ and inlet speeds. Solid lines represent constant FR.

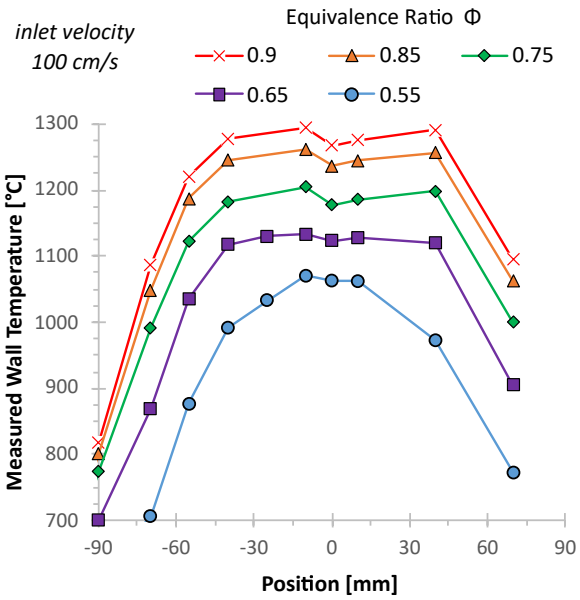

Figure 3.36: Split-channel Geometry: impact of Φ on measured wall temperature profiles at inlet velocity of 100 cm/s.

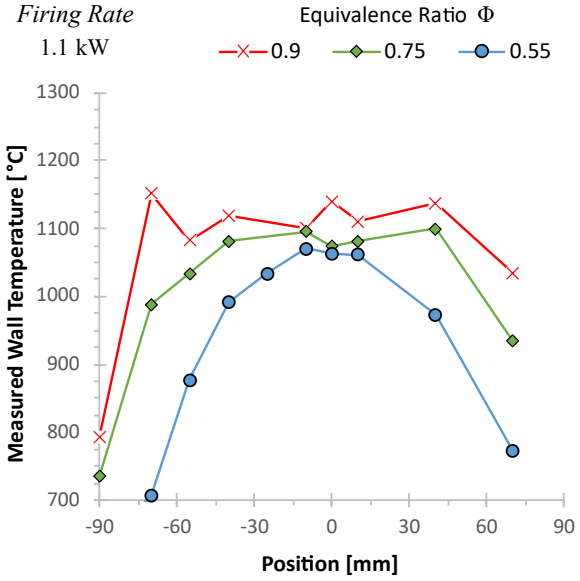

Figure 3.37: Split-channel Geometry: wall temperature profiles at a range of Φ for constant FR = 1.1 kW

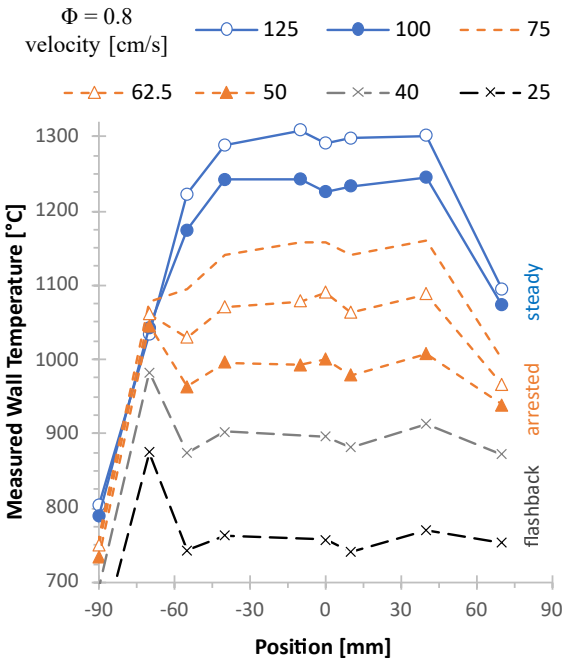

Figure 3.38: Split-channel Geometry: impact of inlet velocity on measured wall temperature profiles at fixed $\Phi = 0.8$.

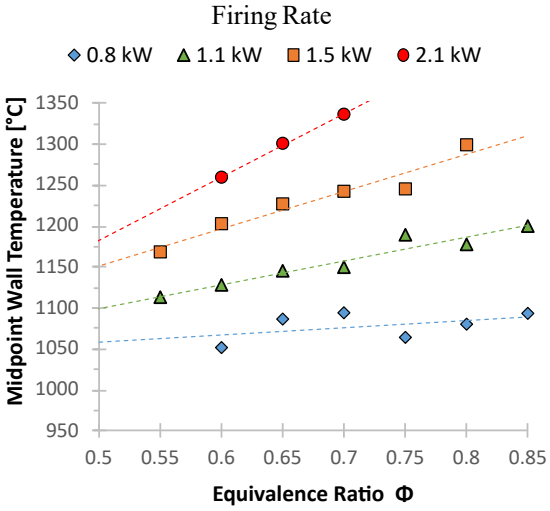

Figure 3.39: Split-channel Geometry: averaged midpoint wall temperature vs velocity plot for a range of Φ

	Inlet Velocity [cm/s]						
Φ	50	75	100	125	150	200	250
0.55	X	X	768	?	785	790	785
0.60	X	780	769	?	780	795	790
0.65	670	780	800	?	790	805	850
0.70	680	785	800	?	800	850	H
0.75	690	790	790	790	805	H	H
0.80	692	800	799	810	H	H	H
0.85	720	810	810	H	H	H	H
0.90	F	810	810	H	H	H	H
0.95	F	810	H	H	H	H	H
1.00	F	820	H	H	H	H	H

Figure 3.40: Split-channel Geometry: sound frequency map for a range of Φ and inlet velocities

	Inlet Velocity [cm/s]						
Φ	45	50	56	62.5	75	87.5	100
0.55	X	X	X	X	X	X	768
0.60	X	X	X	700	780*	740	769
0.65	X	670	686	780	780*	?	800
0.70	672	680	?	760	785*	?	800
0.75	680*	690	?	770*	790*	805*	790
0.80	685*	692	700	780*	800*	815*	799
0.85	693	720	724*	790*	810*	800*	810*
0.90	F	F	770*	790*	810*	800*	810*
0.95	F	F	?	795*	810*	800	H
1.00	F	F	785	800*	820	H	H

Figure 3.41: Split-channel Geometry: sound frequency map for a range of Φ and low inlet velocities

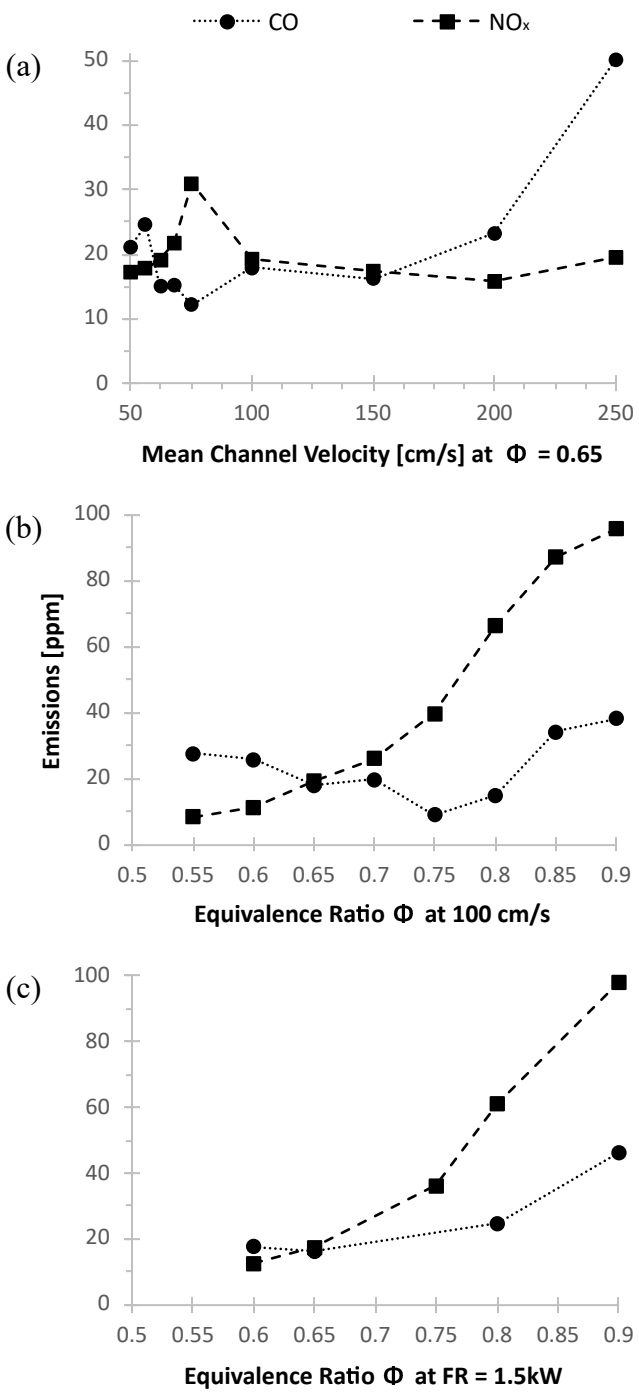

Figure 3.42: Split-channel Geometry: CO and NO_x emissions data at a) $\Phi = 0.65$ b) inlet velocity of 100 cm/s c) FR = 1.5 kW

3.6 Comparison of AM reactors

This section is concentrated on the comparison between the three AM geometries. Figure 3.43 shows the top view of the three reactors under the same scale factor. Arrows show inlets (blue) and outlets (orange), while the indicated flames show the most likely positions under a steady operation. The following Figure 3.44 shows the handmade reactor made by Schoegl and Ellzey [6] that was subsequently used by Belmont et al. [42] for, among others, the lean premixed methane combustion experiments. Those results is included in the comparison as a performance representation of a reactor made with the traditional manufacturing method. The handmade reactor was made with top and bottom blocks of carved zirconia and perpendicular silicon plates that formed the channels, as shown in Figure 3.44. The width of the channel was 4 mm, 33% narrower than AM reactors. The importance of this parameter is examined in section 3.2.2.

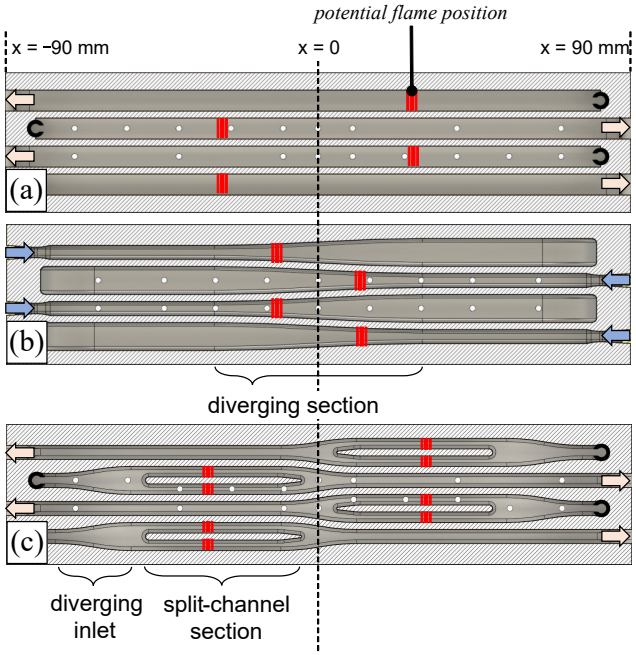

Figure 3.43: Cross-sectional top view of AM reactors: a) straight b) diverging c) split-channel

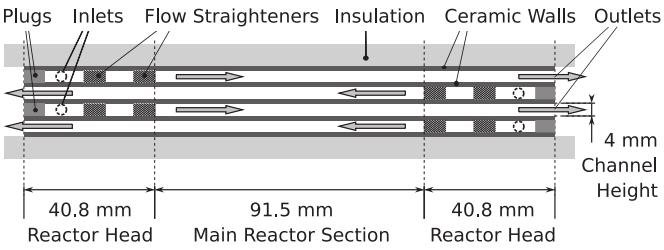

Figure 3.44: Schematic view of previous hand-made heat recirculating reactor by Schoegl and Ellzey [6]

3.6.1 Operating Range

Stability maps for the three AM designs and the handmade reactor [42] are presented in Figure 3.45. All AM reactors (b-d) showed a wide range of stable operating conditions under lean methane combustion. In contrast, the handmade reactor achieved an ultra-lean operation, yet was not able to stabilize the flame at higher equivalence ratios due to flashback issues. Among the AM-produced designs, the split-channel reactor (d) showed the widest operating range extending up to stoichiometric mixture $\Phi = 1$. The diverging channel design was unique in that both flow velocity and $R_{A/V}$ changed along the length. The locally increased heat transfer in the narrower inlet section allowed the diverging design to reach leaner operating conditions. The geometry of the diverging channel design also limited the stability at low velocities as the low FR flames that stabilize near middle point faced reduced $R_{A/V}$. This decreased heat recirculation leading to lower burning rates, thus limiting the operation of the reactor. This feedback loop also limited the low velocity, low Φ operation of the split-channel reactor. Under those conditions the flame would reside diverging region just upstream of the splitter wall, which also had locally lower $R_{A/V}$.

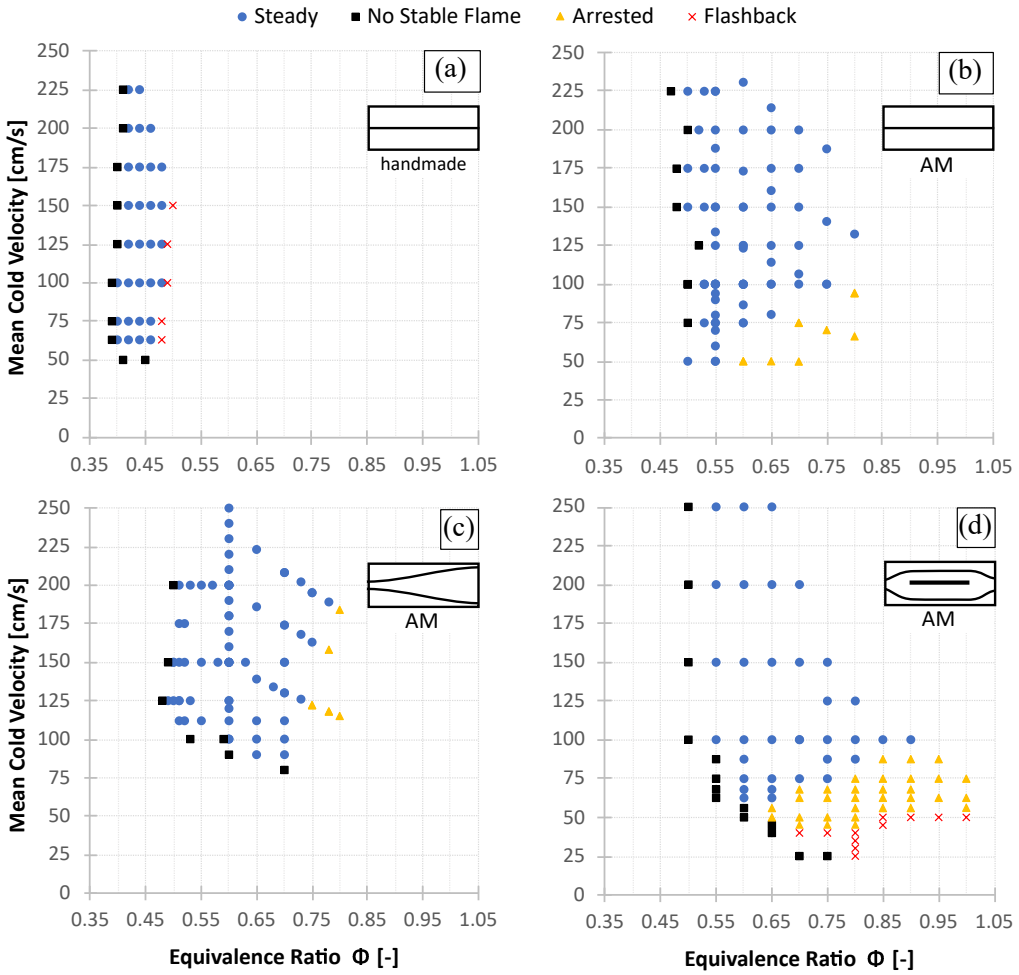

Figure 3.45: Stability maps for experimental reactors: a) previous handmade [6, 42], b) AM straight channel c) AM diverging channel d) AM split-channel

3.6.2 Analytical Model

The previously introduced analytical model provides insight into relative performance of discussed reactors. The differences in AM reactors' geometries, thermal properties, and flow characteristics were represented through the system variables listed in Table 3.6. The parameters used by Belmont et al. [42] excluded the inlet section length occupied by flow straighteners, which required the inlet temperature parameter to be higher to account for preheating. In the current analysis, the full length of the reactor was used, which allow for 298 K cold inlet condition. This modification imposes a limit

to the usable nondimensional length between $-0.53 < x < 0.53$ for the handmade reactor.

		Modified handmade	AM reactor
Geometry factor	ϵ	0.0116	0.0034
Conductivity factor	κ	139	96.2
Heat transfer factor	μ	0.2717	0.0116
Wall heat loss factor	ψ	0.050	0.025
Radiative solid heat loss	σ	0.710	0.932

Table 3.6: Analytical model parameters used in comparison

The comparison between split-channel and straight channel reactors is presented in Figure 3.46. The increased heat transfer of the split-channel reactor leads to higher stable velocities, as shown by the dash-dotted line. The effective flame stabilization distance of the split-channel reactor is shortened to the length of the splitter wall, which reduced the stability range at lower inlet velocities. Meanwhile, the simple straight channel design allows nearly full length of the reactor for flame stabilization. This, coupled with the lower heat transfer coefficient μ due to a wider channel width, results in a greater stability range. The analytically predicted behavior is reflected in the experimental stability maps, where at low velocities the straight reactor, Figure 3.45b, has a wider operating Φ-range than the split-channel reactor, Figure 3.45d.

Analytical predictions using new model parameters to represent the handmade reactor of Belmont et al. [42] at $\Phi = 0.45$ and $\Phi = 0.55$ and the straight channel reactor at $\Phi = 0.55$ is shown in Figure 3.47. The model suggests that a stable operation in the handmade reactor at $\Phi = 0.55$ can be achieved only at very high inlet velocities.

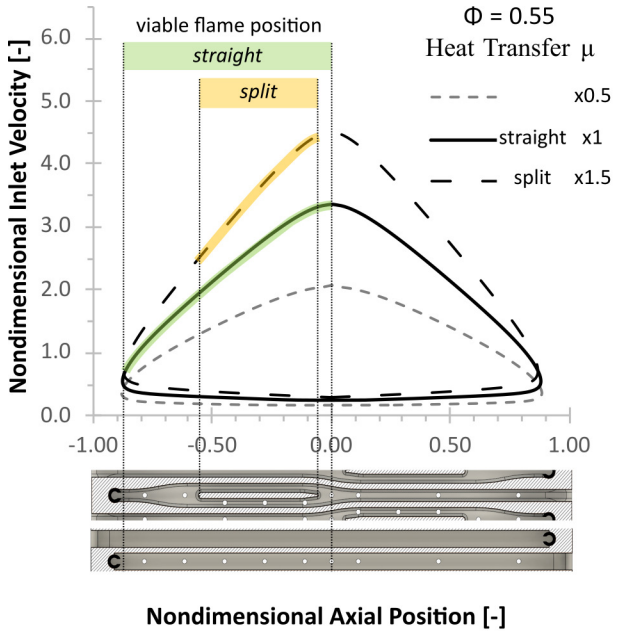

Figure 3.46: Analytical predictions for AM straight and AM split-channel reactors including geometric limits

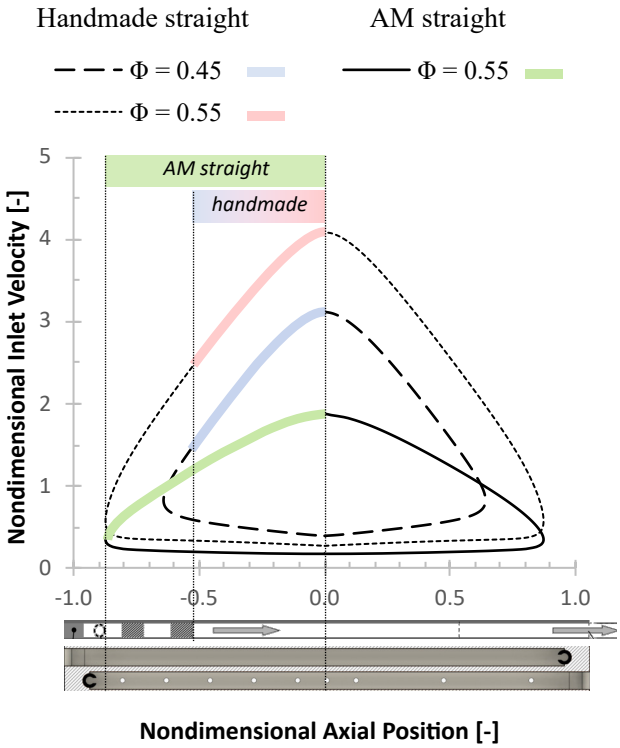

Figure 3.47: Analytical predictions for AM straight channel and handmade reactor [6]

Under those conditions the temperatures would exceed material limits, which explains the narrow operating range observed experimentally. Reducing Φ to 0.45 decreases the stable inlet velocity to the range supported by the given reactor configuration. Meanwhile, the geometry of straight AM reactor and associated thermal properties result in overall lower inlet velocities required for stable operation. This combined with longer available channel length allows for a significantly increased range of stable operation, although at a cost of ultra-lean operation.

3.6.3 Temperature Distribution

The detailed behavior during steady-state operation between the three AM reactors is compared for all designs based on wall temperature profiles at steady-state. Figure 3.48 show the temperature profiles for all 3 designs at varying inlet velocity (left) and Φ (right). Note the $\Phi = 0.6$, 150 cm/s case is repeated in both columns. The shape of the temperature profile carry the information about the location of the flame within reactor. The peaked profile in the diverging reactor indicated that the flame existed near the middle of the reactor whereas a flatter profile in the straight channel reactor indicates the flame was stabilized further upstream, closer to the inlet. The maximum temperatures for the diverging and straight reactor were consistently lower than in the split-channel design, which supports a higher heat recirculation within the split-channel reactor. As the velocity increased to 200 cm/s, the diverging channel experienced a significant reduction in temperature despite the higher FR value. This shows the importance of the heat recirculation as the diverging channel with reduced $R_{A/V}$ was not capable to efficiently preheat incoming reactants. In contrast, the temperatures of straight and split channel reactors increased at 200 cm/s, since designs had higher $R_{A/V}$ and remained limited by material capabilities only. The temperature profile for various Φ shown on the right of Figure 3.48 further

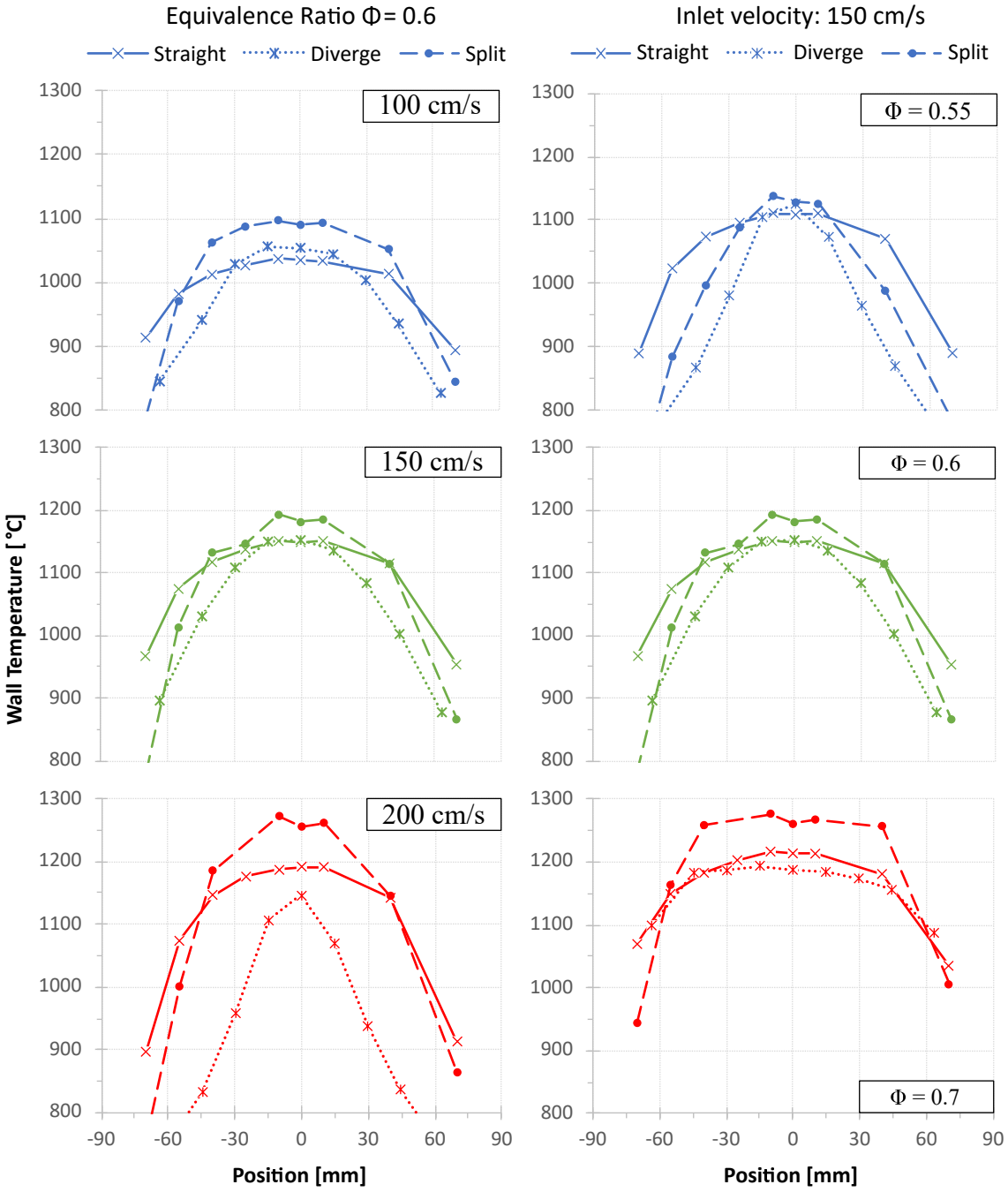

Figure 3.48: Wall temperature comparison between AM reactors over Φ (left) and inlet velocity range (right).

highlights the importance of heat transfer in the steady operation of this reactor type. Leaner conditions caused the flame to propagate nearer the midpoint, where the effective length of heat recirculation is reduced. Nonetheless, the increased heat exchange in the narrow sub-channels in split-channel design led to higher maximum temperatures. This shows the importance of heat recirculation in a lean, high-velocity region. At the richer condition, $\Phi = 0.7$, the heat transfer was not as important for stable operation as all profiles had similar shape indicating that the flame had stabilized in approximately the same position in all reactors. At $\Phi = 0.7$ the split-channel reactor's the flame was located near the upstream edge of the splitter wall. With a further increase of Φ, the flame would jump and stabilize near the throat of the diverging inlet section, an arrested operation. This is an undesirable mode of operation with an unstable flame and increased CO, NO_x, and CH_4 emissions.

Figure 3.49 shows the range of wall temperature profiles for the three reactors at constant FR $\approx$ 1.5 kW over a range of Φ values. The diverging channel reactor displayed a full range of operating states from a near blow-off to an arrested flame as Φ increases from 0.55 to 0.8. Straight and split-channel reactors do not reach the arrested operation at the same Φ range. This shows the high sensitivity of counter-flow heat recirculating reactor to a degree of heat transfer, as predicted previously by the analytical model. The peak temperatures were the highest in the split-channel reactor, followed by a straight design. The lowest peak temperatures were observed in the diverging geometry. The temperature variation between reactors is directly linked to the amount of heat transfer available. Uniquely for the diverging reactor peak temperatures are nearly identical over a range of Φ. It is a result of the varying $R_{A/V}$ along the length of the reactor, hence changing with the flame position. Straight and split-channel geometries were designed for constant $R_{A/V}$ during stable operation, which produced the peak temperature gradation with Φ. Additionally,

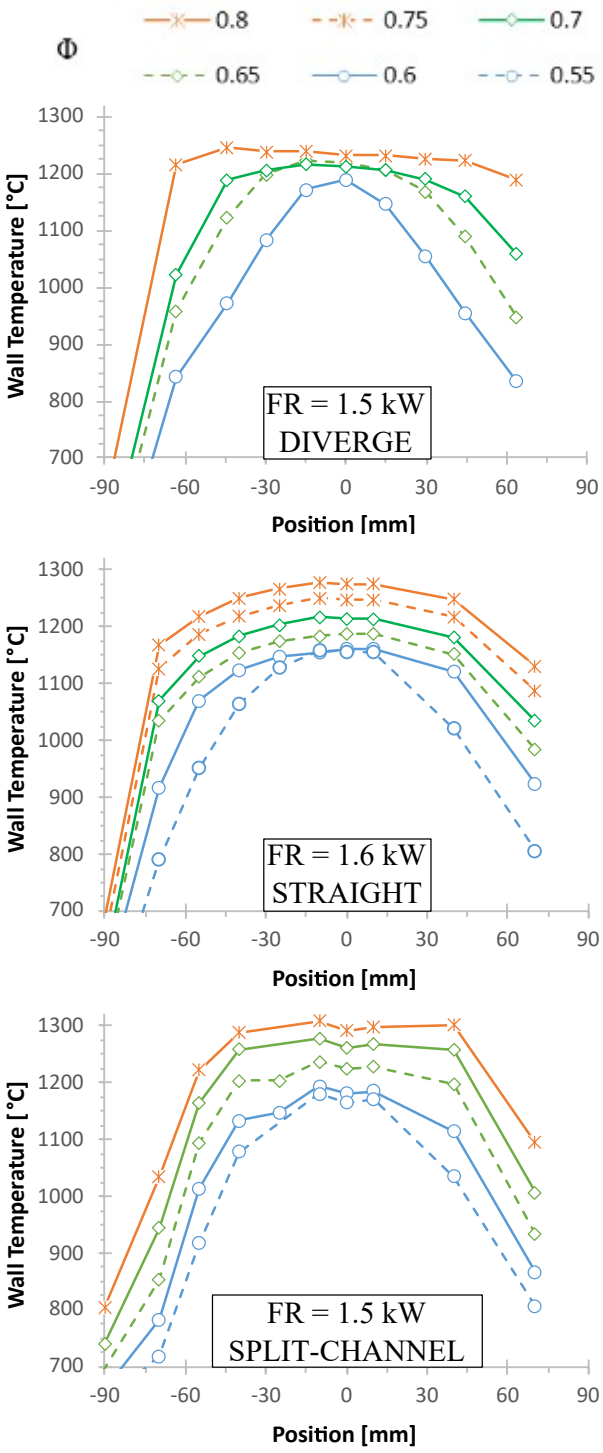

Figure 3.49: Wall temperature profiles for AM reactors at FR near 1.5 kW.

the split-channel design contained the diverging inlet section forcing the flame further downstream. This manifested in narrower wall temperature profiles that concentrated closer to the middle point in the split-channel temperature plot.

3.6.4 Sound

The sound data for straight and split-channel reactors were discussed in the respective sections. Figure 3.50 shows the comparison between the two for multiple velocities and a range of equivalence ratios. The sound frequency demonstrated a strong dependence on inlet velocity and Φ in a straight channel. This is not true in the split-channel reactor, where the scaling with velocity and Φ was very small. In both cases, the sound was produced induced by the flame into a standing wave in the channel. Simplistic application of a standing wave theory predicts the frequency in the 700 Hz to 1000 Hz for the length of the channel and assumed thermodynamic properties at 1000°C. The exact frequency depending on the effective speed of sound in the reactor, that changes with gas temperature. The straight reactor accommodates the $1/4^{\text{th}}$ of the wave over

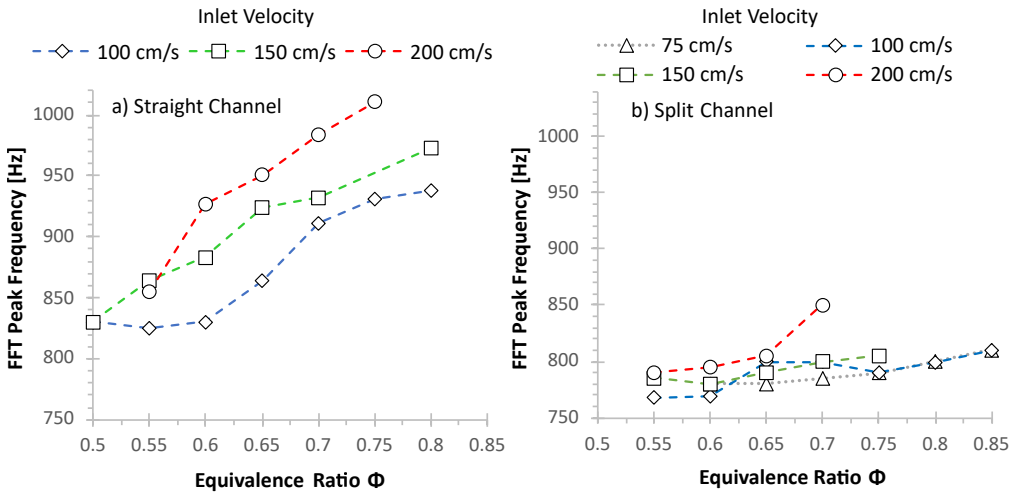

Figure 3.50: Recorded sound peak frequency in a) straight channel and b) split-channel geometries

its full length, hence the effective speed of sound was influenced by the colder reactants entering the device. Therefore the produced frequency were higher and dependent on flame position. In the case of split-channel geometry, the channel path was obstructed by the splitter wall, therefore a simple standing wave could not account for the sound generation. Instead, a complex acoustic system was formed that would require further analysis.

3.6.5 Emissions

The comparison of emissions data for the straight and split-channel reactor is shown in Figure 3.51 for measurements of CO (left column) and NO_x (right column). Continuous double lines show equilibrium and kinetic simulation predictions for CO and NO_x respectively. Both reactors followed general trends of increased emissions at higher Φ and no NO_x sensitivity to the inlet velocity. The split reactor produced consistently higher levels of CO and lower amounts of NO_x than the straight reactor. The CO increase was especially pronounced at constant inlet velocity, Figure 3.51c, at lower Φ, where the flame resided in the narrow 4 mm section of the split-channel reactor. The narrower channel housing the flame caused higher flow velocities and lowered residence times insufficient to break down the remaining CO. The NO_x emission improvements occurred at higher Φ, near or at the arrested operation. In this case, the increased complexity of split-channel design improved mixing, which reduced the flame-generated NO_x. The CO levels at FR = 1.5 kW, Figure 3.51e follow the temperature trends shown in Figure 3.49. The straight channel has lower peak temperature at $\Phi \approx 0.65$, leading to smaller CO emissions that match the 1650 K equilibrium prediction. At higher $\Phi \approx 0.8$ both reactors have similar maximum temperatures, hence converging at the equilibrium prediction for 1700 K combustion.

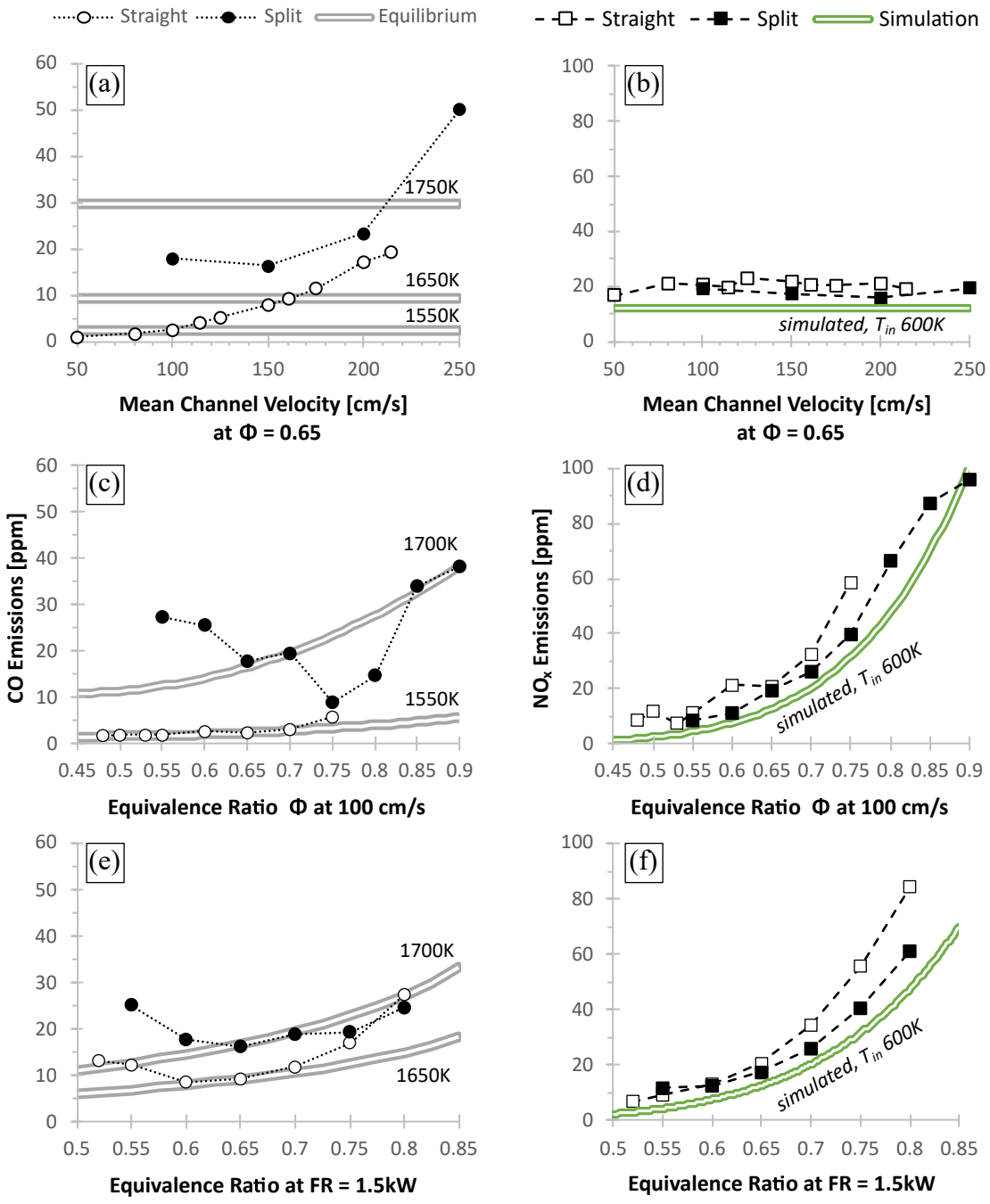

Figure 3.51: Emissions data comparison at a) CO at $\Phi = 0.65$ b) NO_x at $\Phi = 0.65$ c) CO at inlet velocity of 100 cm/s d) NO_x at inlet velocity of 100 cm/s e) CO at FR = 1.5 kW f) NO_x at FR = 1.5 kW

3.7 Material Performance

The thorough high-temperature properties characterization is a complex process outside the scope of the current research project. The following subsections present data on the preliminary evaluation of Si-SiC efficacy in a combustion environment. First, the Si-SiC was exposed directly to a flame to test the endurance under these conditions. Subsequently, the damage to the experimental reactors is evaluated after the combustion testing. Although deficient for proper material characterization, this approach provides a preliminary look at the applicability of Si-SiC material in prolonged combustion applications.

3.7.1 Sustained flame exposure

The impact of the combustion environment on the Si-SiC material was evaluated by a flame exposure test as discussed in section 3.1.2. The conditions of lean combustion were representative of typical combustion devices. The high temperature "1260°C" test covered a high FR, near stoichiometric application with low levels of O_2 in reactants. Meanwhile, the "1000°C" sample was exposed to a substantially leaner flame

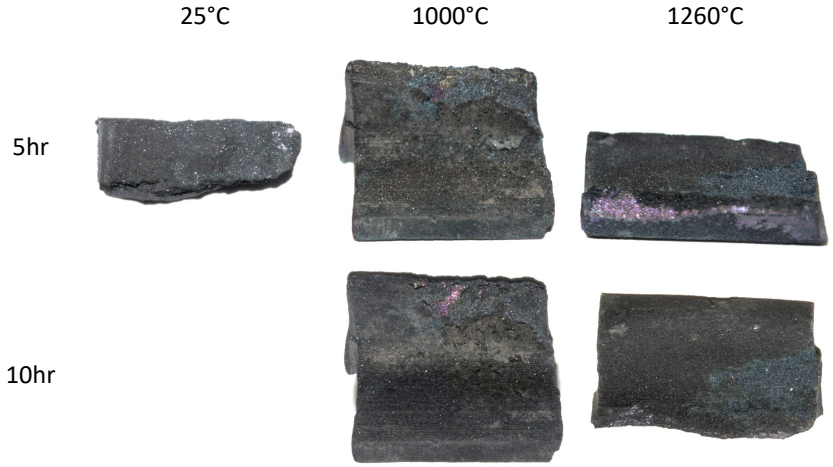

Figure 3.52: Photos compilation of Si-SiC samples at various stages of flame exposure testing

with lower FR, yet higher P_{O_2}.Photos of the samples at 5 hour intervals are presented in Figure 3.52. Mass, volume, and density changes are presented in Table 3.7.

Case	**Time**	**Mass change**	**Volume change**	**Density change**
1000°C	5hr	- 0.06 %	+ 5.6 %	- 5.3 %
1000°C	10hr	- 0.02 %	- 6.7 %	+ 7.1 %
1260°C	5hr	- 0.17 %	+ 4.2 %	- 4.2 %
1260°C	10hr	+ 0.03 %	+ 7.8 %	- 7.2 %

Table 3.7: Detailed mass and volume changes of Si-SiC parts exposed to flame.

During the original 5 hour interval, the high-temperature sample lost 0.17% of its original mass compared to 0.06% mass loss for the low-temperature case. This occurred despite a lower oxygen content of the high-temperature flow. However, further oxidation showed the 1260°C sample experiencing a mass gain indicating the passive oxidation. This type of oxidation is beneficial for the long-term life of the part as the growing oxide layer forms a diffusive barrier that substantially limits further deterioration. This is in agreement with Ernstberger findings [69] that even at such low oxygen concentrations (P_{O_2} = 0.0192 atm) the Si-SiC experiences a passive oxidation after the initial period of mass loss. Meanwhile, 1000°C sample continued to that lose mass after 10 hours, indicating undesirable active oxidation. The SEM image of the surface of both samples, shown in Figure 3.53, shows that the lower temperature case creates shell-like oxide structures that are not well attached to the surface. This finding is further confirmed by examining the photographic evidence in Figure 3.52. The front surface of the part is visibly cracked and actively spalling, which explains the recorded mass loss. In contrast, the high-temperature samples show a well-integrated SiO_2 oxide layer. It occurred because 1260°C is above SiO_2 glass transition temperature. Therefore, the newly formed oxide was able to viscously

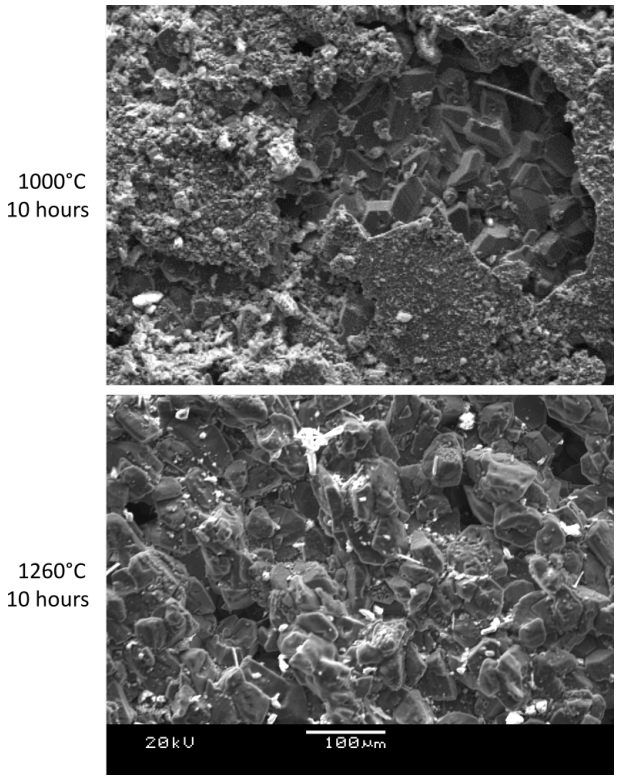

Figure 3.53: SEM images of Si-SiC samples at the end of experiment

flow and conform to the evolving surface. In the case of 1000°C sample, the oxide behaved as a crystalline solid, hence the surface spalling and continuation of active oxidation. The Energy-Dispersive Spectroscopy (EDS), shown in Figure 3.54 also proves the material oxidation is higher in 1260°C despite lesser visible damage and a lower oxygen prevalence in the flow. Meanwhile, the low-temperature sample shows lower oxygen levels as the SiO_2 is actively removed from the part. This preliminary small-scale study identified a critical characteristic impacting the long-term lifetime of Si-SiC and SiC parts in the combustion environment. A thick oxide layer forming a diffusion barrier is a necessary feature for a durable high-temperature material. The limited data suggest that long-term use of Si-SiC and SiC is possible for temperatures above the glass transformation temperature of SiO_2 (≈ 1200°C). The upper temperature is prescribed by the melting point of silicon metal (1414°C). A narrow operating

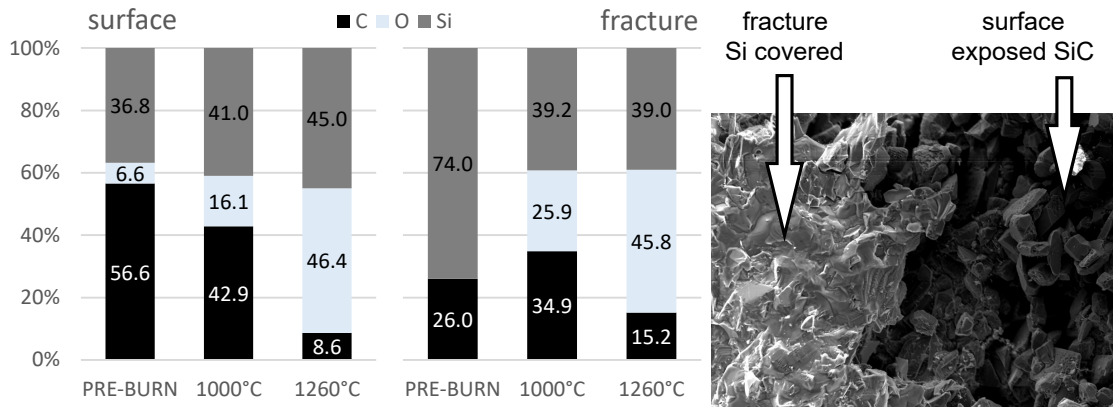

Figure 3.54: EDS atomic concentrations of the Si-SiC before and after the exposure

temperature window is problematic in practical applications, where devices develop temperature gradients across their length. An intentional passivation step can potentially alleviate the spalling issues at lower temperatures during the finishing process. The isothermal hold above $\approx 1200°C$ under an oxidative atmosphere will naturally grow the well-anchored protective layer that should not experience as severe spalling issues at lower temperatures.

3.7.2 Experimental reactors

The combustion tests of experimental reactors were not instrumented for a detailed investigation of material damage sustained during the operation. All devices operated in an unchanged fashion through the entire set of experimental runs required to collect the required combustion data. Each reactor experienced at least 80 hours of operation with at least ten complete cool-down and warm-up cycles. The good thermal shock resistance of Si-SiC and higher thermal mass of the assembly have significantly reduced the material stresses during the startup procedure. The three reactors presented no issues with high thermal gradients where a hot flame impinged on the cold wall during the startup. Good conductivity with higher thermal mass

provided a safe and slow heating period that did not affect the longevity of the reactor. This came in contrast to previous handmade devices made from ceramics, which increased their temperature quickly while emitting cracking noises. It indicated microcracks forming in purely ceramic devices due to excessive thermal stresses.

Through all the combustion tests, the material on the outside surfaces of the reactor remained unaffected. Internal surfaces, experiencing the highest heat and direct exposure to flame, were inspected visually via the borescope video probe at regular time intervals. All pictures presented below show one of the inner channels (i.e. the channels surrounded on both sides by internal wall, not exposed to environment) with the exact position stated in the description. The surface degradation of the straight channel reactor is shown in Figure 3.55. The pictured section of the channel holds the flame during the nominal operation. Si-SiC material showed minimal degradation after 80 hours of operation with a few flakes on the wall. This degradation mode is consistent with the SiO_2 spalling discussed in section 3.7.1 for a lower temperature sample. The oxide spalling rate is sufficiently low that any flakes are continuously removed by the flow and do not accumulate. Notably, the thermocouple sheath, made

Figure 3.55: Internal surface degradation of the straight reactor: channel midpoint looking upstream - the hottest zone

of high nickel stainless steel, sustained substantially greater damage than the channel wall.

The experiments on a split-channel reactor showed a substantially higher degree of degradation, as shown in Figure 3.56 for two locations. Importantly the pictured passages are 2 mm narrower than in the straight channel case (6 mm). The first 20 hours showed a similar oxidation behavior to the straight channel. This period covered a low FR operation with moderate temperatures (1100°C to 1200°C). The subsequent 20 to 40 hours period involved the high FR operation experiencing the highest heating and maximum temperatures. This resulted in new protrusions at positions experiencing the maximum temperatures (up to 1380°C). New growths

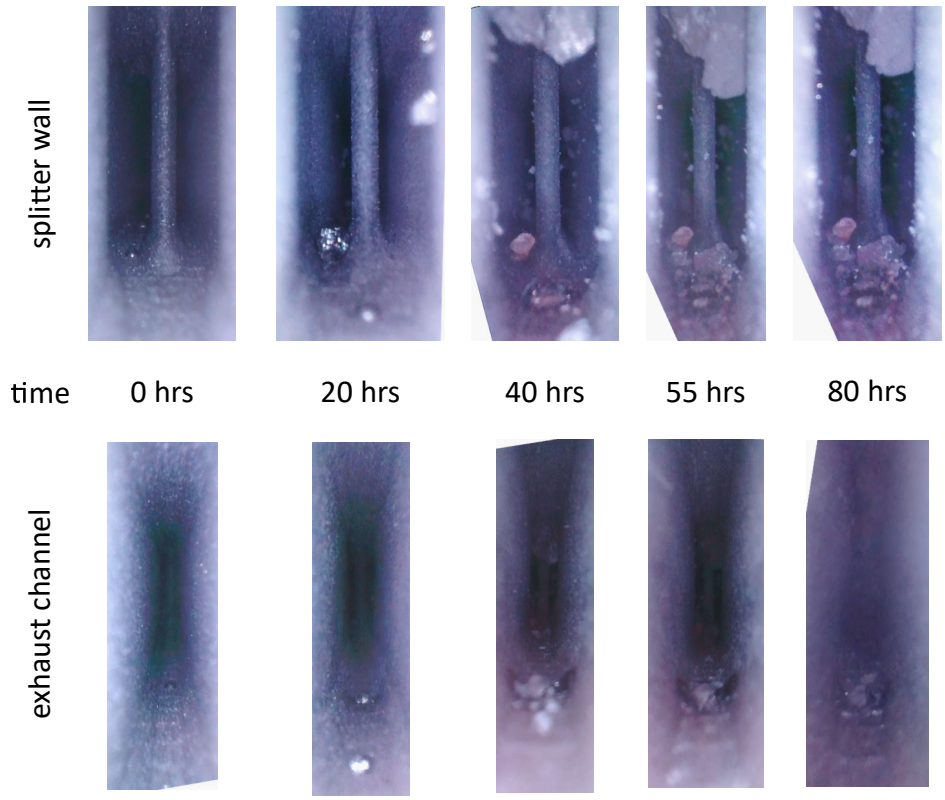

Figure 3.56: Internal surface degradation of the split-channel reactor: (top) splitter wall from the channel midpoint - the hottest zone (bottom) exhaust channel past the midpoint

were usually spherical and loosely attached to the wall. After reaching a critical size, they detached and were carried downstream with the flow. A particular obstruction prominent at the top of the channel in Figure 3.56 has grown so much that it could not clear the narrow exit section. The majority of the protrusions remained small enough to clear the channel. During the remaining time, the reactor worked in a low FR mode investigating the arrested operation. The lower temperatures reduced the creation rate of protrusions. Subsection 3.7.3 further discusses this degradation mode. The exhaust channel downstream the flame did not experience a similar protrusion growth thorough the whole testing period.

The diverging reactor shows the most compelling case of oxidation damage. The reactor operated without insulation during the initial 10 hours, which required a significantly higher FR for sustained operation. The visual observation of surface damage during that period is shown in Figure 3.57. The borescope images show the section upstream of the middle point that varied from 4 mm to 6 mm in width. Within the first 5 hours, the protrusion appeared. The 5-hour picture shows the initial stage of protrusion forming with smooth, metallic skin. By a 10-hour mark, the new growth significantly obstructed the channel. Once the protrusion reached a

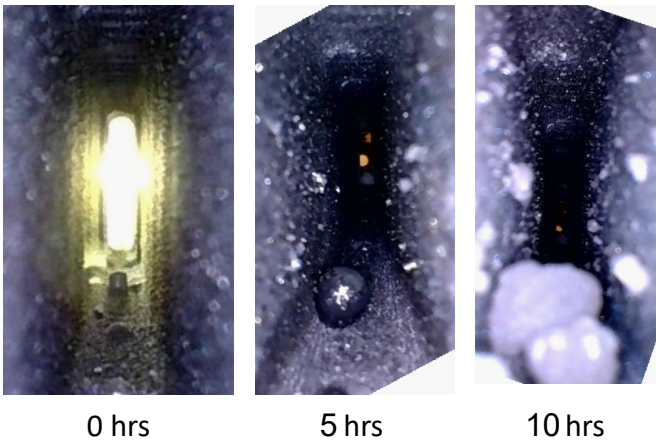

Figure 3.57: Internal surface degradation of the diverging reactor: first 10 hours

specific size, the outer surface became more irregular and opaque, as seen in the 10-hour picture. Additionally, the wall surface also shows the SiO_2 flakes characteristic for previously observed Si-SiC deterioration mechanism. At 10 hours, all channels were mechanically cleaned, and the insulated reactor was investigated following the same procedure at the other two types. The wall oxidation progress for that period is shown in Figure 3.58. Only the oxide spalling was observed with no further protrusion growth.

The combustion tests performed on Si-SiC reactors have found the material to be a suitable solution for experimental combustion applications. Long-term (1'000 hours or longer) oxidation experiments and more in-depth material testing are required to evaluate the suitability of industrial applications. The narrow operating temperature range, 1200°C to 1400°C, and a continuous oxide shedding might be considerable limitations for more general applications.

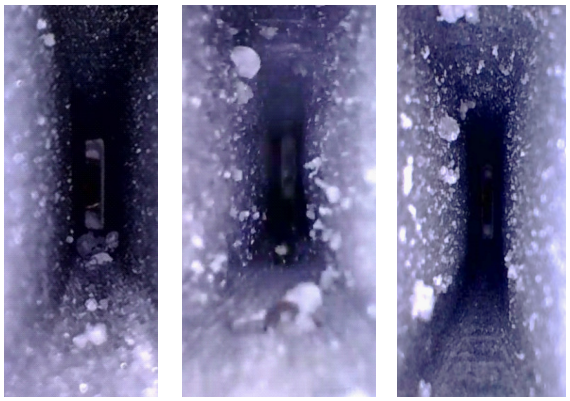

Figure 3.58: Internal surface degradation of the diverging reactor: after mechanical cleaning, remaining test period

3.7.3 Channel protrusions

The generation of solid chunks, 0.2 to 4 mm in diameter, is a substantial indication of material degradation and an issue for practical applications. The smaller particles were usually spherical and metallic in appearance. A more prolonged exposure caused further growth into an irregular shape and opaque. A representative sample was recovered from the diverging reactor and inspected under an electron microscope SEM. The obtained pictures are presented in Figure 3.59. The outer surface is a smooth oxide skin, akin to the oxidation results of Si-SiC at high temperatures, discussed in section 3.7.1. The EDS acquisition was unsuccessful as the smooth surface acted as a mirror, such that the acquired spectrum showed the composition of the SEM chamber. The cavity in the upper end of the object was a suitable target for EDS. The analysis showed the prevalence (80% atomic +) of silicon with the remainder filled by oxygen and carbon. Furthermore, overexposure of the shaded area of the cavity shows surface features characteristic of polycrystalline metal solidification. Similar silicon

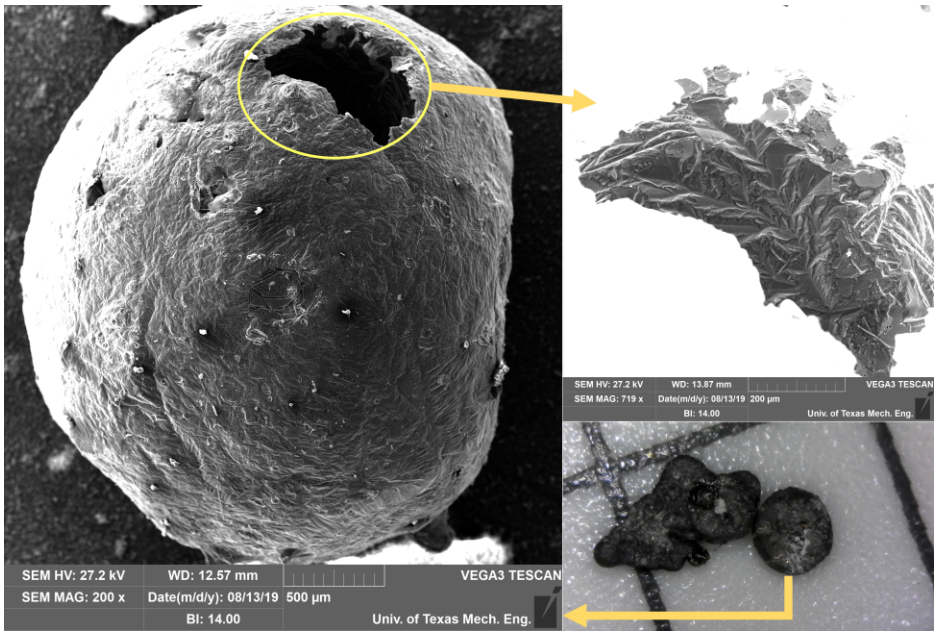

Figure 3.59: SEM imagining of protrusion ball formed inside the reactor

bead formation was reported by Rezaei et al. [93] for Si-SiC lattice samples under 1400°C air atmosphere. Based on their findings, the local concentration of impurities depresses the melting point of silicon alloy. Silicon upon melting shrinks facilitating the oxidation within the structure via micropores. The newly formed subsurface SiO_2 has a lower density, which causes the internal stresses that squeeze the molten silicon alloy into the surface. Finally, the low wettability of silicon on SiO_2 causes the formation of beads and eventually coalesce into bigger structures. The silicon formation process is detrimental to the lifetime of the material as expelled silicon leaves open porosity that accelerates the oxidation process. This can be observed in Figure 3.58, where the amount of SiO_2 spalling was significantly higher than in other reactors due to initial Si beads formation in the 0-10 hours period.

The beads formation in the current set of experiments occurred during the periods of high FR, high-temperature operation. Furthermore, the issues were the most pronounced in the two internal channels, where temperatures were higher than in the outer channels exposed to a higher degree of heat loss. Finally, the recorded temperatures come from the bottom of the channel, which leaves the possibility of even higher than recorded temperatures near the middle height of the channel. Therefore the Si beads formation threshold, ≈ 1350°C constitutes the upper-temperature limit of the material for a long-term operation.

Chapter 4: Conclusions

This study furthered the knowledge on heat recirculating reactors with a particular focus on the counter-flow configuration. A new material system, Si-SiC cermet, was investigated that can be additively manufactured methods while offering increased operating temperatures and higher oxidation resistance. The solid freeform fabrication offered by indirect laser sintering of cermet opens new possibilities for combustion devices. The previously unachievable geometries can be manufactured in a repeatable fashion using a material that can withstand direct exposure to flames. This flexibility enabled the fundamental study on the importance of internal heat transfer in the counter-flowing heat recirculating reactors. Heat recirculating reactors rely on internal heat transfer between products and reactants to achieve excess enthalpy combustion. This is beneficial due to increased reaction rates, which expands conventional flammability limits, increases burning rate, and reduces emissions. Expansion of those metrics enables new applications such as thermal oxidization of unwanted species, more efficient radiant heating, or highly flexible fuel reformers. The crucial enthalpy recirculation is achieved by the incorporation of solids into the flow. The introduction of conductive paths allows for an effective heat transfer between hot products and cold reactants. The heat exchange is further optimized by organizing the flow in a counter-flow fashion, a base configuration of the presented work. The proximity of flame to the wall surface and narrow passages with high flow velocities create demanding conditions for high-temperature materials.

The classically available material solution includes a subset of high-temperature metals and a range of ceramics. Maximum operational temperature of metals and oxidation damage proved to be a limiting factor in combustion application, especially for heat recirculating reactors. Meanwhile, the high brittleness and manufacturing

difficulties of ceramics proved challenging in practical applications. A new method of additive manufacturing provided a ceramic-metal composite that combined the advantages of both constituents. The maximum operating temperature of $\approx 1400°C$ with low oxidation damage is a significant increase over ordinary metals and alloys capabilities. The metal infill provides the pliability that reduces the brittleness and enables traditional machining if necessary. This gas-tight, high-temperature material shows excellent potential for combustion applications. Moreover, the inclusion of the laser sintering process enables producing of nearly arbitrary shapes. The improvement to processing steps developed during current research established a reliable path of manufacturing desired parts. The final products show very good geometric capabilities with minimum feature sizes close to 1 mm and channel narrowest passages of 3mm. The geometric reproducibility was within 2% of the digital model, which significantly improved over classic ceramic densification methods experiencing >10% shrinkage. Furthermore, the original over-infiltration issues were substantially reduced by predicting the exact amount of required metal infiltrant.

The new material and geometric capabilities were used in the experimental combustion study of the effects of heat recirculation on counter-flow reactors. Three combustor cores were additively manufactured in Si-SiC using the new technique. Their internal channel geometry was designed to change the amount of heat transfer between channels while maintaining other factors unchanged. It was achieved by implementing the channel shape that modified the wall surface area to channel volume ratio. A simple straight channel geometry was compared with a diverging channel (heat transfer reduced) and a split-channel design (heat transfer increased). All reactors underwent prolonged combustion testing under lean methane-air flames. The stability range was recorded together with wall temperatures and emissions. Furthermore, the material damage to the interior walls was monitored, which supplemented

the data from dedicated flame exposure tests.

4.1 Results

Each experimental Si-SiC reactor operated for ≈ 80 hours under various firing rates and flow conditions. All reactors showed a wide range of stable operations in both Φ and inlet velocity. The upper-temperature limit of the material reduced the maximum FR. Hence, the higher operating temperature of Si-SiC directly impacted the extension of the range of the stable parameters. Blow-off occurred near the lean flammability limit with the leanest stable operation of Φ=0.475 achieved in the diverging reactor. The ultra-lean operation was diminished because of the geometry optimization for higher flow rates than the low Φ operation.

This was further confirmed by comparing previous experimental data and supported by analytical modeling. The degree of heat recirculation showed a positive correlation with the operating range, with the split-channel design achieving the broadest range of operation extending to stoichiometric ratios Φ = 1. Notably, the effective channel length reduction by the inclusion of the splitter wall diminished the split-channel design performance at low velocities compared with the straight channel. In contrast, the split-channel was predicted to have a higher maximum inlet velocity. Although maximum velocities were not reached, the temperature profiles indicate that the straight reactor was closer to the blow-off limit than the split-channel one. Another unique feature of the split-channel reactor was the built-in flame arrestor at the inlet that allowed the exploration of flow conditions that generally result in flashback.

The wall temperature data in each reactor showed characteristic profiles for steady, near blow-off, and near flashback operations. The general shape of wall temperature profiles allowed inference of the approximate flame location. At leaner condi-

tions, the flame resided further upstream in higher heat recirculation cases, providing greater stability. Furthermore, the heat recirculation directly impacted the peak wall temperatures, with the split-channel reactor consistently recording the highest values. The difference in performance between reactors highlighted the importance of heat exchange in the operation of heat recirculating reactors. The cross-comparison between reactors identified a substantial role of heat recirculation in the lean, high-FR region.

The emissions recorded for straight and split-channel reactors showed low CO and NO_x levels characteristic for counter-flow reactor operation. CO levels agree with equilibrium predictions at the exit temperatures due to CO chemistry timescale being shorter than residence time for all, but the fastest flows. Thermal NO_x chemistry is much slower, hence the emissions are instead governed by fast flame-generated NO_x, significantly lower than equilibrium. The split-channel consistently produced higher concentrations of CO than the straight channel reactor. The opposite is true for NO_x where higher heat recirculation in split-channel reactor led to reduced emissions of NO_x despite higher temperatures.

The examination of the condition of the walls throughout the combustion tests period identified slow oxidation damage in the form of silicon oxide flakes. A separate experiment identified an increase of Si-SiC oxidation at temperatures below 1200°C due to instability of a passivating oxide layer. At lower temperatures, the structural change in SiO_2 causes it to spall off in the form of flakes, as observed in the experimental reactor. Meanwhile, the upper-temperature limit is determined by melting of infiltrating metal at $\approx$ 1400°C. Once that happens, the internal stresses cause the molten metal to protrude and pool on the surface. This is directly detrimental by obstructing the flow in the channel. Furthermore, the void left behind in the wall exposes more surfaces to oxidation, hence increasing the oxidation rate. Both pro-

cesses were proven experimentally. Therefore the optimal long-term operating range of as-manufactured Si-SiC is a narrow range between 1200°C and 1350°C

4.2 Recommendations

Future work based on this study should concentrate on creative uses of newly gained freeform fabrication capabilities. The current designs of heat recirculating reactors are directed by shapes achievable with traditional manufacturing methods. AM loosens those limitations enabling new, complex configurations that can bring breakthroughs in the field. A finely controlled porous media with variable porosity along its length might allow the inherent stabilization of submerged flames. In the case of narrow channel designs, such as the counter-flow reactors discussed in this study, the ability to create highly intricate wall shapes opens the possibility to vary the effective thermal conductivity of the wall along its length. That has the potential to limit the external losses while maintaining a high degree of internal recirculation - both critical factors for device performance.

The specific research presented in this work should be extended to rich combustion. The flame behaves differently under rich combustion, which might affect the stability in the complex geometry channels. Furthermore, there are unique challenges material challenges when operating under reducing atmospheres. Subsequently, an experimental sizing study with a broader set of AM reactors should be performed similarly to the numerical work by Belmont [46]. The ability to reliably reproduce even the narrowest geometries enables the validation of analytical and numerical predictions with the experimental data.

A detailed discussion of material science improvements to cermet processes was discussed. Potential areas of further work include a better understanding of mechanical limitations, material with higher operational temperature, and improvements to the oxidation resistance.

Appendix A

Uncertainty calculations

Operating Conditions The operating condition results from mixing air and fuel streams and introducing then into the counterflowing channels with a total cross section A_{CS}. These parameters can be calculated based on the air flowrate $\dot{V}_{AIR}$ and fuel flowrate $\dot{V}_{FUEL}$ reported by flow controllers in Standard Liters Per Minute (SLPM):

$$\Phi = 2 \cdot 4.76 \cdot \frac{\dot{V}_{FUEL}}{\dot{V}_{AIR}} \tag{1}$$

$$u_{inlet} = \frac{1000}{60} \cdot \frac{\dot{V}_{FUEL} + \dot{V}_{AIR}}{A_{CS}} \quad [\text{cm/s}] \tag{2}$$

$$FR = \frac{A_{CS} \cdot u_{inlet}}{1000} \cdot \frac{\Phi}{\Phi + 9.52} \cdot \rho_{STP,CH_4} \cdot \text{LHV}_{CH_4} \quad [\text{kW}] \tag{3}$$

Flow controllers were calibrated by Omega Engineering to the following standards:

Type	Model	Full Scale (FS)	Uncertainty (U)
Air (high flow)	FMA-2611A	250 SLPM	0.8% reading + 0.2% FS
Air (low flow)	FMA6526ST	30 SLPM	1% FS
Fuel	FMA-2607A	10 SLPM	0.8% reading + 0.2% FS

The flow rate was acquired at 4Hz and averaged for a 1Hz reporting rate (4 samples per reading). The reading noise of 3 standard deviations was added to each flowrate uncertainty.

The propagated error for flow parameters can be calculated as follows:

$$U(\Phi) = \frac{2 \cdot 4.76}{\dot{V}_{AIR}} \cdot \left[U\left(\dot{V}_{FUEL}\right) + \frac{\dot{V}_{FUEL}}{\dot{V}_{AIR}} \cdot U\left(\dot{V}_{AIR}\right) \right] \tag{4}$$

$$U(u_{inlet}) = \frac{1000}{60 \cdot A_{CS}} \cdot \left[U\left(\dot{V}_{FUEL}\right) + U\left(\dot{V}_{AIR}\right) + \frac{\dot{V}_{FUEL} + \dot{V}_{AIR}}{A_{CS}} \cdot U\left(A_{CS}\right) \right] \quad (5)$$

$$U(FR) = \frac{1}{60} \cdot U\left(\dot{V}_{FUEL}\right) \cdot \rho_{STP,CH_4} \cdot \mathrm{LHV}_{CH_4} \quad (6)$$

Temperature

The temperature was measured by K-type and N-type thermocouples. The standard limit of error for those thermocouple types is the greater of: ±2.2°C or 0.75% of reading. In current work, the thermocouple error spanned between ±5.25°C and ±10.5°C for the measurement range of 700°C to 1400°C. The rational polynomial function approximation ITS-90 [94] was used to interpret measured voltage to a temperature reading, which introduced a negligible error of ±0.02°C.

The voltage output from thermocouples was digitized by a DAQ system that introduced the quantization uncertainty:

$$U(DAQ) = U_{\text{gain}} \cdot \text{reading} + U_{\text{offset}} + U_{\text{CJC}} + U_{\text{noise}} \quad [\text{mV}]$$

where each uncertainty can be calculated based on the PCI-6225 manual for the voltage reading range of ±0.2 V:

- U_{gain} is 210 ppm
- U_{offset} is ≈ 0.1 mV
- U_{CJC} is equivalent to ±1°C imposed by the SCB-68 connector block
- U_{noise} is the noise error discussed below

The 16-bit ADC resolution for ±0.2V range translates the temperature resolution of ±0.2°C. However, the random noise of μV range introduced as much as ±20°C variance between subsequent readings. The oversampling approach, discussed in Application Note 118 by Silicon Labs [95], was used to increase effective ADC resolution and improve the signal-to-noise ratio. The dithering function of the PCI-6225 DAQ card provided a suitable Gaussian noise pattern for this application. The temperature was sampled at 1024Hz, and subsequent decimation to 1Hz final measurement rate provided resolution improvement to 21 bit (±0.005°C) and a significantly reduced noise uncertainty of 3-sigma confidence:

$$U_{\text{noise}} = \frac{3 \cdot \text{st.dev. (noise)}}{\sqrt{\text{samples}}}$$

Using 1024 samples per reading reduced the noise by a factor of 32. In practice, the noise uncertainty component of a singular measurement was between 0.2°C and 0.6°C, depending on the particular conditions.

All reading uncertainties were propagated through ITS-90 polynomials parallel with the temperature readings to calculate the propagated temperature error for each measurement. This process resulted in the combined DAQ quantization uncertainty between 1.5°C and 2°C. Therefore the final temperature uncertainty is a combination of quantization uncertainty and thermocouple limits of error. The exact value of uncertainty is calculated for each measured value but varies between ±6.75°C and ±11. °C for the 700°C to 1400°C reading range respectively.

Emissions

Emission measurements were obtained from calibrated MRU Vario Luxx gas analyzer. The specified uncertainties are as follows:

Component	Method	Uncertainty (U)
O_2	EC sensor	± 0.2%
CO	EC sensor	higher of: ± 10 ppm or 5% of reading
CO_2	NDIR	higher of: ± 0.3% or 2% of reading
NO	EC sensor	higher of: ± 2 ppm or 5% of reading
NO_2	EC sensor	higher of: ± 2 ppm or 5% of reading
CH_4	NDIR	higher of: ± 20 ppm or 2% of reading

The reported NO_x value is a sum of NO and NO_2 measurement. The propagated uncertainty can be calculated:

$$U(NO_x) = U(NO) + U(NO_2) \approx \pm 4 \text{ ppm} \tag{7}$$

The validity of calibration was periodically checked by set of calibration gasses obtained from Cal Gas Direct:

Gas code	Composition
298	100 ppm CO, 5% CO_2, 10% O_2, bal. N_2
150N-60	60 ppm CH_4, bal. N_2
125-10	10 ppm NO, bal. N_2
112-5	5 ppm NO_2, bal. Air

The calibration gas for all compounds, besides NO_2, was delivered via the combined bypass & water bubbler system, as specified by the manufacturer. The bubbler was omitted in the case of NO_2 due to its water sensitivity.

Bibliography

[1] E. Mallard and H. Le Chatelier, *Recherches expérimentales et théoriques sur la combustion des mélanges gazeux explosives*. H. Dunod et E. Pinat, 1883.

[2] C. K. Law, *Combustion physics*. Cambridge: Cambridge University Press, 2006.

[3] D. B. Spalding and J. W. Linnett, "A theory of inflammability limits and flame-quenching," *Proceedings of the Royal Society of London. Series A. Mathematical and Physical Sciences*, vol. 240, no. 1220, pp. 83–100, 1957.

[4] F. J. Weinberg, "Combustion temperatures: the future?," *Nature*, vol. 233, pp. 239–241, 1971.

[5] F. Weinberg, "Heat-recirculating burners: Principles and some recent developments," *Combust. Sci. Technol.*, vol. 121, pp. 3–22, 1996.

[6] I. Schoegl and J. L. Ellzey, "Superadiabatic combustion in conducting tubes and heat exchangers of finite length," *Combust. Flame*, vol. 151, pp. 142–159, 2007.

[7] A. R. Jones, S. A. Lloyd, and F. J. Weinberg, "Combustion in heat exchangers," *Proc. R. Soc. A Math. Phys. Eng. Sci.*, vol. 360, pp. 97–115, 1978.

[8] J. Howell, M. Hall, and J. Ellzey, "Combustion of hydrocarbon fuels within porous inert media," *Progress in Energy and Combustion Science*, vol. 22, no. 2, pp. 121–145, 1996.

[9] S. Wood and A. T. Harris, "Porous burners for lean-burn applications," *Progress in Energy and Combustion Science*, vol. 34, no. 5, pp. 667–684, 2008.

[10] M. A. Mujeebu, M. Abdullah, M. A. Bakar, A. Mohamad, and M. Abdullah, "Applications of porous media combustion technology – a review," *Applied Energy*, vol. 86, no. 9, pp. 1365–1375, 2009.

[11] D. J. Moon, J. W. Ryu, S. D. Lee, B. G. Lee, and B. S. Ahn, "Ni-based catalyst for partial oxidation reforming of iso-octane," *Applied Catalysis A: General*, vol. 272, no. 1, pp. 53–60, 2004.

[12] Y. Ju, C. P. Cadou, and K. Maruta, *Microscale combustion and power generation*. New York: Momentum Press, 2015.

[13] A. Gutkowski, L. Tecce, and J. Jarosinski, "Some features of propane-air flames under quenching conditions in narrow channels," *Combustion Science and Technology*, vol. 180, no. 10-11, pp. 1772–1787, 2008.

[14] D. G. Goodwin, H. K. Moffat, and R. L. Speth, "Cantera: An object-oriented software toolkit for chemical kinetics," *Thermodynamics, and Transport Processes http://www.cantera.org. Version 2. 3*, vol. 2.3, 2017.

[15] D. Dunn-Rankin and P. Therkelsen, *Lean combustion : technology and control*. Academic Press, Elsevier, 2016.

[16] N. S. Kaisare and D. G. Vlachos, "A review on microcombustion: Fundamentals, devices and applications," *Progress in Energy and Combustion Science*, vol. 38, no. 3, pp. 321–359, 2012.

[17] A. C. Fernandez-Pello, "Micropower generation using combustion: Issues and approaches," *Proceedings of the Combustion Institute*, vol. 29, no. 1, pp. 883–899, 2002. Proceedings of the Combustion Institute.

[18] F. Weinberg, D. Rowe, G. Min, and P. Ronney, "On thermoelectric power conversion from heat recirculating combustion systems," *Proceedings of the Combustion Institute*, vol. 29, no. 1, pp. 941–947, 2002. Proceedings of the Combustion Institute.

[19] V. KHANNA, R. GOEL, and J. L. ELLZEY, "Measurements of emissions and radiation for methane combustion within a porous medium burner," *Combustion Science and Technology*, vol. 99, no. 1-3, pp. 133–142, 1994.

[20] R. Mital, J. Gore, and R. Viskanta, "A study of the structure of submerged reaction zone in porous ceramic radiant burners," *Combustion and Flame*, vol. 111, no. 3, pp. 175–184, 1997.

[21] N. I. Kim, S. Kato, T. Kataoka, T. Yokomori, S. Maruyama, T. Fujimori, and K. Maruta, "Flame stabilization and emission of small swiss-roll combustors as heaters," *Combustion and Flame*, vol. 141, no. 3, pp. 229–240, 2005.

[22] M. Zenker, A. Heinzel, G. Stollwerck, J. Ferber, and J. Luther, "Efficiency and power density potential of combustion-driven thermophotovoltaic systems using gasb photovoltaic cells," *IEEE Transactions on Electron Devices*, vol. 48, no. 2, pp. 367–376, 2001.

[23] H. Wu, M. Kaviany, and O. Kwon, "Thermophotovoltaic power conversion using a superadiabatic radiant burner," *Applied Energy*, vol. 209, pp. 392–399, 2018.

[24] P. Gentillon, J. Southcott, Q. N. Chan, and R. A. Taylor, "Stable flame limits for optimal radiant performance of porous media reactors for thermophotovoltaic applications using packed beds of alumina," *Applied Energy*, vol. 229, pp. 736–744, 2018.

[25] C. H. Chen and P. D. Ronney, "An active gas mask using a heatrecirculating burner," *Spring Technical Meeting, Combustion Institute, Western States Section*, 2008.

[26] J. L. Ellzey, E. L. Belmont, and C. H. Smith, "Heat recirculating reactors: Fundamental research and applications," *Progress in Energy and Combustion Science*, vol. 72, pp. 32–58, 2019.

[27] Z. Al-Hamamre, S. Voß, and D. Trimis, "Hydrogen production by thermal partial oxidation of hydrocarbon fuels in porous media based reformer," *International Journal of Hydrogen Energy*, vol. 34, no. 2, pp. 827–832, 2009.

[28] A. da Rosa, "Chapter 10 - hydrogen production," in *Fundamentals of Renewable Energy Processes*, pp. 371–428, Elsevier Inc, third edition ed., 2012.

[29] J. Ahn, P. D. Ronney, Z. Shao, and S. M. Haile, "A thermally self-sustaining miniature solid oxide fuel cell," *Journal of fuel cell science and technology*, vol. 6, no. 4, 2009.

[30] C. Hays, "Romm, joseph j. the hype about hydrogen: Fact and fiction in the race to save the climate," *Booklist*, vol. 100, no. 14, pp. 1250–, 2004.

[31] R. V. Fursenko, S. S. Minaev, and V. S. Babkin, "Thermal interaction of two flame fronts propagating in channels with opposing gas flows," *Combustion, explosion, and shock waves*, vol. 37, no. 5, pp. 493–500, 2001.

[32] P. D. Ronney, "Analysis of non-adiabatic heat-recirculating combustors," *Combust. Flame*, vol. 135, pp. 421–439, 2003.

[33] Y. Ju and C. Choi, "An analysis of sub-limit flame dynamics using opposite

propagating flames in mesoscale channels," *Combustion and Flame*, vol. 133, no. 4, pp. 483–493, 2003.

[34] C. H. Chen and P. D. Ronney, "Scale and geometry effects on heat-recirculating combustors," *Combust. Theory Model.*, vol. 17, no. 5, pp. 888–905, 2013.

[35] I. M. Schoegl and J. L. Ellzey, "Numerical investigation of ultra-rich combustion in counter flow heat exchangers," *Combust. Sci. Technol.*, vol. 182, no. 10, pp. 1413–1428, 2010.

[36] C. H. Chen and P. D. Ronney, "Three-dimensional effects in counterflow heatre-circulating combustors," *Proc. Combust. Inst.*, vol. 33, pp. 3285–3291, 2011.

[37] J. Chen, X. Gao, L. Yan, and D. Xu, "Effect of wall thermal conductivity on the stability of catalytic heat-recirculating micro-combustors," *Applied thermal engineering*, vol. 128, pp. 849–860, 2018.

[38] K. Maruta, J. K. Parc, K. C. Oh, T. Fujimori, S. S. Minaev, and R. V. Fursenko, "Characteristics of microscale combustion in a narrow heated channel," *Combustion, explosion, and shock waves*, vol. 40, no. 5, pp. 516–523, 2004.

[39] J. Ahn, C. Eastwood, L. Sitzki, and P. D. Ronney, "Gas-phase and catalytic combustion in heat-recirculating burners," *Proceedings of the Combustion Institute*, vol. 30, no. 2, pp. 2463–2472, 2005.

[40] I. Schoegl and J. L. Ellzey, "A mesoscale fuel reformer to produce syngas in portable power systems," *Proc. Combust. Inst.*, vol. 32, pp. 3223–3230, 2009.

[41] V. Vijayan and A. Gupta, "Combustion and heat transfer at meso-scale with thermal recuperation," *Applied energy*, vol. 87, no. 8, pp. 2628–2639, 2010.

[42] E. L. Belmont, I. Schoegl, and J. L. Ellzey, "Experimental and analytical investigation of lean premixed methane/air combustion in a mesoscale counter-flow reactor," *Proc. Combust. Inst.*, vol. 34, pp. 3361–3367, 2013.

[43] S. A. LLOYD and F. J. WEINBERG, "A burner for mixtures of very low heat content," *Nature (London)*, vol. 251, no. 5470, pp. 47–49, 1974.

[44] S. A. Lloyd, "Combustion in double spiral burners," *Industrial & engineering chemistry research*, vol. 33, no. 7, pp. 1809–1816, 1994.

[45] J. Hoffmann, R. Echigo, H. Yoshida, and S. Tada, "Experimental study on combustion in porous media with a reciprocating flow system," *Combustion and Flame*, vol. 111, no. 1, pp. 32–46, 1997.

[46] E. L. Belmont, P. P. Radyjowski, and J. L. Ellzey, "Effect of geometric scale on heat recirculation and syngas production in a noncatalytic counter-flow reformer," *Combust. Sci. Technol.*, vol. 187, no. 6, pp. 874–893, 2015.

[47] E. L. Belmont, S. M. Solomon, and J. L. Ellzey, "Syngas production from heptane in a non-catalytic counter-flow reactor," *Combustion and Flame*, vol. 159, no. 12, pp. 3624–3631, 2012.

[48] E. L. Belmont and J. L. Ellzey, "Lean heptane and propane combustion in a non-catalytic parallel-plate counter-flow reactor," *Combust. Flame*, vol. 161, pp. 1055–1062, 2014.

[49] G. W. Meetham, "High-temperature materials — a general review," *Journal of Materials Science*, vol. 26, pp. 853–860, 1991.

[50] Y. Bar-Cohen, *High temperature materials and mechanisms / edited by Yoseph Bar-Cohen.* Boca Raton, Florida: CRC Press, 1st edition ed., 2014 - 2014.

[51] J. R. Davis, *Heat-resistant materials*. Materials Park, Ohio: ASM International, 1997.

[52] M. F. Ashby, *Materials selection in mechanical design Michael F. Ashby.* Amsterdam ;: Butterworth-Heinemann, 3rd ed. ed., 2005.

[53] C. T. Sims, N. S. Stoloff, and W. C. Hagel, *Superalloys II.* Wiley-Interscience, 1987.

[54] J. Justin and A. Jankowiak, "Ultra High Temperature Ceramics : Densification, Properties and Thermal Stability.," *AerospaceLab*, pp. p. 1–11, Nov. 2011.

[55] K. Ono, "A simple estimation method of weibull modulus and verification with strength data," *Applied Sciences*, vol. 9, no. 8, 2019.

[56] W. M. Mathis and J. L. Ellzey, "Flame stabilization, operating range, and emissions for a methane/air porous burner," *Combust. Sci. Technol.*, vol. 175, pp. 825–839, 2003.

[57] B. J. Vogel and J. Ellzey, "Subadiabatic and superadiabatic performance of two-section porous burner," *Combust. Sci. Technol.*, vol. 177, pp. 1323–1338, 2005.

[58] J. Deckers, J. Vleugels, and J. Kruth, "Additive manufacturing of ceramics: A review," *Journal of ceramic science and technology*, vol. 5, pp. 245–260, 2014.

[59] N. Travitzky, A. Bonet, B. Dermeik, T. Fey, I. Filbert-Demut, L. Schlier, T. Schlordt, and P. Greil, "Additive manufacturing of ceramic-based materials," *Advanced Engineering Materials*, vol. 16, no. 6, pp. 729–754, 2014.

[60] M. Vaezi, S. Chianrabutra, B. Mellor, and S. Yang, "Multiple material additive manufacturing – part 1: A review," *Virtual and Physical Prototyping*, vol. 8, 03 2013.

[61] J. Halloran, "Free form fabrication of ceramics," *British Ceramic Transactions*, vol. 98, pp. 299–303, 06 1999.

[62] J. Wilkes, Y.-C. Hagedorn, W. Meiners, and K. Wissenbach, "Additive manufacturing of zro2-al2o3 ceramic components by selective laser melting," *Rapid Prototyping Journal*, vol. 19, 01 2013.

[63] M. Leu, S. Pattnaik, and G. Hilmas, "Investigation of laser sintering for freeform fabrication of zirconium diboride parts," *Virtual and Physical Prototyping*, vol. 7, pp. 25–36, 03 2012.

[64] N. Harlan, S.-M. Park, D. L. Bourell, and J. J. Beaman, "Selective laser sintering of zirconia with micro-scale features," in *1999 International Solid Freeform Fabrication Symposium*, 1999.

[65] A. Streek, P. Regenfuss, F. Ullmann, L. Hartwig, R. Ebert, H. Exner, and F. Laserapplikationszentrum, "Processing of silicon carbide by laser micro sintering," in *17th Solid Freeform Fabrication Symposium, SFF 2006*, pp. 349–358, 01 2006.

[66] Wikipedia contributor: FM1418, "Selective laser sintering process diagram," 2020. [Online; accessed 03/18/2021].

[67] S. Song, Z. Gao, B. Lu, C. Bao, B. Zheng, and L. Wang, "Performance optimization of complicated structural sic/si composite ceramics prepared by selective laser sintering," *Ceramics International*, vol. 46, no. 1, pp. 568–575, 2020.

[68] P. Kennedy and J. V. Shennan, "Engineering applications of refel silicon carbide," in *Silicon carbide–1973; proceedings*, (Columbia), pp. 359–366, Interna-

tional Conference on Silicon Carbide (3rd : 1973 : Miami Beach, Fla.), University of South Carolina Press, 1974.

[69] U. Ernstberger, H. Cohrt, F. Porz, and F. Thümmler, "Oxidation von silizium-infiltriertem siliziumkarbid.," *Berichte der DKG*, vol. 60, pp. 167–173, 1983.

[70] B. Y. Stevinson, D. L. Bourell, and J. J. Beaman Jr., "Support-free infiltration of selective laser sintered (sls) silicon carbide preforms," 2006-09-14.

[71] R. S. Evans, D. J. Bourell, J. J. Beaman, and M. I. Campbell, "Reaction bonded silicon carbide: Sff, process refinement and applications," in *2003 International Solid Freeform Fabrication Symposium*, pp. 414–422, 2003.

[72] A. Mortensen and J. A. Cornie, "On the infiltration of metal matrix composites," *Metallurgical and materials transactions. A, Physical metallurgy and materials science*, vol. 18, no. 6, pp. 1160–1163, 1987.

[73] B. Stevinson, D. Bourell, and J. Beaman, "Over-infiltration mechanisms in selective laser sintered si/sic preforms," *Rapid Prototyp. J.*, vol. 14, pp. 149–154, 2008.

[74] P. A. Williams, R. Sakidja, J. H. Perepezko, and P. Ritt, "Oxidation of zrb2–sic ultra-high temperature composites over a wide range of sic content," *Journal of the European Ceramic Society*, vol. 32, no. 14, pp. 3875–3883, 2012.

[75] F. Delannay, L. Froyen, and A. Deruyttere, "The wetting of solids by molten metals and its relation to the preparation of metal-matrix composites composites," *Journal of materials science*, vol. 22, no. 1, pp. 1–16, 1987.

[76] S. K. WOO, C. H. KIM, and E. S. KANG, "Fabrication and microstructural

evaluation of zrb2/zrc/zr composites by liquid infiltration," *Journal of materials science*, vol. 29, no. 20, pp. 5309–5315, 1994.

[77] H.-L. Liu, G.-J. Zhang, J.-X. Liu, and H. Wu, "Synergetic roles of zrc and sic in ternary zrb2-sic-zrc ceramics," *Journal of the European Ceramic Society*, vol. 35, pp. 4389–4397, 12 2015.

[78] Y. Zhang, D. Gao, C. Xu, Y. Song, and X. Shi, "Oxidation behavior of hot pressed zrb2-zrc-sic ceramic composites," *International Journal of Applied Ceramic Technology*, vol. 11, no. 1, pp. 178–185, 2014.

[79] Y. Wang, B. Ma, L. Li, and L. An, "Oxidation behavior of zrb2–sic–tac ceramics," *Journal of the American Ceramic Society*, vol. 95, no. 1, pp. 374–378, 2012.

[80] P. R. Radyjowski, I. M. Schoegl, and J. L. Ellzey, "Experimental and analytical investigation of a counterflow reactor at lean conditions," *Combust. Sci. Technol.*, (under review) 2021.

[81] P. R. Radyjowski, D. Bourell, and J. L. Ellzey, "Advanced heat recirculating counterflow reactors utilizing additive manufacturingr," *2019 WSSCI Fall Technical Meeting*, 2019.

[82] P. R. Radyjowski and J. L. Ellzey, "Advanced heat recirculating counterflow reactors: Experimental study on the influence of gas-solid heat transfer," *Combust. Sci. Technol.*, (under review) 2021.

[83] C. H. Smith, D. I. Pineda, and J. L. Ellzey, "Syngas production from burner-stabilized methane/air flames: The effect of preheated reactants," *Combustion and Flame*, vol. 160, no. 3, pp. 557–564, 2013.

[84] I. M. Schoegl, *Superadiabatic Combustion in Counter-Flow Heat Exchangers*. PhD thesis, The University of Texas at Austin, 2009.

[85] I. Schoegl, "Radiation effects on flame stabilization on flat flame burners," *Combustion and Flame*, vol. 159, no. 9, pp. 2817–2828, 2012.

[86] I. Schoegl, V. M. Sauer, and P. Sharma, "Predicting combustion characteristics in externally heated micro-tubes," *Combustion and Flame*, vol. 204, pp. 33–48, 2019.

[87] B. J. Matkowsky and G. I. Sivashinsky, "An asymptotic derivation of two models in flame theory associated with the constant density approximation," *SIAM J. Appl. Math.*, vol. 37, no. 3, p. 686–699, 1979.

[88] University of California at San Diego, "*San Diego Mechanism web page, Mechanical and Aerospace Engineering (Combustion Research)*," 2016. URL `http://combustion.ucsd.edu`, Accessed: 2021-03-30.

[89] T. Takeno and K. Sato, "An excess enthalpy flame theory," *Combust. Sci. Technol.*, vol. 20, no. 1-2, pp. 73–84, 1979.

[90] T. Takeno and K. Hase, "Effects of solid length and heat loss on an excess enthalpy flame," *Combust. Sci. Technol.*, vol. 31, no. 3-4, pp. 207–215, 1983.

[91] F. N. Egolfopoulos, P. Cho, and C. K. Law, "Laminar flame speeds of methane-air mixtures under reduced and elevated pressures," *Combust. Flame*, vol. 76, pp. 375–391, 1989.

[92] G. P. Smith, D. M. Golden, M. Frenklach, N. W. Moriarty, B. Eiteneer, M. Goldenberg, T. Bowman, R. K. Hanson, S. Song, W. C. J. Gardiner, V. V. Lissianski,

and Z. Qin, "*GRI-Mech 3.0 Home Page*," 2000. URL `http://combustion.berkeley.edu/gri-mech/version30/text30.html`, Accessed: 2021-03-30.

[93] E. Rezaeia, S. Haussener, S. Gianella, and A. Ortona, "Early-stage oxidation behavior at high temperatures of sisic cellular architectures in a porous burner," *Ceramics International*, vol. 42, no. 14, pp. 16255–16261, 2016.

[94] NIST, "*ITS-90 Thermocouple Database, Standard Reference Database 60*," 1999. URL `https://srdata.nist.gov/its90/main/`, Accessed: 2021-03-30.

[95] Silicon Laboratories, *Improving ADC Resolution by Oversampling and Averaging*. Application Note 118, Silicon Laboratories, 2013.